Relationship between Aquarius L-band Active and Passive multi-year observations over Australia

by

Maria de Quadras

Thesis

Submitted to the UPC University for the degree of Engineering of Telecommunications

Advisors: Nuria Duffo and Maria Piles

ACKNOWLEDGEMENTS

I am highly indebted to M. Piles, N. Duffo and C. Rüdiger for this project would not have been possible without their knowledge, guidance and inspiration. My thanks and appreciations also go to my mother for her love, encouragement and unconditional support.

I would like to extend my sincere gratitude to my brother, Luis, and J. Allen for their enthusiasm, attention and time. Special thanks to my colleague and friend, C. Amat, for creating a stimulating environment to learn and grow.

CONTENTS

LIST OF TABLES

LIST OF FIGURES

LIST OF APPENDICES

1 INTRODUCTION

In 624 B.C. Thales of Miletus stated that "water constitutes the element and principle of all things". From the birth of civilization until present day, water has been crucial for the development of society. It makes life possible and plays a vital role in the proper functioning of the Earth's ecosystem.

The water cycle is essential for the energy exchanges between atmosphere, ocean and land. Considering that, the interaction among these various factors is very complex and numerous questions remain unresolved, Scientists have applied cutting-edge technology for understanding the Earth's climate and its variability.

The first weather satellite, TIROS I, was launched in 1960. While it was only operational for 78 days, it proved that it was possible to monitor the weather in a global scale. Many satellite launches later, in 2011, a joint mission between NASA and the Argentinian space agency (CONAE), launched Aquarius/SAC-D satellite for measuring global sea surface salinity. Although the main objective was focused in the ocean, Aquarius included passive and active sensors measuring at L-band, which provided a unique opportunity for the Earth's water research.

While active sensors have their own source of illumination, passive sensors detect the electromagnetic energy emitted and scattered by Earth's surface and atmosphere. The advantages of using active sensors are that they are able to measure at a higher resolution. However, they have a more significant interference from vegetation, water content, surface roughness and topography.

Active and passive measurements cover different scales that can be combined to obtain relative advantages of the two sensing approaches.

1.1 Objectives

The aim of this Thesis is to further our understanding of the geophysical information that can be estimated from active and passibe L-band sensors. Three active-derived indices, namely Roughness Radar Index, Soil Moisture Index and the Radar Vegetation Index are examined and compared to active backscatter and passive emissivity

signals acquired with the Aquarius sensor during years 2011-2014 over specific scenarios within the Australian continent. Once the individual behaviours of the variables are understood, the main focus remains in studying the relation between the data obtained with the active sensor and the data acquired from the passive sensor.

Emissivity is a passive physical magnitude that at L-band is directly dependant on the water content of the emitting element. This thesis will study its temporal evolution along the different climate classes and will relate the information it contains to vegetation properties, rainfall and topography patterns of the study regions.

All the data was obtained from NASA's satellite, Aquarius, during the period: September 2011- August 2014. The target area for this Thesis is the vast and diverse country of Australia. Australia is a suited target due to its different climates classes and vast variety of vegetation.

The majority of the research described in this Thesis has been carried out at the UPC, in the Signal Theory and Communications laboratory. Research was also carried out during a seven-month stay at Monash University with Professor Chris Rudiger, which provided a better understanding of the target area. Further understanding was also gathered through participation of a field campaign in Birchip, Australia.

1.2 Thesis Organization

This Thesis is devoted to a better understanding of active and passive climate variables in the area of Australia and it is organized as follows:

Chapter 1 describes the aim of the Thesis and its scientific interest.

Chapter 2 introduces the importance of water cycle monitoring and the differences between radar and radiometer measurements.

Chapter 3 describes the basic concepts of radiometry and scatterometry.

Chapter 4 summarizes the SMOS, AQUARIUS and SMAP missions.

Chapter 5 reviews the datasets and methods for acquiring the different variables and describes the target area of the study.

Chapter 6 presents the radar and passive variables and analyses the relationship between active and passive measurements.

Chapter 7 recapitulates the main conclusions of the Thesis.

2 BASIC CONCEPTS

This chapter contains background information related to the Aquarius/SAC-D project. It describes the importance of monitoring the water cycle and it introduces the two main instruments of the satellite: the radar and the radiometer. The state-of-the-art of scatterometers and radiometers is also included.

2.1 The water cycle

Even though the water quantity is fix, the compartments for water storage can be very variable. The water cycle refers to the circulation of water in its different phases liquid, solid, and vapour while travelling in the atmosphere, from soil, rivers, lakes, and oceans. Water on Earth is continually exchanging from the oceans to the atmosphere and to the Earth. Around 86 percent of global evaporation and 78 percent of global precipitation take place over the ocean [1].

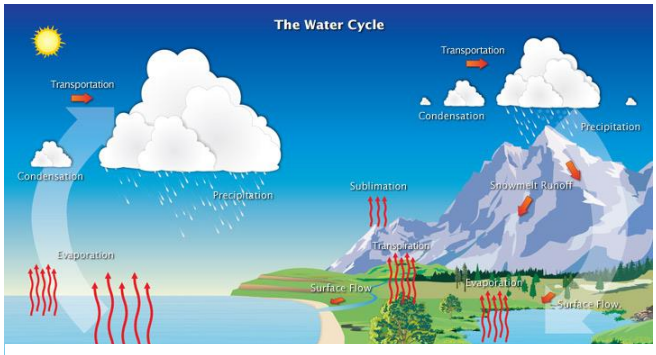

Figure 2-1: Representation of the water cycle

Most of the water, when heated by the sun, evaporates and goes into the air. Ice and snow sublimate, which is the process where they change into vapour without going through the liquid phase. This vapour together with the water transpired from the plants and the water evaporated from the soil (evapotransportation) is carried to the stratosphere by air currents, where it condenses into clouds that precipitate. Most of the precipitation returns into

the ocean or land. Infiltration occurs when water or snow penetrates into the soil or rocks.

The information about the amount of water available to evaporate can be used to develop a better weather forecasting. With soil moisture data (p. 25), there is a possibility to progress in the irrigation planning and crop yield forecast. By knowing the amount of moisture in the soil, warnings can be created if there is a deficit of moisture or if the soil is wet before a rainstorm [2]. Another soil moisture sensing application is to get a better understanding of the energy and carbon exchanges between the land and the air.

Water cycle processes are associated with vegetation patterns. It has an impact in society monitoring agriculture, in meteorological forecasting, hydrological modelling, monitoring photosynthesis and plant growth. Besides, near real time estimations of soil moisture can forecast threatening events from drought to heat waves or floods [3]. Under the effect of the sun, the circulation and conservation of water on Earth is the most valuable resource, and has a direct impact on sustaining life weather and climate. Increase of global temperatures during the last century cause excess heat which is absorbed and moved by the ocean. Changes in the atmospheric temperature of the ocean surface may lead to more evaporation phenomena resulting in higher salinity density. For all of the above, measurement of water becomes critically important for human beings.

Researchers have the challenge to understand if Earth water cycle modifications are altered by climate changes. This question will lead to better comprehend how Earth works, and it will be applicable to environmental policy and decision-making [4].

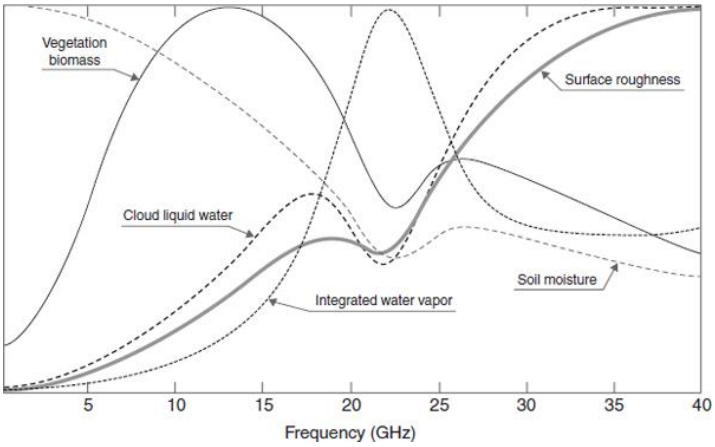

Figure 2-2: Interferences for each Frequency band

2.2 Active and Passive Microwave sensors

2.2.1 Active sensors

Radars are active sensors that provide their own source of illumination and combine a transmitter and a receiver. They are able to remotely sense a surface at high spatial resolution (less than 1 km with Aperture Synthesis). However, the radar backscattering is highly influenced by the effects of surface roughness, topography, vegetation canopy structure, and water content, and it is difficult to disentangle the different contributions to the total signal

and hence estimate a geophysical property [4].

Aquarius/SAC-D satellite radar is a scatterometer (p. 15) called ALScat.

State of the Art

There are mainly four different kinds of spaceborne scatterometers that have been the predecessors of nowadays scatterometers. Three of them were fan-beam scatterometers and one was a conically scanning pencil-beam scatterometer. These four scatterometers are, listed in chronological order [6]:

- SASS: the Seasat-A Satellite Scatterometer, which was flown on NASA's Seasat satellite and operated between June and October, 1978 before a power failure terminated the mission.

- ESCAT: the European Space Agency's (ESA) Earth Remote Sensing (ERS)-1 & -2 Active Microwave Instrument (AMI) scatterometer, the first of which operated between 1992-1996 and the second of which has been operating since 1996.

- NSCAT: the NASA Scatterometer (NSCAT), which was flown aboard the Japanese Aerospace Exploration Agency's (JAXA; then known as NASDA) Advanced Earth Observing Satellite (ADEOS)-I (also sometimes referred to as Midori-I) between August, 1996 and June, 1997 before a power failure prematurely terminated this mission as well.

- QSCAT: NASA Quick Scatterometer (QuikSCAT) SeaWinds instrument, flown aboard QuikSCAT from 1999 to the present as well as on the JAXA ADEOS-II satellite (also referred to as Midori-II) as SeaWinds-II from 2002 until late September 2003 when a power failure also terminated this mission.

Figure 2-3 shows the characteristics of the different radars. Although radars have been used until present days, there was a gap between the years 1978 and 1992. This fact has been adverse for studying long-term climate change.

	SASS	ERS-1/2	NSCAT	SeaWinds
FREQUENCY	14.6 GHz	5.3 GHz	13.995 GHz	13.6 GHz
AZIMUTHS				
POLAR.	V-H, V-H	V ONLY	V, V-H, V	V-OUTER/H-INNER
BEAM RESOLUTION	FIXED DOPPLER	RANGE GATE	VARIABLE DOPPLER	PENCIL-BEAM
SCI. MODES	MANY	SAR, WIND	WIND ONLY	WIND/HI-RES
RESOLUTION	50/100 km	25/50 km	25/50 km	25 km/6x25km
SWATH	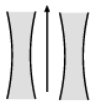		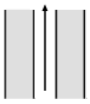	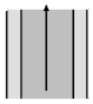
INCIDENCE ANGS	0° - 70°	18° - 59°	17° - 60°	45° & 54°
DAILY COVERAGE	VARIABLE	< 41 %	78 %	92 %
DATES	6/78 – 10/78	92–96 & 96–	8/96 – 6/97	5/99 & 11/01

Figure 2-3: Scatterometers characteristics

2.2.2 Passive sensors

Radiometer is a passive sensor because it consists only in a receiver that measures the radiation naturally emitted from the scene under observation. The advantages of the radiometers versus the radars are that they have a higher sensibility to soil water content and a reduced sensibility to land surface roughness and vegetation geometry. However, passive sensors spatial resolution is limited to 40 to 50 km due to practical constrains on antenna size and the altitude of low Earth orbits [5].

State of the Art

United States has been launching series of passive satellites since the 70's. In 1978, Nimbus-7 was launched by NASA with earth observation purposes. More precisely, its objectives were to test new instruments (sensors) and to provide atmospheric data. Its radiometer, SMMR, worked at five different frequencies: 6.6, 10.7, 18, 21 and 37 GHz. After, sensor SSM/I was used in the Defense Meteorological Satellite Program of the US Department of Defense to collect cloud cover data. It received four frequencies from 19.35 to 85 GHz, with footprints size of 68.9 x 44.3 to 15.7 x 13.9 (km x km).

In 1997, TRMM satellite was launched. It was a joint mission from NASA and JAXA, and lasted for 15 years. The satellite collected data of tropical and subtropical rainfall, which is parameter in global change [7]. The radiometer frequency range went from 10.7 to 85.5 GHz and the footprints size went from 63 x 37 to 7 x 5 (km x km).

Other Earth observations missions were AQUA (NASA), ADEOS II (JAXA) and GCOM-W1 (JAXA). The missions used the same families of passive sensors, called: AMSR-E, AMSR and AMSR2, respectively. The first two were launched in 2002 and had six frequency channels (6.925, 7.3, 10.65, 18.7, 23.8, 36.5 and 89.0 GHz).The last one, was launched in 2012 and received also at 7.3GHz. GCOM-W1 is still orbiting today and its primary goal is to achieve sustained observations of the Earth's environment [8].

These satellite missions have been developing radiometers' technology with the aim to improve the weather's

knowledge. Aquarius radiometer, ALRad, is the successor of Jason Microwave Radiometer (JMR). JMR is a passive microwave radiometer measuring the brightness temperatures at 18.7, 23.8 and 34 GHz. It was included in Jason-1 satellite which was the joint CNES/NASA oceanographic mission.

3 REMOTE SENSING

This section covers the theoretical basis of radiometry and scatterometry.

3.1 Microwave Radiometry

The Earth receives the bulk of the energy as solar electromagnetic radiation. This incident solar energy is divided into:

- energy that is scattered and absorbed by the Earth atmosphere, and
- energy that is transmitted to the Earth surface, and subsequently divided into:
    - scattered energy outward the Earth surface
    - absorbed energy by the Earth surface

The absorption of electromagnetic energy by a material medium applying the thermodynamic theory results in the transformation of electromagnetic energy into thermal energy, increasing the material temperature [9]. There is a balance between the absorbed and emitted solar radiation by the Earth surface and atmosphere.

The science area that studies the electromagnetic radiation is named Radiometry. The emission of this radiation is measured by instruments called radiometers. This section introduces several basic concepts of radiometry necessary for comprehending this project.

3.1.1 Brightness

Figure 3-1 is a schematic representation of the geometry for power received by an emitting body, where A_t and A_r are the areas of a transmitting and receiving antenna respectively separated by a distance R, which is sufficiently large so that the power density, S_t , of the transmitting antenna can be defined as a constant over the solid angle Ω_r [9].

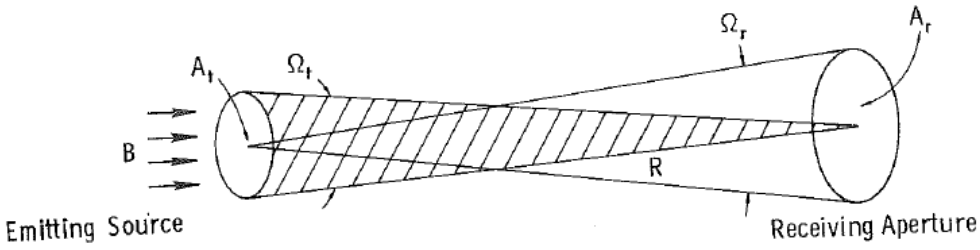

Figure 3-1: Antenna diagram with receiving and emitting source

Brightness, the quantity of bright, $B\ (\theta, \phi)$ (W.sr $^{-1}$.m^{-2}) is defined as the power emitted by a body at a solid angle per Ω unit area:

$$B\ (\theta, \phi) = \frac{F_t\ (\theta,\phi)}{A_t} \qquad (1)$$

where Ft (θ, ϕ) is the normalized radiation pattern of the transmitted antenna and A_t is the radiation area.

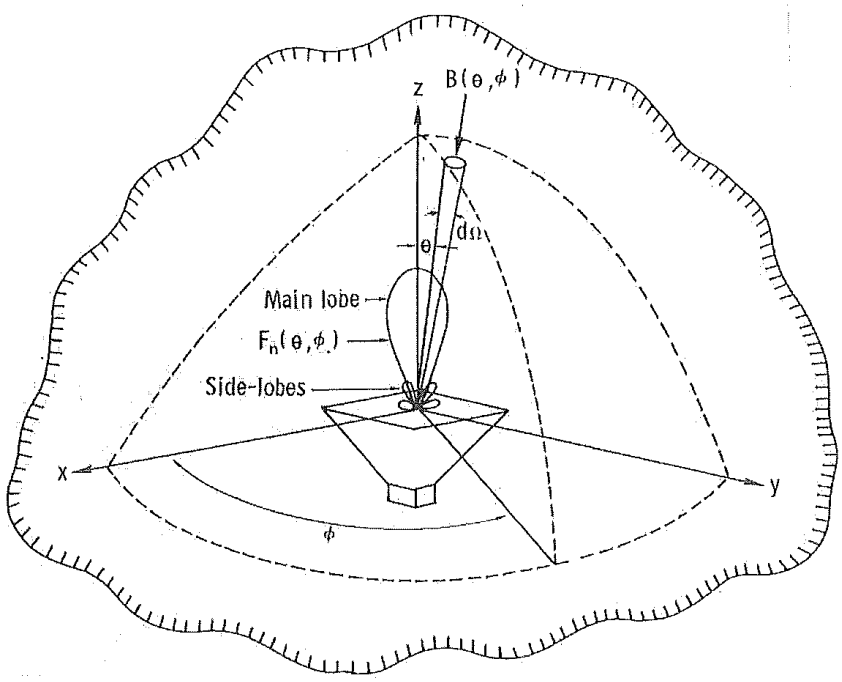

Figure 3-2: Geometry of the incident radiation on an antenna

If we consider Figure 3-2: **Geometry of the incident radiation on an antenna**, the total power received by the antenna with an effective aperture A_r, for the normalized radiation diagram $Fn(\theta, \phi)$ with an incidental brightness of B (Θ, Φ); over a bandwith Δf (extending from frequency f to frequency $f + \Delta_f$) is the following:

$$P = A_r \int_f^{f+\Delta f} \iint_{4\pi} B_f\ (\theta, \phi) Fn\ (\theta, \phi)\ d\Omega\ df \qquad (2)$$

Where $B_f\ (\theta, \phi)$ measures the received power in directional distribution of the spectral brightness, which is not

constant with frequency. In atmospheric emission $B_f\ (\theta, \phi)$ is unpolarized, since the receptor antenna is polarized it will only detect half of the total power incident upon its surface and a factor of ½ should be applied.

$$\boldsymbol{P = \frac{1}{2} A_r \int_f^{f+\Delta f} \iint_{4\pi} B_f\,(\theta,\phi) Fn\,(\theta,\phi)\, d\Omega\, df} \qquad \textbf{(3)}$$

3.1.2 Blackbody radiation

All substances in gas, liquid, solid or plasma phase at a higher temperature above 0 K emit electromagnetic radiation.

According to the Quantum theory the transition of an atomic energy level to another lower energy level emits radiation. Collision of two atoms or particles results in emission of radiation. A collision will occur depending on the density of atoms and the kinetic energy of their random motion. The intensity of kinetic energy, or heat released by a substance increments with its temperature.

For understanding thermal emission of a real body it is necessary to introduce the concept of a blackbody radiator. A blackbody is defined as "*an idealized, perfect opaque material that absorbs all the incident radiation at all frequencies, reflecting none*". Besides being a perfect absorber, a blackbody is a perfect emitter, it is in a perfect thermodynamic equilibrium. At a certain temperature T the blackbody surface will absorb and emit photons at the same rate.

The blackbody emission follows the Planck's law; its radiation is uniform in all directions with a spectral brightness B_f:

$$B_f = (2hf^3/c^2)\left(\frac{1}{e^{\frac{hf}{kT}}-1}\right) \qquad \textbf{(4)}$$

where: B_f is the blackbody spectral brightness; W m^{-2} sr^{-1} Hz^{-1}, h is the Planck's constant equal to 6.63 x 10^{-34} joules, f is the frequency, c is the light velocity, k is the Boltzmann's constant and T is the black body's temperature.

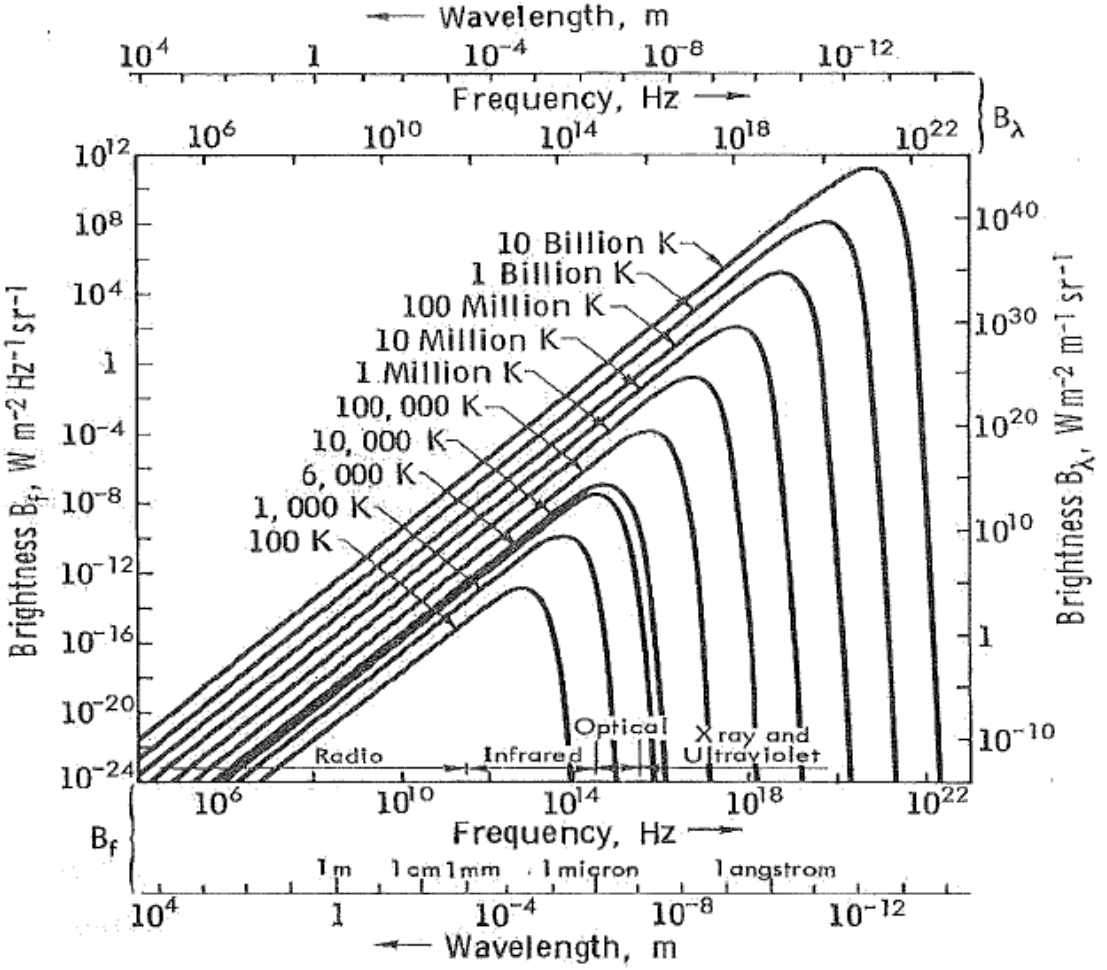

Figure 3-3: Brightness spectral density in relation to frequency for different Physical Temperature values

Figure 3-3 shows a set of Brightness curves following Plank's law (B_f, Hz) as a function of the frequency unit (Hz) at different Physical Temperature values (absolute temperature K). Two relevant trends are illustrated in the figure: a) an increase in T results in an increase in spectral brightness and b) the B_f maximum value increases with T.

The Wien radiation law can be applied for high frequencies. For microwaves, the low frequency counterpart of the Wien radiation, is the Rayleigh-Jeans Law, a simpler approximation of the Plank's law with a deviation error less than 1% if $\lambda T > 0.77$ m K or equivalent $f/T < 3.9 \times 10^8$ HzK:

$$Bf = \frac{2f^2kT}{c^2} = \frac{2kT}{\lambda^2} \qquad (5)$$

where $\lambda = c/f$ is the wavelength (m)

The Earth's temperature is estimated in 300K. For a blackbody with a 300K temperature, if $\lambda > 2.57$ mm or $f <$ 117 *GHz* covering the most usable microwave range, the fractional deviation from Planck law is 3%. For comparison of the Planck's law and its approximations for high and low frequency, see the Figure 3-4.

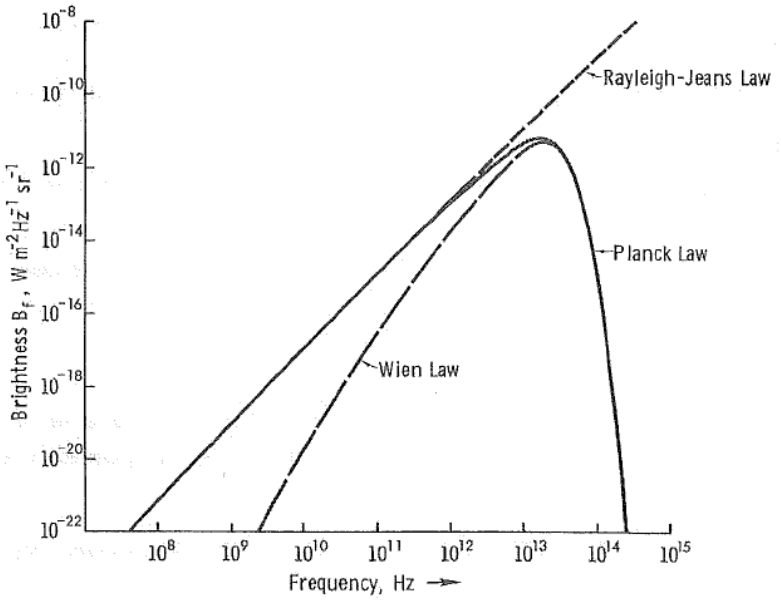

Figure 3-4: Comparison of Planck's low with the low frequency (Rayleigh-Jeans Law) and high frequency (Wien Law) approximations

In the microwave region, for a narrow bandwidth Δf, the brightness of a blackbody at a defined temperature T, is

$$B_{bb} = B_f \Delta f = \frac{2kT}{\lambda^2} \Delta f \qquad \textbf{(6)}$$

Considering a microwave antenna, the power received by emission of a blackbody as an integral with brightness directional distribution $B_f(\Theta, \Phi)$ it leads to:

$$P_{bb} = \frac{1}{2} A_r \int_f^{f+\Delta f} \iint_{4\pi} \frac{2kT}{\lambda^2} F_n(\theta, \phi)\, d\Omega\, df \qquad \textbf{(7)}$$

When B_f is approximately constant due to the narrow Δ_f ($\Delta_f << f^2$) the following is obtained:

$$P_{bb} = kT\Delta f \frac{A_r}{\lambda^2} \iint_{4\pi} F_n(\theta, \phi)\, d\Omega \qquad \textbf{(8)}$$

As the integral represents the solid angle Ω_p of the antenna, the equation becomes

$$\iint_{4\pi} F_n(\theta, \phi)\, d\Omega = \Omega_p = \frac{\lambda^2}{A_r} \qquad \textbf{(9)}$$

$$\text{and} \quad P_n = kT\Delta f \qquad \textbf{(10)}$$

This equation shows a highly significant concept in microwave remote sensing, that is, the direct linear relationship between power and temperature, which leads to the interchangeable use between units.

3.1.3 Radiation of a grey body

We have seen above that a blackbody is an idealized body in thermodynamic equilibrium. Nevertheless, real materials, also named grey bodies, do not absorb all the energy incident upon them, and thus emit less than black bodies. The brightness emitted for a grey material is defined as

$$B(\theta,\phi) = \frac{2k}{\lambda^2} T_B\,(\theta,\phi)\Delta f \qquad \textbf{(11)}$$

Where the brightness temperature $T_B\,(\theta,\phi)$, is the physical temperature of a blackbody equivalent radiometric temperature to produce $\mathrm{B}(\theta,\phi)$ brightness. It is not the real material temperature but the effective temperature.

The brightness $\mathrm{B}\,(\theta,\phi)$ of the grey body relative to that of a blackbody at the equal temperature is referred as emissivity.

$$e\,(\theta\,,\phi) = \frac{B(\theta\,,\phi)}{B_{bb}} = \frac{T_B\,(\theta\,,\phi)}{T} \qquad \textbf{(12)}$$

Therefore, the brightness temperature $T_B\,(\theta\,,\phi)$ of a grey body is smaller or equal to its physical temperature *T*, since the emissivity *e* is lower than 1, the material has a cooler brightness temperature than the physical temperature [9].

3.1.4 Power and temperature relationship

The apparent radiometric temperature (T_{AP}) is a blackbody equivalent temperature distribution referring to the brightness distribution $\mathrm{B}\,(\theta\,,\phi)$ of the energy incident upon the antenna.

$$B(\theta\,,\phi) = \frac{2k}{\lambda^2} T_{AP}\,(\theta,\phi)\Delta f \qquad \textbf{(13)}$$

With this equation and equation (2) brightness distribution of a grey body in the received power upon the antenna is

$$P = \frac{1}{2} A_r \iint_{4\pi} \frac{2k}{\lambda^2} T_{AP}(\theta,\phi)\Delta f F_n(\theta,\phi)\mathrm{d}\Omega \qquad \textbf{(14)}$$

The brightness temperature T_B refers to the radiation released from a surface or volume, considering a semi-finite homogenous material. On the other hand apparent temperature T_{AP} is related with the radiation incident energy upon the antenna. Generally, T_{AP} will be different from T_B, in the exceptional case of no extraterrestrial emission and lossless atmosphere $T_{AP=}\,T_B$.

As mention earlier, there is a direct linear relationship between power and temperature, therefore the power provided by the antenna to the receiver by a grey body is

$$P = kT_A\,\Delta_f \qquad \textbf{(15)}$$

Based on equation (14) T_A leads to

$$T_A = \frac{A_r}{\lambda^2} \iint_{4\pi} T_{AP}(\theta,\phi) F_n(\theta,\phi) d\Omega \qquad \textbf{(16)}$$

For the antenna shown in the following picture (Figure 3-5) radiation incident upon the antenna could contain components such us self-emitted terrain radiation T_B, self-emitted atmosphere up-ward radiation T_{UP} and downward radiation T_{DN} reflected by the terrain to the antenna. However both, terrain emitted and self-emitted radiations are attenuated as they propagate from the terrain to the atmosphere.

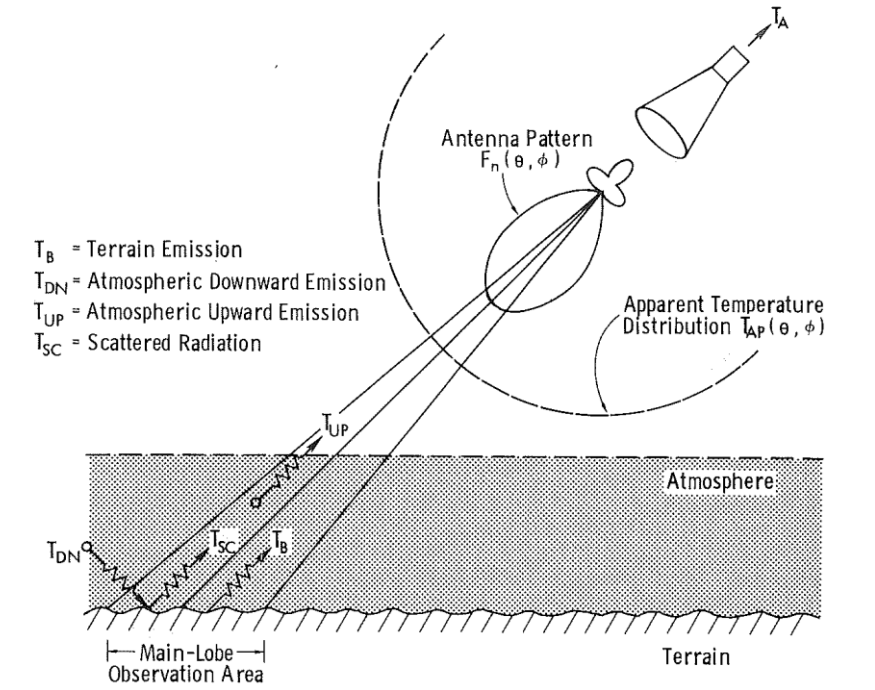

(a)

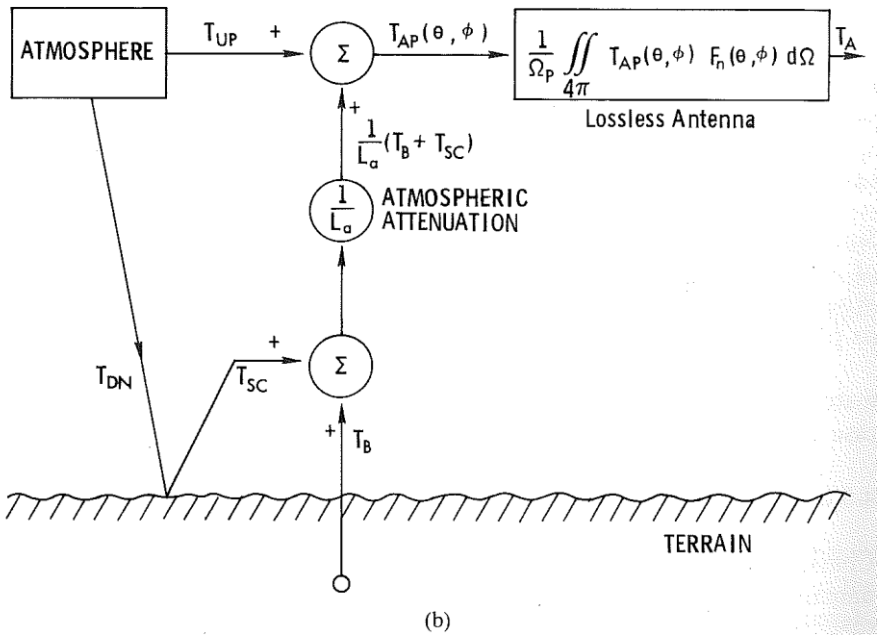

(b)

Figure 3-5: Correlation between antenna temperature, apparent temperature and brightness temperature a) Incident upon antenna b) block diagram

Apparent radiometric temperature distribution T_{AP} can be expressed as a function of temperatures (upwards T_{UP} , brightness T_B and scattering T_{SC}). T_{SC} represents the proportion of the radiation impinging on the terrain surface from the upper hemisphere that is scattered by the terrain surface with an attenuation factor (L_a).

$$T_{AP}(\theta, \phi) = T_{UP} + (T_B + T_{SC}) \cdot \frac{1}{L_a} \quad \textbf{(17)}$$

Atmospheric effects can be dismissed at low frequency. Soil moisture is measured a low frequency.

3.1.5 Measurements of Brightness temperatures from space

Radiometers are highly sensitive receptors, that measure antenna radiometric temperature, representing the radiation power delivered by the antenna to the receiver [9]. The performance of a radiometer is measured by its accuracy and precision.

The Accuracy is determinated by the similarity between the antenna temperature measured by the receiver and its real value. In other words the output voltage measured as a linear function of noise temperature of the input terminal in the antenna.

In the other hand, precision, referred as radiometric sensitivity, is the smallest variations in brightness temperatures that the radiometer is able to detect.

The performances of space radiometers is considered based not only on accuracy and precision but also on spatial resolution, meaning the capability of the sensor to discriminate among nearby sources [10].

3.2 Scatterometry

Scatterometers are a form of radars that measure the geographical characteristics of surface and volume with microwave electromagnetic pulses of different amplitudes transmitted from and scattered back to the spacecraft antenna. It is referred as Scatterometer since it measures the backscattered pulses. Initially, radars where based on radio waves reflection. The first spaceborne radar mission, back in 1950, had the mission to gather information on politically enemy regions.

In general, by sending and receiving the returning of their own pulses, radars can measure their duration, frequency and/or amplitude. Additionally, they can infer surface or volume characteristics from the scattered pulse that is received by the radar antenna. The life of the radar instrument is conditioned by the amount of power that the radar satellite can store and generate. The radar pulse is generally in the microwave region of the electromagnetic spectrum, which broadly ranges in wavelength from 1 mm to 1 m. Radars which measure the power, or amplitude, of the return pulse scattered back to the antenna are known as Scatterometers. Since it uses its own power to generate pulses from the sensor, Scatterometers are considered active remote sensing.

Scatterometers function indepently of the presence of sunlight; they can operate at day and night. Radars have the ability to controls the angle at which pulses are transmitted. Radars can transmit multiple pulses concurrently permitting to collect a great quantity of information at once.

Scatterometers have coarser resolution (50-100 km) compared to most radars which gives them the advantage of covering a larger portion of the globe on a frequent basis which is a benefit for monitoring large scale phenomena such as global ocean winds and snow cover, continental ice sheets, and polar sea ice extent.

The physics of scatterometry remote sensing is expressed as the "**radar equation**":

$$P_r = (P_t G_t / 4\pi R^2)\sigma_{rt}(A_r / 4\pi R^2) \qquad \textbf{(18)}$$

where: P_r is the received power, P_t is the transmitted power, G_t is the gain of the transmitting antenna in the direction of the target, R is the distance between the target and the antenna, σ_{rt} is the radar cross-section: the area of the target intercepting the transmitted pulse that produces a return pulse equal to the received power and A_r is the effective receiving area of the receiving antenna aperture.

In the equation, the first parenthesis describes the total amount of transmitted power reaching a given target. It is multiplied by the radar cross-section (σ_{rt}) defining the transmitted power. While the second parentheses, defines the total amount of backscattered energy that is received at the radar antenna.

Factors: P_t, G_t, and A_r are all known quantities related with the radar system, while R is associated with the distance to the target and can be determined based on the time that the transmitted pulse to return to the antenna. The radar cross-section, σ_{rt}, is a function of the way the transmitted electromagnetic energy interacts with the surface. When this quantity is integrated over a number of pulses, it is referred to as the "scattering coefficient," or "backscattering coefficient," and is commonly denoted as σ^o. The primary variable that scientists work with when using scatterometry data is the quantity σ^o (in decibels (dB)), used to derive geophysical parameters.

The σ^o value is determined by **roughness** and its **dielectric properties**. For a pulse to be scattered back in the same direction that it comes, the surface has to be rough. If that happens, the radar antenna detects the pulse. When the surface is rough, the value of σ^o is higher.

The **Rayleigh roughness criterion**, considers the surface to be rough according to the following equation:

$$h > (\lambda / (8 \sin \Upsilon)) \qquad \textbf{(19)}$$

where: h is the vertical relief of the surface roughness features, λ is the radar wavelength and Y is the depression angle of the radar pulse.

For example with a radar a 2-cm wavelength (or 15 GHz frequency) at a 50° depression angle would only be backscattered if the surface had features with a minimum vertical relief of about 3 mm. Figure 3-6 shows a schematic representation of the radar backscatter response to different surface roughness.

Surface roughness impacts on σ^o over a range of "**incident angles**." On the other hand, smooth surfaces have a

mirror-like, or "**specular**," reflection, a radar satellite will only measure a return signal at nadir, with an incident angle of 0° to the target. However, if the target is an extremely rough surface, it scatters the signal so that the antenna receives approximately equal amount of power (regardless of incident angle). This kind of surface is referred to as "**isotropic**," and the return signal is considered "noncoherent" as opposed to coherent or specular. Intermediate rough surfaces vary in their angular response of σ^o between the specular and isotropic examples, as illustrated in Figure 3-7. [6]

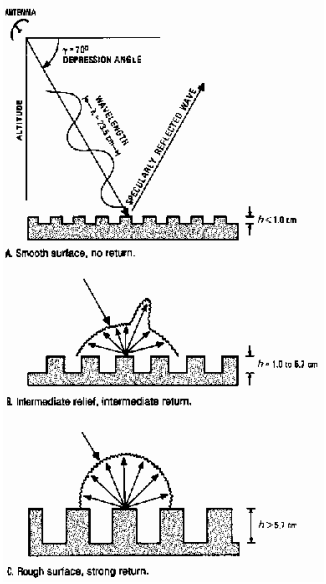

Figure 3-6: Response of radar backscatter to different surface roughness criteria: (a) smooth, (b) intermediate, and (c) rough (Sabins, 1997)

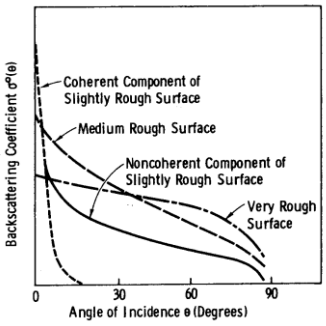

Figure 3-7: Angular variation of backscatter for different roughness conditions [9]

Moreover, besides roughness, the dielectric properties of surface materials also have an impact on σ^o. The **dielectric constant** is an electrical property that effects the interaction between matter and electromagnetic energy and is a function of temperature and wavelength. This quantity is expressed in real and imaginary components, with the former representing the amount of energy that the medium scatters while the latter represents the amount of energy absorbed [6]. If liquid water is present, it strongly increases the dielectric constant in the microwave region, making σ^o sensitive to moisture. Due to this characteristic of radar remote sensing it makes scatterometry a very useful tool for the detection of snow and ice melting, and for the measurement of soil moisture

and vegetation water content.

The quantity of σ^o averages the result of several return pulses and it is more accurate because of the high level of noise present in any single return pulse. Figure 3-8b illustrates the process of "fading", which explains the distortion caused by the interference between the pulses from multiple ground targets. In Figure 3-8a it is presented a case where two targets are situated at a distance D from each other. Figure 3-8b shows how the sum of both signals oscillates between peaks and troughs, as a result of constructive and deconstructive interference. When there are more targets that interfere, the scenario is more similar to Figure 3-9, where the return pulses experience fading.

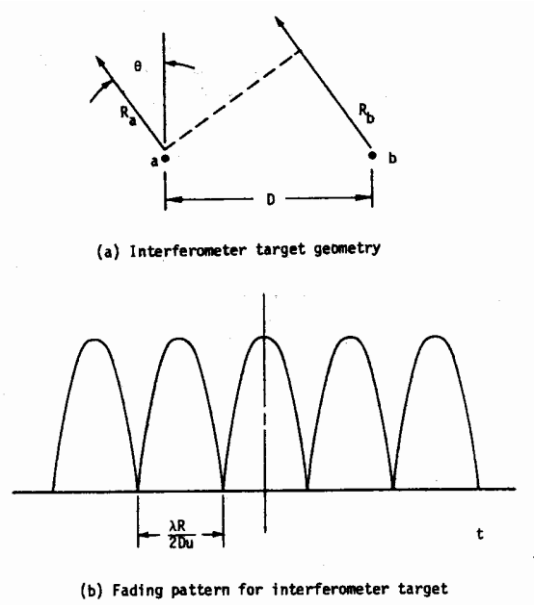

Figure 3-8: Simplified target fading (Moore, et al 1983)

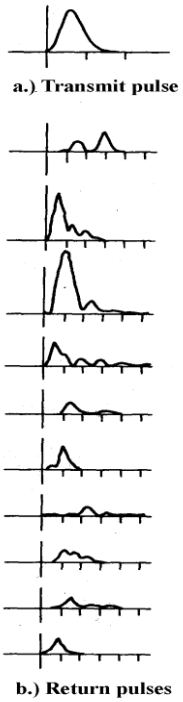

Figure 3-9: Sequence of pulses returned to the receiver showing the fading (variability of signal levels) on a pulse-to-pulse basis (Moore, et al 1983)

The averaging of a considerable number of return pulses has the effect of cancelling out these variations, also referred as noise, caused by fading so that an accurate measurement of σ^o can be made. A ± 0.10 – 0.15 dB accuracy can be achieved by the Scatterometers when applying this method. However, the trade-off of averaging together multiple return pulses, is a reduction in the spatial resolution. This explains why SARs can achieve 1-10 km resolution while scatterometers typically have 25-50 km resolution. Because SAR instruments are used primarily for topographic imaging and altimetry, they are concerned with measuring the duration it takes for a pulse to return from a target and not with measuring its amplitude.

Noise is not a concern, then, for SAR remote sensing and the fine spatial resolution achieved with single pulses can be exploited [6].

Scatterometer systems collect measurements at multiple incident and azimuth angles. An incident angle measures the vertical angle between the direction directly below the satellite platform (0°) and parallel to it (90°). An azimuth angle measures the horizontal angle between the forward direction (0°) of the satellite and the direction to its rear (180°), with 90° to its right and 270° to its left [6]. Various scatterometers use a different approach to collect data from multiple angles is referred as the "fan-beam" approach. That is, it fans out, or points, several fixed-angle "beams" of radar pulses at the ground simultaneously (Figure 3-9). A "pencil-beam" approach is a different approach which rotates a single beam of pulses at multiple angles

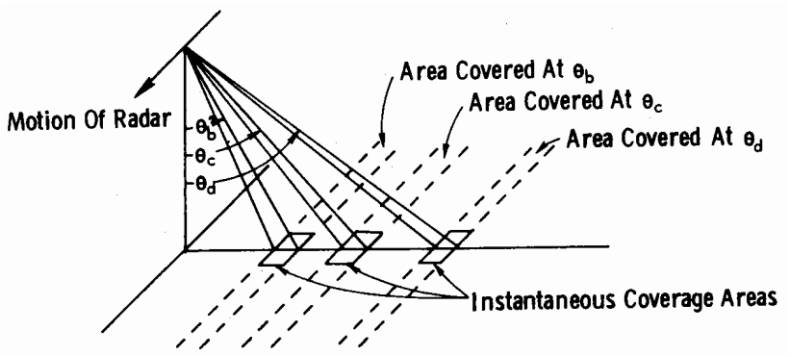

Figure 3-9: Example of a fan-beam scatterometer [8]

Aquarius L-band Scatterometer is called ALScat. ALScat is a simple real-aperture radar without the requirement of pulse-to-pulse coherence. It is a total-power dual-polarized L-band (1.26 GHz), designed to measure backscatter from the ocean surface. Its measurements will enable the removal of wind effects from the Aquarius radiometer (ALRad) brightness temperature measurements being used to retrieve ocean salinity. The ALScat requirement calls for great stability with repeatability on the order of 0.1 dB over several days, and calibrated accuracy to this level over several months. The Scatterometer signal is rotated among three feeds and two polarizations. The operation consists of a 6 steps at each the feeds: (1) transmit H-pol and receiving at V-pol; (2) receive at V-POL (noise only); (3) transmit at V-pol and receive at V-pol; (4) transmit at V-pol and receive at H-pol; (5) receive at H-pol (only noise); (6) transmit at H-pol and receive at H-pol. The result are the different backscatter measurements at HV, VV, VH and HH together with the measurement of noise. After the ground processing, once the total power is known (HV + VV + VH + HH), the roughness correction for the radiometer is retrieved.

Another feature needed for the scatterometer is a Thermal control for keeping the temperature of the electronics within about 1ºC.

3.3 Emission at L-band

Terrain emission depends on the dielectric constant of the terrain which is influenced by the Earth's surface moisture, its temperature, the roughness of its surface, the vegetation density and its surface type.

3.3.1 Thermal radiation or brightness temperature

The simplest scenario for microwave emission is considering a homogenous terrain medium and constant temperature, particularly in this case the brightness temperature of surface $T_B\,(\theta_1, p)$ is

$$T_B\,(\theta, \phi) = e^p(\theta_0\,, p) \cdot T = \,[1 - \,\Gamma^p\,(\theta_0, p\,)] \cdot T \qquad \textbf{(20)}$$

Where T is ground physical temperature and $e(\theta_1, p)$ is the emissivity and P polarization. Figure 3-11 represents the emissivity for several types of material as a function of incident angle, for vertical or horizontal polarizations at 10 GHz [9].

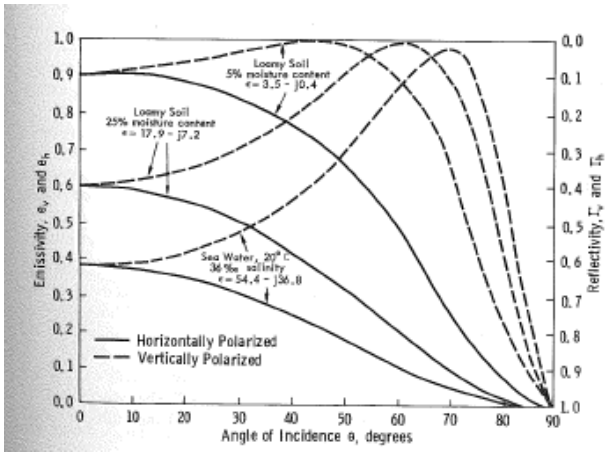

Figure 3-10: Calculated reflectiveness and emissivity as function of incidence angle for a defined 10 GHz

3.3.2 Surface scattering

Electromagnetic waves impacting upon a boundary surface that separates to semifinite media outcomes in an incident energy that is scattered backwards and a transmitted forward energy into the medium. See the schematic Figure 3-12 of surface scattering patterns.

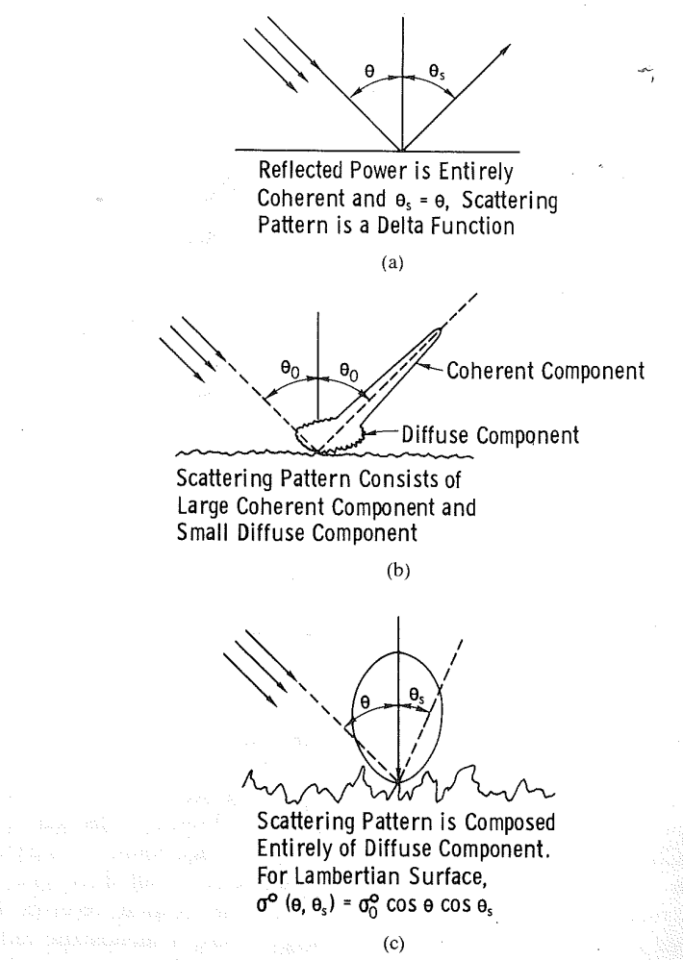

Figure 3-11: Scattering (coherent and diffuse) in specular slightly rough and very rough conditions.

When the transmitter and the receiver are in the same radar, it receives the backscattered energy of the scattered emission. The contributions of scattering patterns are shown for different surfaces roughness [9].

Roughness of a surface is measured in wavelengths units which represent: the standard deviation of the surface height variation (rms height, cm) and the surface correlation length.

Normalized antenna temperature is the measured temperature divided by the physical temperature of the ground surface. The Figure 3-13 shows the values of normalized antenna temperatures for a given frequency of 1.4 GHz. Three different surface-roughness conditions for vertical and horizontal polarization as a function of the incident angle are considered [9].

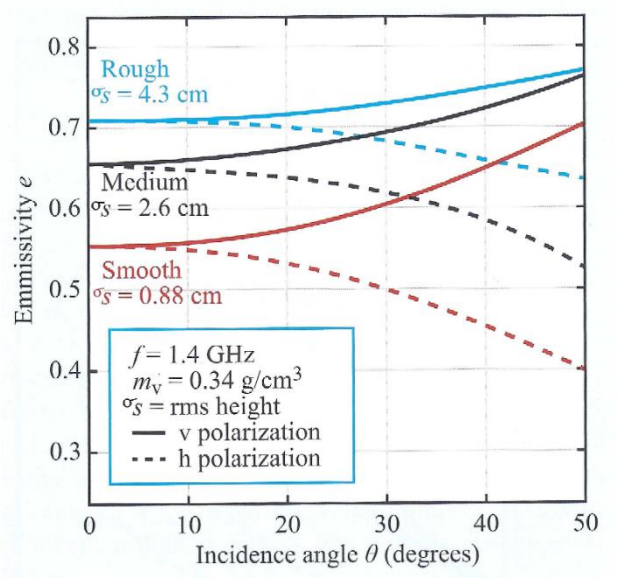

Figure 3-12: Bare soil field with different roughness. Angular patterns for normalized antenna.

Increases in terrain roughness correlate with overall increases in horizontal and vertical polarized emissivity.

According to the single parameter model of Choudhury [11], emissivity is as follows:

$$e_r(\theta) = 1 - \Gamma_r^{sp}(\theta)\, e^{-h' \cos^2 \theta}, \text{ r = h or v,} \qquad \textbf{(21)}$$

For a r polarized index, $\Gamma_r^{sp}(\theta)$ polarized specular surface reflectivity, Θ angle of incidence and h' the roughness.

A more elaborated model was proposed in 1981 by Wang and Choudhury [12].

$$\Gamma_{sp} = \left[(1 - Q_s) \cdot \Gamma_{op}(\theta) + Q_s \Gamma_{oq}(\theta)\right] \cdot \exp\left(-h_s \cdot \cos^n(\theta)\right) \qquad \textbf{(22)}$$

where Q_s models the effect of mixed polarization, h_s and n model terrain roughness and Γ_o is the reflection coefficient (calculated by the Fresnel equation) for a p and q with orthogonal polarization (vertical and horizontal).

The next figure illustrates the brightness temperature for 3 different frequencies and different surface roughness and soil moisture.

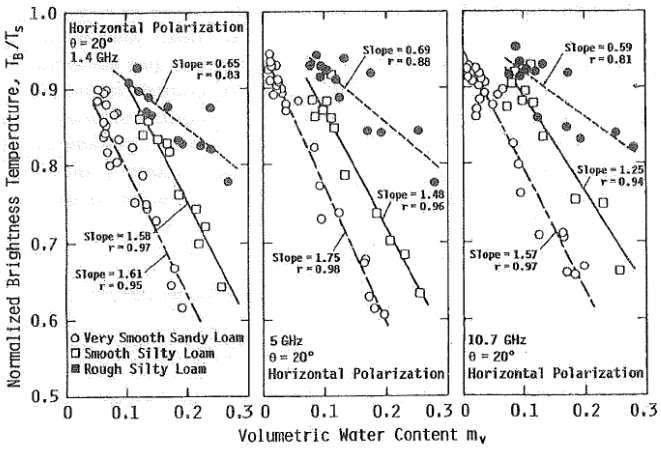

Figure 3-13: Variations in brightness temperatures as a function of volumetric water content

3.3.3 Dielectric Soil Properties

Dielectric constant is a measurement of the soil response to an electromagnetic wave, and allows to correlates soil emission, microwave frequency and moisture.

$$\epsilon_s = \epsilon_s' + j \cdot \epsilon_s'' \qquad \textbf{(23)}$$

Where the real part represents soil energy propagation and the imaginary part represents the loss of energy due to water concentration, rocs, air, soil structure, temperature and salinity among others.

3.3.4 Soil Moisture

For the purpose of this project it is necessary to define soil moisture. According to the European Space Agency (ESA): "soil moisture refers to the water held in the spaces between soil particles. Primarily, soil moisture is a function of rates of evaporation and precipitation, although the type of soil and vegetation cover also influences the rates at which water filters through the soil and runoffs off the surface." Soil Moisture variations drive ocean circulation patterns, which in turn, moderate climate by bringing warm surface waters to higher latitudes and cool deeper waters back to equatorial regions". For example, increased moisture content of the atmosphere is expected in warmer climate with alterations in evaporation which has an effect on weather patterns and implications on water consumption and agricultural [4].

Space satellites improve the knowledge of global water cycle. In addition to space measurements, gauge ground estimations are also taken to reassure satellites deliver accurate information.

A global perspective of water, measured from the space, is a cornerstone for the advancement of water science also refereed as hydrology. Hydrology has evolved as a very relevant science in response to understanding the water system of the earth and solving water problems. Progression in water knowledge, collecting data, understanding the challenges, and gathering the adequate information was foresee as a need by the National Aeronautics and Space Administration NASA stating that: "improves the ability to manage water and to provide

the water-related infrastructure that is needed to provide for human needs and to protect and enhance the natural environment and associated biological systems" [2]. Water state in soil (frozen or thawed), has implications on carbon cycle. For example modifications in spring thaw and variations in expansion of season's duration will aid the scientific community to define more precise the quantity of carbon, plants are removing from Earth's atmosphere each year.

3.3.4.1 Bare Soil

Scientific observations of bare soil surface microwave emission show that brightness temperatures decrease with soil moisture content.

This figure shows the brightness temperature T_B impact at a fix 1.4 GHz for soils with differences in moisture content (m_f) of the top first centimeter surface layer. The percentage of field capacity (FC) defined for 3 sets of soil textures (FC< 23; 23≤FC<30;FC ≥30).

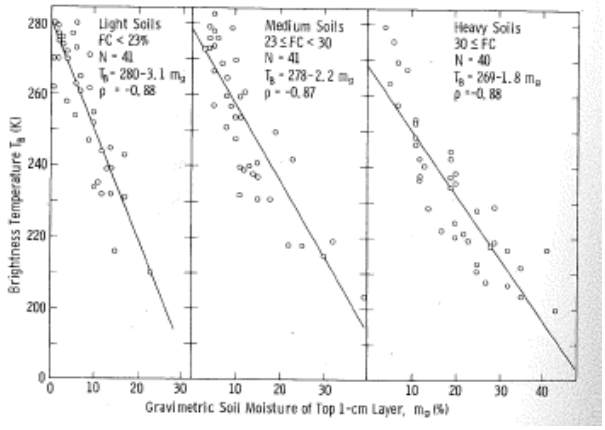

Figure 3-14: T_B in relation to weight percent of soil moisture for three soil textures according to FC values.

3.3.4.2 Vegetation covered Soil

Emission is affected by soil vegetation. The vegetation layer results in attenuation of soil radiation and can cause diffuse scattering of soil and self-emission. Absorption will depend on the wavelength and vegetation water content.

Brightness temperature of vegetation covered soil is estimated with 3 three parameters: a) attenuated soil emitted radiation; b) reflectivity of vegetation upwards (air- vegetation boundary) and; c) reflectivity of vegetation downwards (vegetation soil boundary), that will be reflected and again attenuated by the vegetation layer.

$$T_B = \left(1 + \frac{1-e_{sp}}{L_v}\right)\left(1 - \frac{1}{L_v}\right)(1-\omega)T_v + \frac{e_{sp}}{L_v} \cdot T_s \qquad \textbf{(24)}$$

Where T_s is the physical temperature of soil surface, T_v is the physical temperature of the vegetation layer, L_v = exp (τ / cos Θ) is the attenuation of the vegetation layer, $\tau = b \cdot VWC$ is vegetation opacity, b depends on the

vegetation type and frequency, *VWC* is the vegetation water content, ω is the soil emissivity reflected by the vegetation that depends on the polarization and angle of refraction. In addition, soil emissivity e_{sp} is defined as

$$e_s = 1 - \Gamma_{sp} \qquad (25)$$

The next Figure 3-15 shows the brightness temperature as a function of the incident angle for vertical and horizontal polarization for three soil patterns: dry, moist and wet. Differences between bare soil and vegetation covered soil are shown in Figure 3-15 *a* and *b* respectively. For bare soil and vertical polarization, an increase in incidence angle results in an increase in brightness temperature and the contrary results for horizontal polarity. On the other hand, for vegetation covered soil, the differences in brightness temperature are reduced between both vertical and horizontal polarization, and within the three classes of soil.

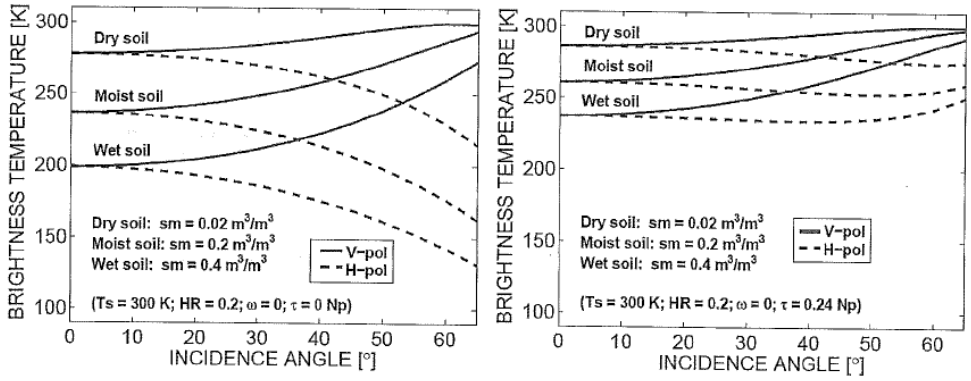

Figure 3-15: Brightness temperature versus incidence angle for bare soil (a) and vegetation covered soil (b), and three different classes of soil moisture [13].

4 SATELLITE MISSIONS

There are two main satellite missions that are dedicated to monitoring the temporal spatial variation of the Earth's Soil Moisture: SMOS and SMAP. Also, a third mission: Aquarius/SAC-D, retrieved Soil Moisture data during four years. The three missions worked at L-band frequencies and only Aquarius/SAC-D satellite, combined passive and active measurements for a long period. This thesis chapter explains the three missions and the different features of each satellites.

4.1 SMOS (Soil Moisture and Ocean Salinity)

The European Space Agency (ESA), initiated its first Earth observation mapping with the Meteosat meteorological satellite in 1977.

Since then, ESA created the ESA's Living Planet Program, which includes the Earth Explorer missions, and an Earth Watch element to collect Earth observation data for hydrological studies and progress on humankind by addressing key scientific challenges.

SMOS is the ESA's water satellite; it measures Soil Moisture and Ocean Salinity. Its mission was to determine global observations on Earth's soil moisture and salinity on the sea surface. A combination of this two parameters provides an understanding of the water cycle processes between Earth landmark and the atmosphere, with the aim of improving weather and climate models.

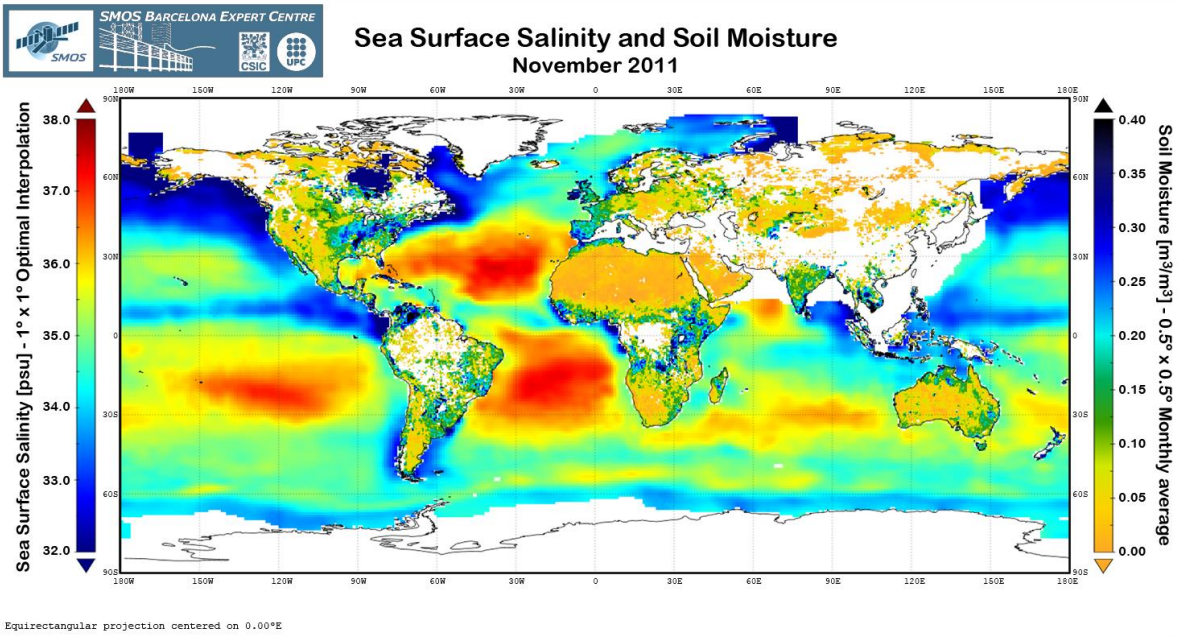

Figure 4-1: This image combines ocean salinity measurements with soil moisture data. It represents both variables during November 2011

SMOS has distributed the longest continuous information of ocean salinity from the space. The satellite was launched on the 2nd of November, 2009, as a 5 year mission but it was extended up to 2017 due to the relevance of the information and the opportunity of synergies with other new ESA programs. For instance, SMOS is capable of providing data to measure thin ice floating in the polar seas accurately enough for forecasting and ship routing.

SMOS describes a low-Earth, polar sun-synchronous orbit. The satellite is formed by a unique interferometric radiometer operating in the L-band microwave range that has the function to capture 'brightness temperature' images. These images are combined to have a global map of soil moisture every 3 days. SMOS radiometer (MIRAS), consists in three deployable arms that have 69 antennas. The accuracy of its Soil Moisture product is of 4% with a spatial resolution of, approximately, 50 km. On the oceans, SMOS maps salinity down to 0.1 practical salinity units (PSU, averaged over 10–30 days in areas measuring 200 × 200 km). New applications have been added to the initial mission of Earth water cycle. SMOS has been adapted to provide observations of snow and ice.

Full name	**Soil Moisture and Ocean Salinity mission**
Launched	2nd of November, 2009, at 02:50 CET from the Plesetsk Cosmodrome, Russia.
Launcher	Rockot by Eurockot Launch Services GmbH.
Satellite	Proteus platform adapted to the needs of SMOS.
Instrument	Microwave Imaging Radiometer using Aperture Synthesis (MIRAS), 2D interferometric L-band

	radiometer operating at 1.4 GHz (21 cm wavelength), with 69 antenna receivers distributed on a Y-shaped deployable antenna array and central hub.
Mass	658 kg (platform: 275 kg, payload: 355 kg, fuel: 28 kg).
Power	Deployable solar panels with Si-cells, Li-ion battery. Maximum power available for satellite: 1065 W, maximum consumption for MIRAS payload: 511 W
Orbit	Mean altitude of 758 km and inclination of 98.44°; Sun-synchronous, quasi-circular, dusk-dawn, 23-day repeat cycle, 3-day sub-cycle.
Mission control	Via the CNES French space agency's ground station in Toulouse, France. S-band uplink and downlink for satellite health and housekeeping data and telecommanding through ground station network in Kiruna (Sweden), Aussaguel (France) and Kourou (French Guiana).
Data processing	Data Processing Centre at ESA's European Space Astronomy Centre (ESAC) in Villafranca, Spain; long-term archive at Kiruna; User Services via ESA's Centre for Earth Observation (ESRIN) in Frascati, Italy.
Nominal life	Three years (including a six-month commissioning phase). Extended to 2017.
Project	Mission development and commissioning managed at ESA's European Space Research and Technology Centre (ESTEC) in Noordwijk, the Netherlands. This involved more than 20 European companies and hundreds of technicians and engineers around Europe.
Prime contractors	Spain's EADS CASA Espacio for the MIRAS instrument. Thales Alenia Space Industries (France) and CNES were responsible for the Proteus platform.

Table 4-1: SMOS facts [10]

4.2 SMAP (Soil Moisture Active Passive)

Following the 2007 report by the National Research Council's Committee "Earth Science and Applications from Space: National Imperatives for the next Decade and Beyond", NASA launched the Soil Moisture Active Passive Satellite mission on January 31st, 2015. SMAP is a 3 year mission satellite with two main objectives. First of all, to provide global mapping of high-resolution soil moisture. Secondly, to detect if soils are frozen or thawed. The results of the mission also have an impact on hydrogen, ecology, forecasting of flood, drought monitoring and numerical weather prediction. Therefore, SMAP contribution is very valuable in science and applications disciplines.

On July 7th, 2015, SMAP's radar transmissions stopped due to an irreparable hardware failure of the radar high-power amplifier. The radiometer became the only transmission of soil moisture from the satellite.

This Earth observing satellite has an inclination of 98 degrees and it is orbiting around the earth at an altitude of 685 km. It describes a sun-synchronous near-polar orbit with ascending node time of 6 P.M. Almost every 3 days

it completes the global coverage with an exact 8 days repeated cycle. The differences in microwave emissions caused by water in soil are captured by the radiometer as brightness temperature, in Kelvins, emission. The Satellite captures and measures this emission at a horizontal spatial resolution of 40 km [14]. It has a mesh reflector antenna of 6 meters that provides high-resolution, high-accuracy and L-band passive radiometer state. The shared antenna is the most prominent characteristic of the satellite.

By combining the active and passive microwaves observations with SMAP wide swath, it had the capacity to measure both soil moisture and frozen/thaw with high accuracy, high resolution, and global coverage. Specialists unify both radiometer and radar sensor data to obtain profit on the solidity of each. SMAP's radar had a soil moisture product with a spatial resolution of 3 kilometers, however this measure was less precise than the radiometer. Radiometer by itself has an accurate measurement of soil moisture, nevertheless with less spatial resolution of 40 kilometers. The combined active/passive microwave soil moisture product has a spatial resolution of 10 km and a mean latency of 24 hours [14].

Satellite Platform	**SMAP**
Altitude	685 km
Equator Crossing Time	6pm ascending /6am descending
Antenna Size	6.0 m
Swath Width	1000 km
Orbit Inclination	98 deg
Off-Nadir View Angle	40.0 deg
Resolution	40 km
Repeat Cycle	7 days

Table 4-2: Principle features of SMAP [12]

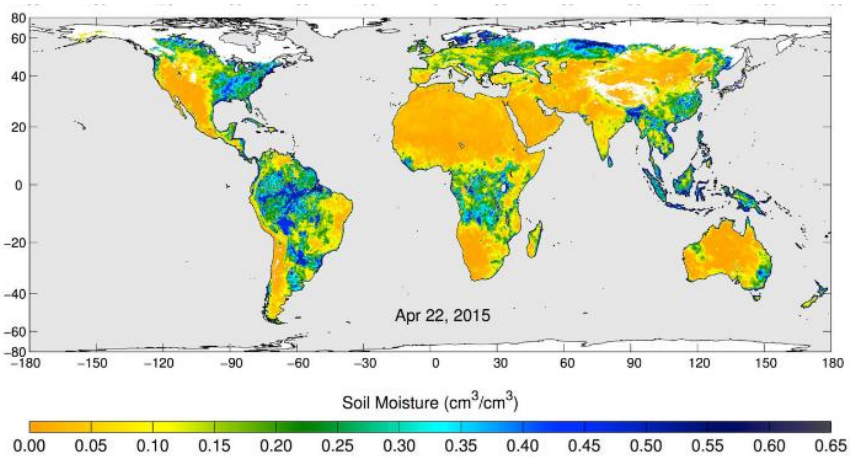

Figure 4-2: Global map of SM product

Figure 4-2 shows a global soil moisture map that was created using data from 3 days of the radiometer observations. Wetter areas are blue and drier areas are yellow. White areas indicate snow, ice or frozen ground [14].

One of the responsibilities of the Scientists SMAP Team is to validate SMAP soil moisture measurement with in situ measurements. Field teams work at selected locations. Their duty is to stick probes into the ground and measure water in the 5 top centimeters of the soil surface. In words of Tom Jackson, SMAP Science Team calibration/validation lead and research hydrologist at the USDA. "Field experiments are one of the most demanding parts of validation in terms of human and fiscal resources. Therefore, they must be well designed and focused on specific objectives." [14].

This Thesis started as an invitation from Monash University to participate in the Soil Moisture Active Passive Experiments -5 campaign in Yanco, Australia. 612 kilometers west of Sydney, scientists analyzed the ground as part of the SMAPEx-5 from 7th September to 27th September. Field teams also measured the land's vegetation coverage and surface roughness.

4.3 Aquarius/SAC-D

The purpose of Aquarius satellite is to understand how oceans respond to climate changes and the role of water cycle in ocean circulation and climate. Aquarius mission is to measure global sea surface salinity (SSS) or concentration of dissolved salts, the impact of soil wetness that fluctuates with the seasons and weather phenomena.

It is the first satellite mission specifically designed to provide monthly global measurements of how sea water salinity varies at the ocean surface, which is a key to studying the links between ocean circulation and global water cycles. Variations in ocean surface salinity are a key area of scientific uncertainty. Salinity variations modify the interaction between ocean circulation and the global water cycle, which in turn affects the ocean's capacity to store and transport heat and regulate Earth's climate. The Aquarius Mission seeks to determine how the ocean responds to the combined effects of evaporation, precipitation, ice melt and river runoff on seasonal and inter-

annual time scales, and their impact on the global distribution and availability of fresh water. Sea surface salinity, along with sea surface temperature, determines the sea surface density. Recent technological advances have provided the ability to examine these processes using remote sensing tools via satellite, and will further understanding of how climate variations induce changes in the global ocean circulation and how our oceans respond to climate change and the water cycle.

The satellite was named Aquarius following the Water Bearer constellation due to its aim to explore the role of the water by observing the natural thermal emission from the ocean surface with radiometers. These passive sensors are designed to detect and measure a particular wavelength of microwave energy being emitted by the ocean. The radiometers on Aquarius measure the microwave emissions from the sea surface at 1.4 GHz in the L-band portion of the electromagnetic spectrum. This energy, which is measured as an equivalent temperature called the "brightness temperature" in Kelvin, has a direct correlation to surface salinity.

By using frequencies close to the ones used in microwave ovens, it captures natural thermal emissions from the ocean surface; a salinity dependent signal of the ocean water and temperature. The microwave energy, measured as an equivalent “brightness” temperature in Kelvin and has a direct correlation to surface salinity. Salty water is seen cooler than freshwater. The satellite has the capacity to discriminate with high precision the changes in SSS of a “pinch” (i.e., 1/6 of a teaspoon) of salt in 1 gallon of water.

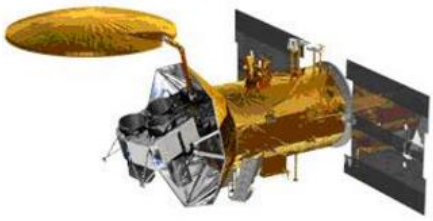

Figure 4-3: Aquarius/SAC-D satellite illustration

The spacecraft is constituted by 3 radiometers operating at 1.4 GHz. The data collected by the radiometer are being used together with sea surface temperature collected from another platform(s), to derive salinity data. Aquarius also includes a scatterometer operating at 1.2 GHz. The reason why it was incorporated was because there were many interferences with the salinity signal Aquarius was measuring, such as land effects, atmospheric noise and Ocean waves. The scatterometer sent a radar pulse to the ocean surface that was reflected back to the spacecraft, providing information about the ocean surface.

A description of the Aquarius SAC-D instrument is shown in the Table 4-3:

Instrument	Objectives	Specification	Resolution	Owner
Aquarius	Understanding ocean circulation, global water cycle and climate interaction. Soil moisture measurements over Argentina	Integrated L-band radiometers (1..413 GHz) and scatterometer (1.26 GHz)	Three beams: 76 km x 94 km, 84 km x 120 km, 96 km x 156 km	NASA
MWR	Precipitation rate, wind speed, sea ice concentration, water vapor, clouds	23.8 and 37 GHz, H+V polarization; Bandwidth: 0.5 and 1 GHz; Swath: 390 km	40 km	CONAE
NIRST	Hot spot events, SST (Sea Surface Temperature) measurements	3.8, 10.7 and 11.7 µm bands; Swath of 180 km Tilt: ± 470 km	350 m	CONAE, CSA (Canada)
HSC	Urban lights, electric storms, polar regions, snow cover	0.45 - 0.9 µm Swath: 700 km	200-300 m	CONAE
DCS	Data Collection System	401.55 MHz uplink	2 contacts/day from 200 platforms	CONAE
ROSA	Atmospheric properties	GPS occultation techniques	300 km horizontal 300 m vertical	ASI (Italy)
CARMEN-1 composed of ICARE and SODAD	I: Effect of cosmic radiation in electronic devices, S: distribution of microparticles and space debris	I: three fully depleted Si and Si/Li detectors S: four SMOS sensors	I: 256 channels S: Sensitivity 0.5 part at 10 km/sec	CNES (France)
TDP (Technology Demonstration Package)	Position, velocity and time determination, inertial angular velocity	GPS receiver, Inertial Reference Unit	20 m, 1 m/s, 2 m/s ARW: 0.008º/sqrt h	CON

Table 4-3: Overview of payloads instruments on the Aquarius/SAC-D mission

This satellite combined information of water cycling and ocean circulation and collected much more information than water sensors and boats have been able to do in 125 years. Aquarius yield for the first time a new mean global salinity map at higher spatial resolution than existing data and provided complete observations during an annual cycle. The satellite reported high quality data with surface salinity variation at much smaller scales than expected (EOS: Satellite Mission Monitors Ocean Surface Salinity Vol. 93, No. 25, 19 June 2012). Mapping Ocean surface salinity observations in a monthly basis gave information of changes in freshwater input and output to the ocean related to precipitation, evaporation, ice melting, and river runoff. It also gave information on the formation and travelling of enormous water masses responsible of the regulation of ocean circulation and Earth's climate.

Initially Aquarius was constructed by the NASA and was followed by the Aquarius/Satélite de Aplicaciones Científicas (SAC)-D Spacecraft, a collaboration between NASA and Argentina's space agency, where other countries participated including Brazil, Canada, France and Italy. Fruit of this collaboration was new microwave radiometer that ensured to obtain data during heavy rain falls at the same time that it gauged salinity. The 10th June, 2011, the Aquarius/ SAC-D mission was launched to the space. Although the initial mission was focused on the salinity of the ocean surface water, it was extended to include soil moisture measurements.

Soil Moisture data helps Scientifics to better understanding the climate system. For instance, it provides information for advancing climate models, weather forecasts, drought monitoring and flood prediction to informing water management decisions and aiding in predictions of agricultural productivity [15].

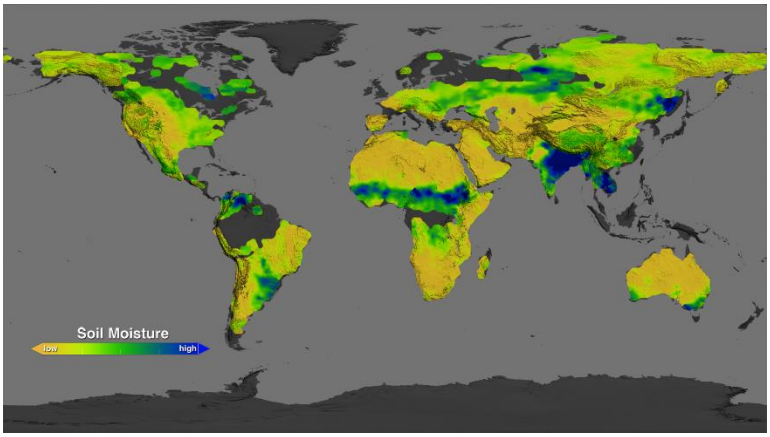

Figure 4-4: Soil Moisture conditions in August 2013. The data was retrieved from Aquarius. Dry areas are represented with yellow and wet areas with green

The 8th of June, 2015, the Aquarius mission ended suddenly. The onboard power of the spacecraft was lost for the attitude control system resulting in a cessation of data flow. The primary objective of the satellite mission was achieved by collecting observations and reporting high quality measurements for 3 years and 9 months with an unprecedented global resolution and accuracy.

5 DATASET AND METHODS

This section covers the data sets used and methodology followed to retrieve the variables that are analysed in the next chapter. Additionally, it includes a description of the target study areas.

5.1 Dataset

5.1.1 Aquarius/SAC-D data

This project covers 3 years of Aquarius Level 2 data satellite observations (September 2011 to August 2014). The data used are: the brightness temperatures (Tb_H, Tb_V), the radar backscatter co-pol (σ_{HH}, σ_{VV}), the radar backscatter crooss-pol ($\sigma_{HV} = \sigma_{VH}$) and the soil moisture product (SM_{SCA}), obtained with the Single Channel Algorithm.

The single channel algorithm (SCA) was implemented using the Aquarius observations to estimate surface soil moisture. The soil moisture retreival algorithm development focused on using only the radiometer data because of the extensive heritage of passive microwave retrieval of soil moisture. Ancillary data inputs required for using the SCA are vegetation water content, land surface temperature, and several soil and vegetation parameters based on land cover classes. The products are routinely available through the National Aeronautics and Space Administration data archive at the National Snow and Ice Data Center.

Measurements are considered exclusively from morning overpasses (6 A.M.) as vegetation and near-surface soil are present in thermal equilibrium.

5.1.2 Modern-Era Retrospective Analysis for Research and Applications (MERRA) dataset

MERRA is a reanalysis of historical weather data for the satellite era (from 1979 to the present). More precisely,

it consists on improving the hydrologic cycle analysis represented in earlier generations.

In order to obtain the parametrization of the vertical and horizontal emissivity, as described in Methods (p. 38), this study uses MERRA soil moisture information (SFMC) at 2 cm of depth, the soil temperature at 0.0988 m (TSOIL1) and 0.3859 m deep (TSOIL3).

5.1.3 MODIS IGBP Land Cover

The International Geosphere-Biosphere Programme Land Cover dataset is used in this study to classify the dominant land cover of each Aquarius/SAC-D footprint.

The 2005 MODIS MCD12Q1 IGBP product has a spatial resolution of 500 m and distinguishes 17 different land cover categories: evergreen needleleaf forests, evergreen broadleaf forests, deciduous broadleaf forests, mixed forests, closed shrublands, open shrublands, woody savannas, savannas, grasslands, permanent wetlands, cropland, urban and built-up, cropland/natural vegetation mosaics, snow and ice, barren and water bodies. Eight of these classes are found in the region of Australia.

The data can be downloaded for free at the Land Processed Distributed Active Archive Center (http://www.lpdaac.usgs.gov/).

For this Thesis, the IGBP classification is used to categorize each pixel in order to analyze homogenous data.

5.1.4 Australian Government Bureau of Meteorology Rainfall data

Since the mid-1800s, weather observations have been recorded in the Australian Data Archive of Meteorology. The products are now freely distributed by the Australian Government Bureau of Meteorology (http://www.bom.gov.au/climate/data/).

In this study, the data is used to investigate the effects of the rainfall in the behaviour of the different variables.

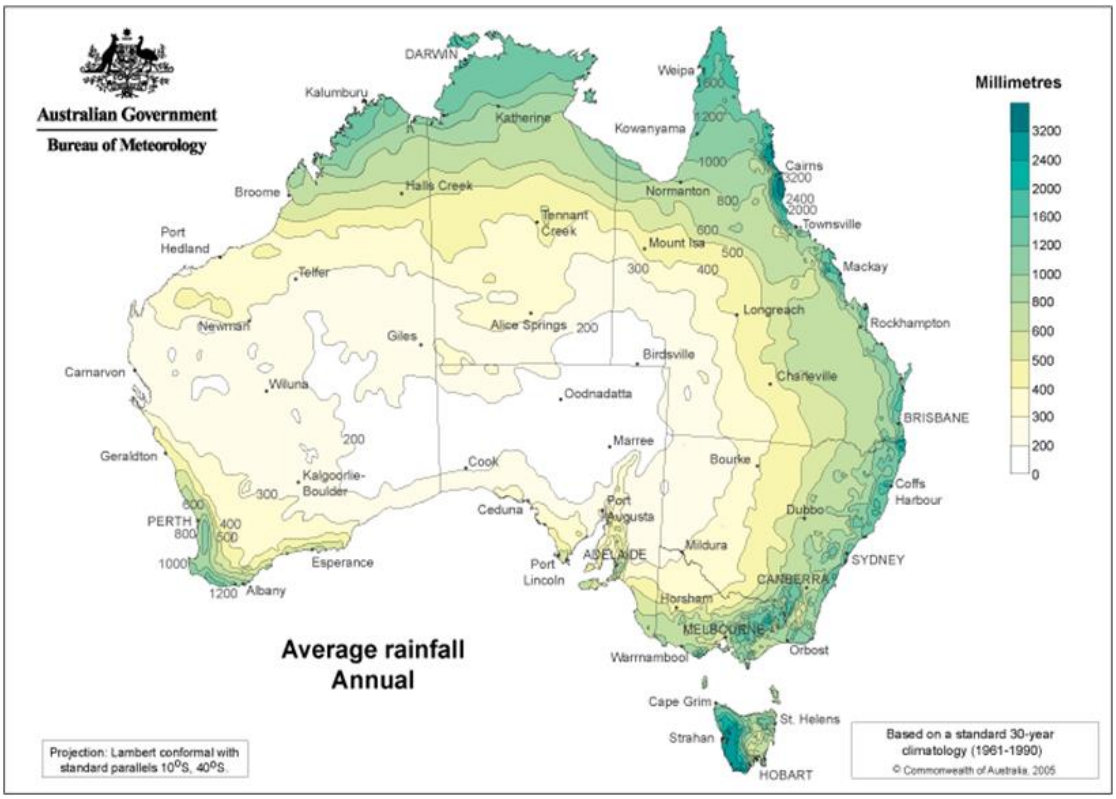

Figure 5-1: Representation of the annual average rainfall in the different regions of Australia. Based on 30-years climatology (1961-1990)

Figure 5-2 shows the average amount of water which evaporates from an open pan annually. Areas in central Australia are very dry, and therefore have a high rate of evaporation. In contrast, coastal areas tend to have a lower evaporation rate as a result of their proximity to a large water source. Areas with low rainfall and low humidity tend to have a high evaporation rate, while areas with high rainfall and high humidity tend to have a low evaporation rate.

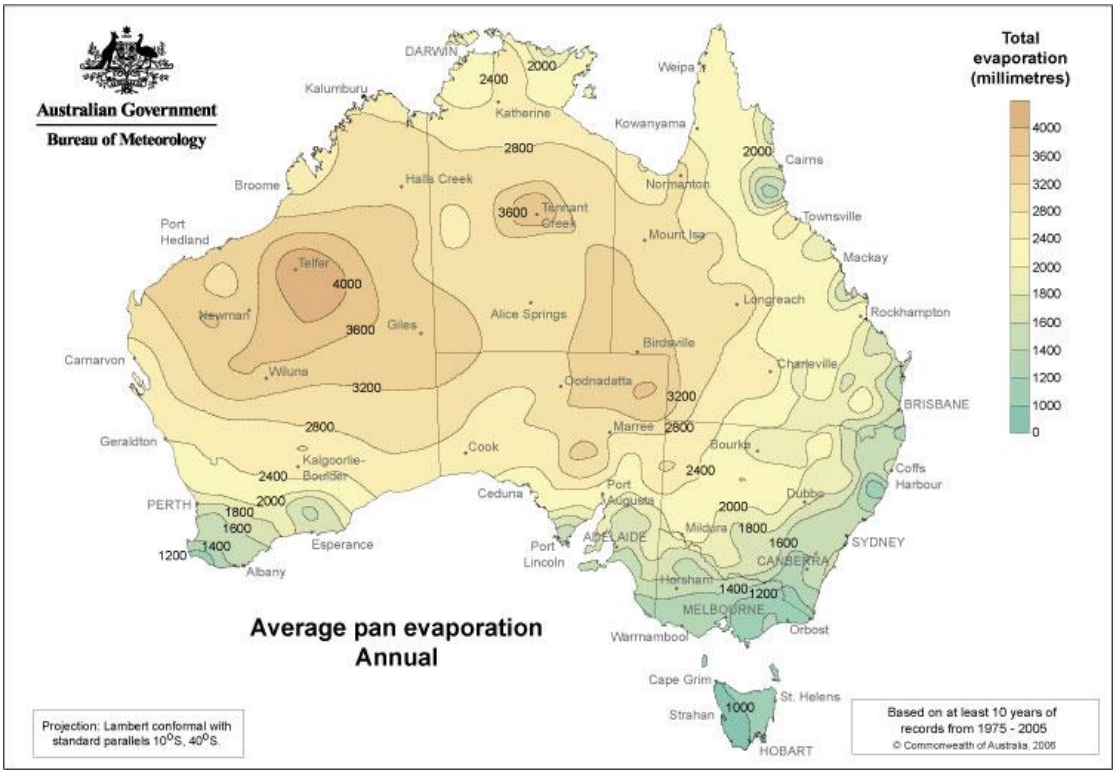

Figure 5-2: Average of the annual pan evaporation, based on the records from 1975-2005

5.1.5 National Vegetation Information System (NVIS)

NVIS is a data system of the Department of the Environment and Energy of the Australian Government. It provides information about the vegetation types in the different Australian regions. It was created for developing sustainable long-term solutions for Australian landscapes.

More information can be found in the following link: http://www.environment.gov.au/.

The NVIS is used for characterizing the vegetation of the 16 target ares.

5.2 Methods

5.2.1 Radar Variables

5.2.1.1 Radar Vegetation Index (RVI)

The RVI characterizes the amount of vegetation cover and it varies from 0 to 1. It is an indicative of the magnitude of scattering by vegetation [15]. It has the lowest values for smooth bare surface [$\sigma_{HV} \ll (\sigma_{VV}\ or\ \sigma_{HH})$] and it increases when the crop grows. It is defined by

$$RVI = \frac{8\sigma_{HV}}{\sigma_{HH}+\sigma_{VV}+2\sigma_{HV}} \qquad (26)$$

Where σ_{HV} is the radar cross-polarized backscatter, σ_{HH} is the radar backscatter in the horizontal polarization and σ_{VV} is the radar co-polarized vertical backscatter.

The RVI reaches it maximum (RVI=1) when there is full volume scattering by dense vegetation, since in these circumstances $\sigma_{VV} \approx 3 * \sigma_{HV}$ or $\sigma_{HH} \approx 3 * \sigma_{HV}$. The structural elements of vegetation canopies are the main drivers of this volume scattering. It has been shown that it has low sensibility to the environmental conditions effects [15].

The RVI is independent of greenness and it can be used in many applications; such as classifying regions, monitoring the crop growth and tracking lava flow. In this Thesis RVI is used to quantify the amount of vegetation.

5.2.1.2 Radar Roughness Index (RRI)

The RRI ratio is proposed as a measure of the surface roughness. The RRI ratio is written as a function of the observed backscatter coefficients (σ_{HH} and σ_{VV}) and the constant minimum bare soil backscatter values (${\sigma^s}_{HH}$ and ${\sigma^s}_{VV}$). It is defined by

$$RRI = \frac{\sigma_{HH} - {\sigma^s}_{HH}}{\sigma_{VV} - {\sigma^s}_{VV}} \qquad \textbf{(27)}$$

This algorithm was proposed in June 2005, as a solution to overcome the difficulty to account for the surface roughness effects over a footprint and the difficulty of decoupling roughness and vegetation effects form the radar signal [14]. The minimum bare soil backscatter values can be approximated by:

$${\sigma^s}_{HH}(clf) = 1.64 * clf^2 - 5.71 * clf + {\sigma^{s0}}_{HH} \qquad \textbf{(28)}$$

$${\sigma^s}_{VV}(clf) = 3.67 * clf^2 - 11.70 * clf + {\sigma^{s0}}_{VV} \qquad \textbf{(29)}$$

Where the clay fraction (clf) is a soil classification across global none frozen land regions. In this project, it was extracted from the SMOS database that uses ECOCLIMAP information.

This parameterization uses the backscatter values expected for dry soils: ${\sigma^{s0}}_{VV}$= -37.5 dB and ${\sigma^{s0}}_{HH}$= -29.1 dB. For low vegetation conditions it is mainly a function of the surface roughness and whereas for dense vegetation conditions it is more dependant of the vegetation cover [16].

5.2.1.3 Soil Moisture Index (SMI)

SMI is an estimation of the soil saturation in a thin layer of soil. It was initially proposed by Wagner [3] in his changed-detection approach to estimate soil moisture using radar information. After, McColl proposed another formulation for Aquarius observation [15].

The formula is an alteration from the original one, for it to be a function of σ_{VV} in linear units [15]. Moreover, it assumes that ${\sigma^{min}}_{VV}$ is an approximation to the value for a totally dry soil and that ${\sigma^{max}}_{VV}$ is an estimation of a fully saturated soil.

$$SMI(\sigma_{VV}) = \frac{10log_{10}(\sigma_{VV}) - \sigma^{min}{}_{VV}}{\sigma^{max}{}_{VV} - \sigma^{min}{}_{VV}} \qquad \textbf{(30)}$$

5.2.2 Radiometer Variables

5.2.2.1 Emessivities

Wigneron, introduced in the year 2001, an effective parametrization of the emissivity for rough surface characteristics (surface roughness and surface soil moisture).

In the model, the soil emissivity e_P is written as a function of the measured brightness temperature T_{B_P}, the effective soil temperature ${T_S}^E$, and the sky radiometric temperature ${T_B}^{SKY}$ [17].

$$e_P = \left(T_{B_P} - {T_B}^{SKY}\right)/({T_S}^E - {T_B}^{SKY}) \qquad \textbf{(31)}$$

For this study, a simplification of the formula is proposed. The term ${T_B}^{SKY}$ is eliminated because it has a low value (${T_B}^{SKY} \sim 4\ K$) and it almost does not affect the result of the emissivity. The resulting equation is

$$e_P = T_{B_P}/{T_S}^E \qquad \textbf{(32)}$$

Where ${T_S}^E$ is a parameterization of the effective soil temperature and depends on the deep soil temperature $T_{S\infty}$, the surface temperature $T_{S\,SURF}$ and a parameter that depends mainly on frequency and soil moisture C.

$${T_S}^E = T_{S\infty} + (T_{S\,SURF} - T_{S\infty})C \qquad \textbf{(33)}$$

C increases when there is an increment of the soil moisture content. Consequently, for high values of C, the effective soil temperature ${T_S}^E$ becomes closer to $T_{S\,SURF}$. C is given by

$$C = (w_s/w_0)^b \qquad \textbf{(34)}$$

Where w_s is equal to SFMC (5.1.2 Modern-Era Retrospective Analysis for Research and Applications (MERRA) dataset that is the 2 cm Surface Soil Moisture MERRA daily product. w_0 and b are semi-empirical parameters that can be extracted from TABLE II. The formulation used to simplify ${T_S}^E$ is similar to the one depeveloped by Choudhury [13]. The following calibrated values were deducted from the resulting data of the Avignon experiment [17].

TABLE II
CALIBRATION AND EVALUATION OF THE SIMPLIFIED MODEL OF T_S^E

$T_{S\,SURF}$	T_∞*	w_0	B	rms error (K)	bias (K)	R^2
T_{IRT} (thermal infrared measurement)	50 cm	0.418	0.498	2.71	-0.68	0.54
0.5 cm	50 cm	1.052	0.3157	1.88	0.04	0.69
1 cm	50 cm	1.079	0.277	1.62	0.11	0.77
2 cm	50 cm	0.794	0.258	1.38	0.13	0.84
4 cm	50 cm	0.377	0.262	1.37	0.1	0.84
5cm	50 cm	0.273	0.266	1.45	0.07	0.82

– as T_∞ at 50 cm was not available over the bare field plots, T_∞ was obtained from measurements over a wheat field adjacent to the bare fields.

Figure 5-3: Parametrization of the emissivity variables

To be aligned to w_s depth, Soil surface temperature ($T_{S\,SURF}$) correspond to temperatures at 2 cm. Consequently, w_0 equals to 0.794 and $b = B$ equals to 0.258. Theoretically, $T_{S\infty}$ is the deep soil temperature at 50 cm approximately.

$T_{S\,SURF}$ and $T_{S\infty}$ correspond to MERRA Soil temperature products at 0.0988m and 0.3859m respectively.

5.2.3 Target study areas

Australia is a vast and diverse country. Being the sixth largest country in the world, there is a significant vegetation and climate variety. According to the Australian Boreau of Meteorology, there are 6 major groups in the climate classification. These classes are retrieved from temperature/humidity, vegetation and rainfall data. The following images (Figure 5-6, Figure 5-5) show the different climate classes and sub-classes that are used for this chapter.

The weather is moderate in most of the areas of the country throughout the course of the year. However, it is warmer in the norther regions and it can get cold during the winters of the southern states.

Figure 5-4: Australia is a federation of 6 states and 10 federate territories. This figure shows the different

States: Western Australia (WA), Queensland (QLD), New South Wales (NSW), Victoria (VIC), South Australia (SA), Tasmania (TAS) and the Northen Territory (NT).

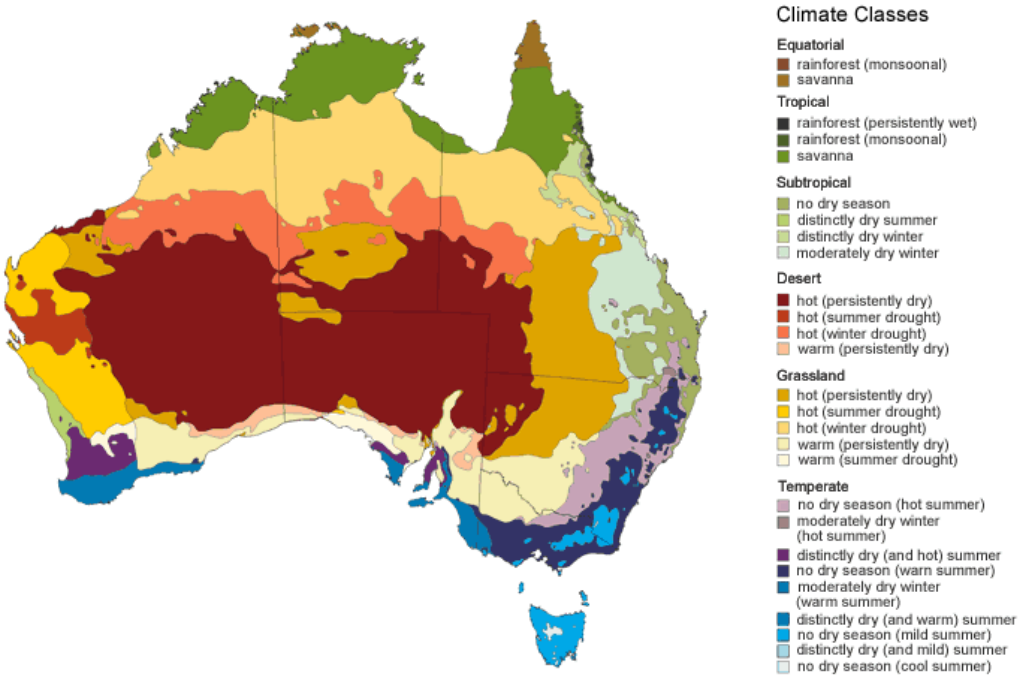

Figure 5-5: Climate sub-classes of Australia

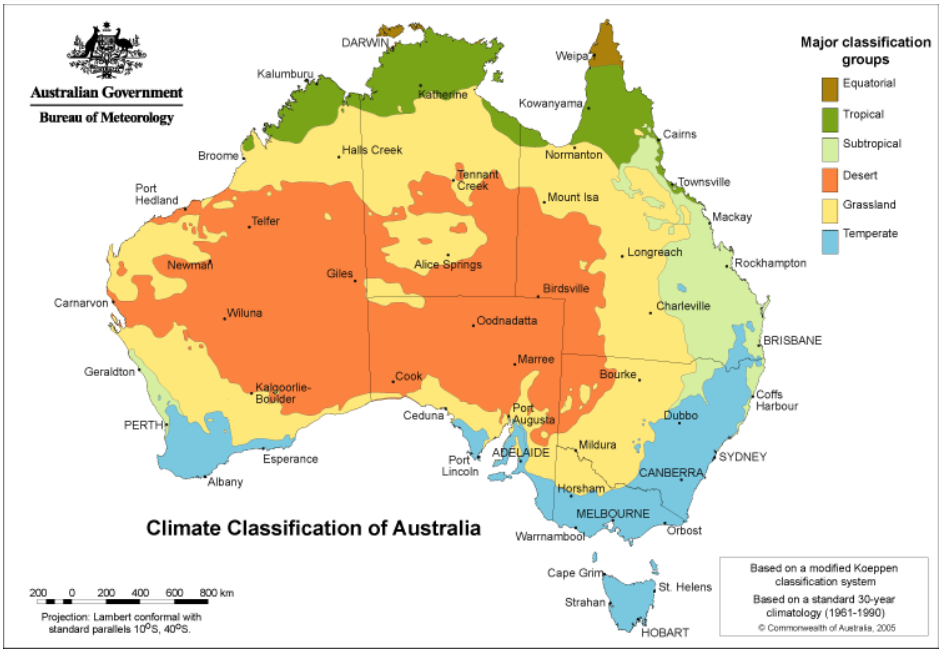

Figure 5-6: Climate Classes of Australia

In the region of Australia there are 8 IGBP classes (p. 35) that correspond to the vegetation and terrain differences.

This study is focused in 16 pixels that correspond to these 8 different IGBP classes. More precisely, 2 pixels per each class were selected so as to cover all possible climate and vegetation variability.

Name of the study area	Longitude Coordinate	Latitude Coordinate	IGBP
Terraleah TAS	146.4962º	-42.2972º	Evergreen Broadleaf forest
Talmalmo NSW	147.5529º	-35.9243º	Closed Shrublands
Tanami WA	128.8201º	-20.1º	Open Shrublands
Ingomar SA	134.8934º	-29.3961º	Woody Savannas
Nemarluk NT	130.4232º	-14.7934º	Savannas
Tablelands NT	136.2302º	-19.4144º	Grasslands
Kuender WA	118.5318º	-32.9043º	Cropland
Lake Eyre SA	137.9688º	-27.9051º	Barren
Ngaanyatjarra-Giles WA	127.4724º	-26.1123º	Open Shrublands
Lindsay VIC	141.1550º	-37.5830º	Cropland
Georgetown QLD	143.5543º	-18.1183º	Savannas
Myrtle Park NSW	145.4331º	-35.5658º	Grasslands
Bullfinch WA	119.0302º	-30.9359º	Closed Shrublands
Elgin QLD	146.8270º	-22.1517º	Woody Savannas
Kalamurina SA	137.4111º	-27.9452º	Barren
Bronte Park TAS	146.4052º	-42.1955º	Evergreen Broadleaf Forests

Table 5-1: Location of the 16 target areas

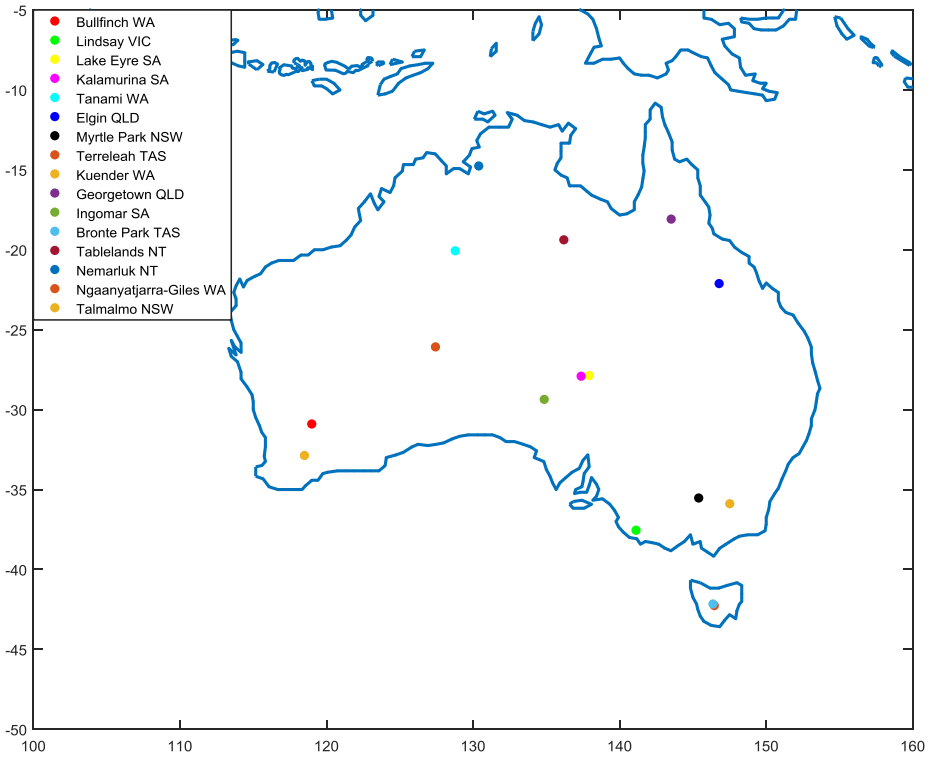

Figure 5-7: Map with the location of the 16 target areas.

5.2.3.1 Terreleah TAS

Located in the center of Tasmania, the pixel area includes: Lake Echo, Bradys Lake, Lake King William, Lake Gordon, Great Lake and Arthurs Lake. Although there are some lakes that may interfere the signal, most of the pixel is vast vegetation. There are many tall trees. The area is noted for many hydro-electric dams, canals and giant steel pipeways.

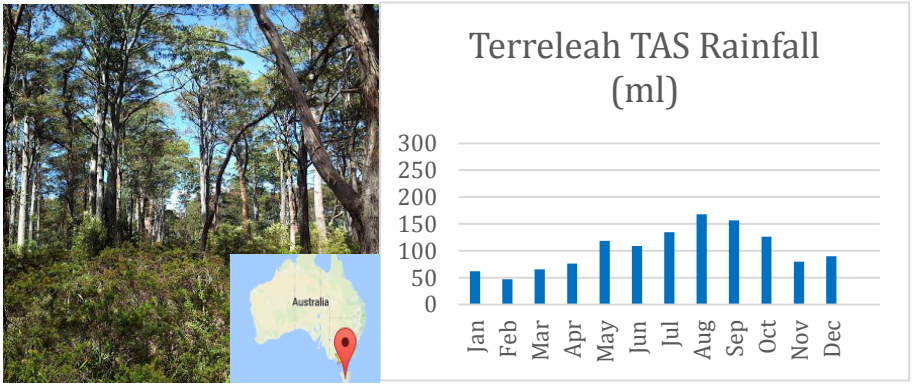

Figure 5-8: Terraleah TAS location and rainfall data

5.2.3.2 Talmalmo NSW

Situated in the frontier between Victoria and New South Wales, Talmalmo contains mountains from different state forest and national parks such as the Wabba Wilderness Park. Additionally, Talmalmo embodies the Murray River and the city of Albury. Albury has an urban population of 45.627 people. It has a warm, temperate climate.

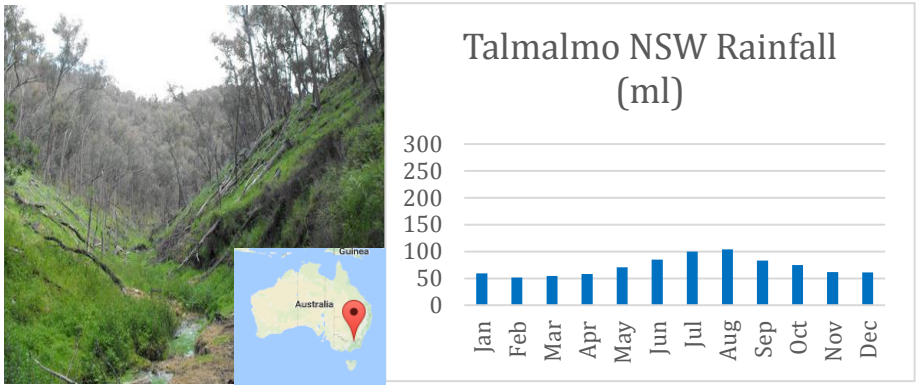

Figure 5-9: Talmalmo NSW location and rainfall data

5.2.3.3 Tanami WA

In between Western Australia State and Northern Territory, the Tanami Desert is found. The Tanami Desert is the third largest desert in Australia. It has a rocky terrain with small hills. The average annual rainfall is over 200mm. However, due to the high temperatures the evaporation occurs fast throughout most of the year. There can be flooded areas during the wet season (October-March). There are mostly sandy plains, sometimes covered with grass, low acacias and other small trees.

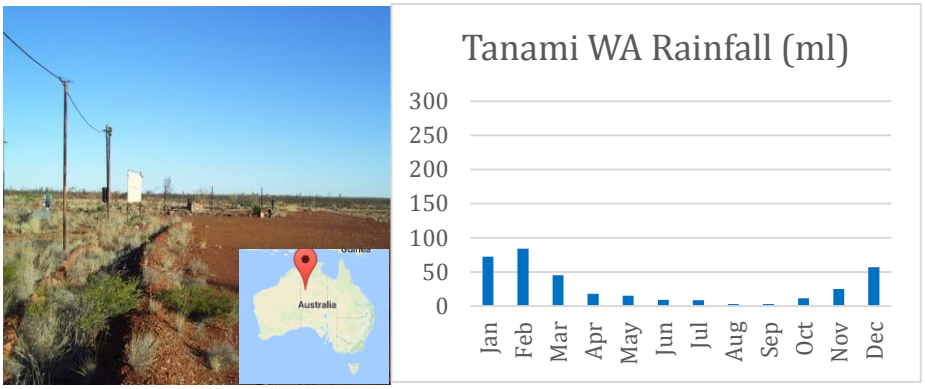

Figure 5-10: Tanami WA location and rainfall data

5.2.3.4 Ingomar SA

Ingomar is located in the state of South Australia, in a very dry area of the desert. It experiences far below average rainfall and humidity levels than the rest of Australia. It is dominated by shrubland and some grassland.

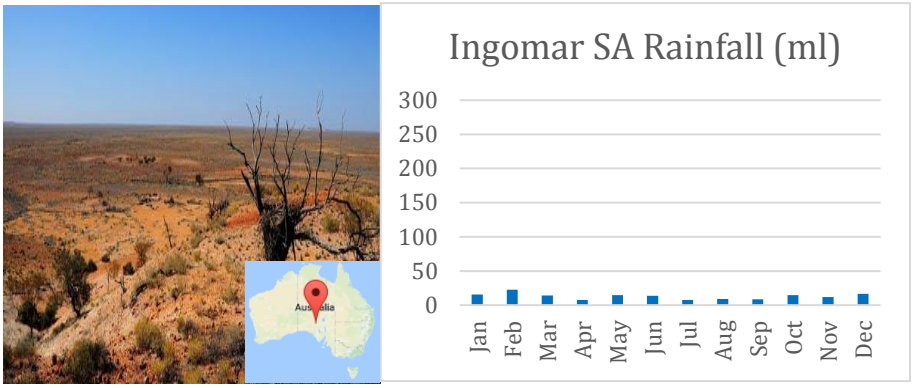

Figure 5-11: Ingomar SA location and rainfall data

5.2.3.5 Namarluk NT

Low vegetation predominates in this zone, located in Northern Territory. It has a tropical climate and experiences very high daylight temperatures. The wet season goes from October until April and it rains more than 900 mm. In contrast, during the dry season, from May until September, it rains less than 100 mm. The region contains Fizmaurize River.

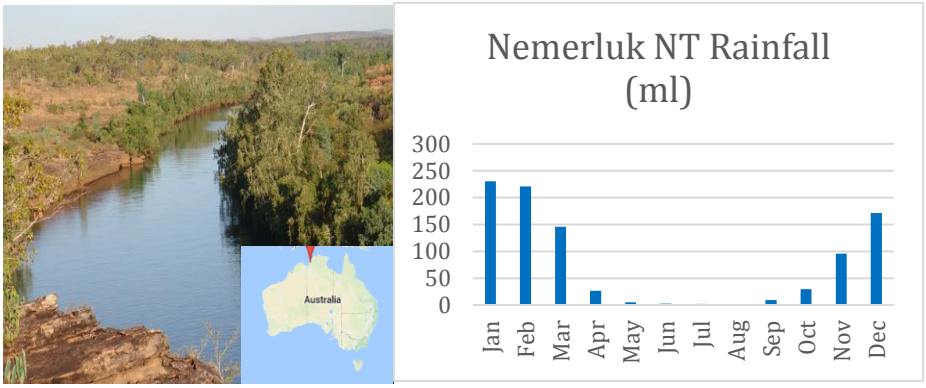

Figure 5-12: Nemarluk NT location and rainfall data

5.2.3.6 Tablelands NT

It is located in Northern Territory. The rainfall is low in this area and temperatures can vary from approximately 5 ºC to 35 ºC. The temperature variations are due to the four different seasons that the region experiences. The dominant flora is semi-arid savanna so most of the pixel has low spare vegetation.

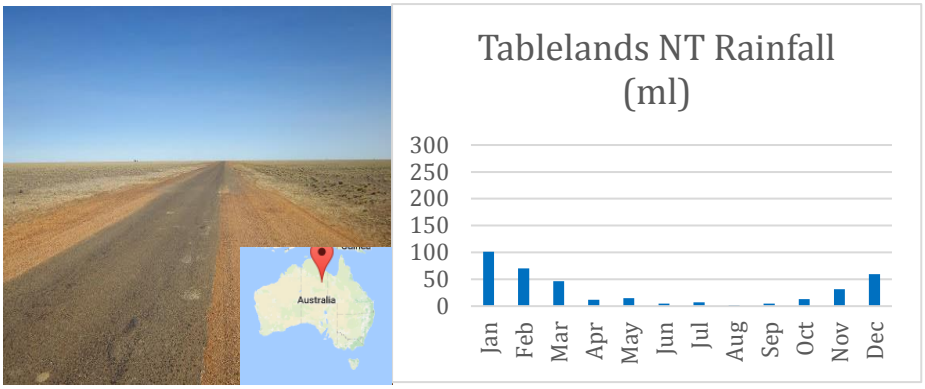

Figure 5-13: Tablelands NT location and rainfall data

5.2.3.7 Kuender WA

Situated in Western Australia, there are some little lakes in the area, a considerable portion of Lake Grace. Additionally, there are Natural Parks, including: Kuender Nature Reserve, Mordetta Nature Reserve and South Keunder Nature Reserve. However, it is mostly agricultural field. The average of the minimum and maximum temperatures through the year are 10 ºC and 24ºC, respectively. The mean of the annual rain is around the 340.

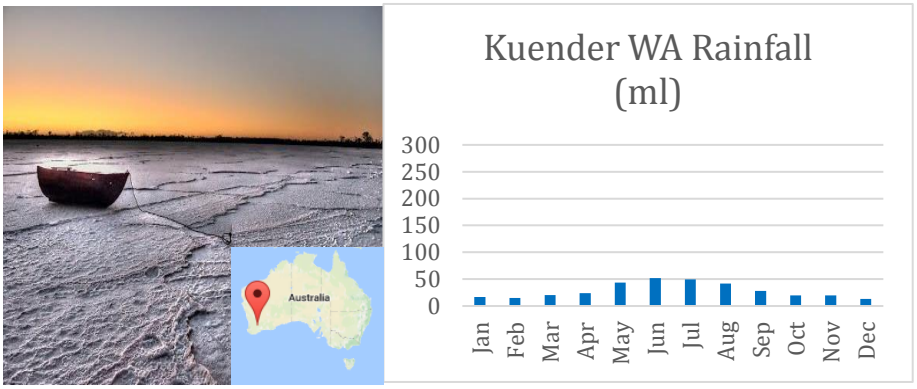

Figure 5-14: Kuender WA location and rainfall data

5.2.3.8 Lake Eyre SA

Surrounded by lakes, such as: Lake Koolkootinnie, Kalamurra Lake, Lake Mulapula, Lake Kittakittaooloo, Lake Warrandirinna and Lake Pantoowarinna, this pixel covers an area of South Australia. Nevertheless, the lakes appear to be quite dry. There is almost no vegetation and the ambit is mainly sand and some rock.

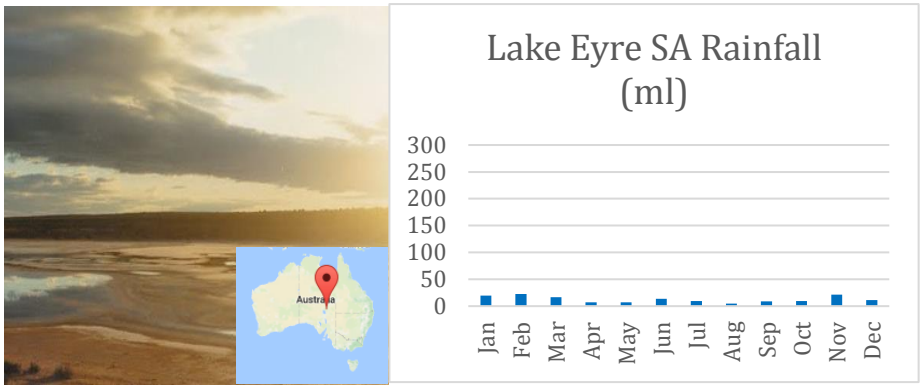

Figure 5-15: Lake Eyre SA location and rainfall data

5.2.3.9 Ngaanyatjarra-Giles WA

It is placed in Western Australia, low vegetation and low mountains prevail. The mean minimum temperatures in the site go from 7ºC to 22 ºC and the maximum temperatures go from 18ºC to 32ºC.

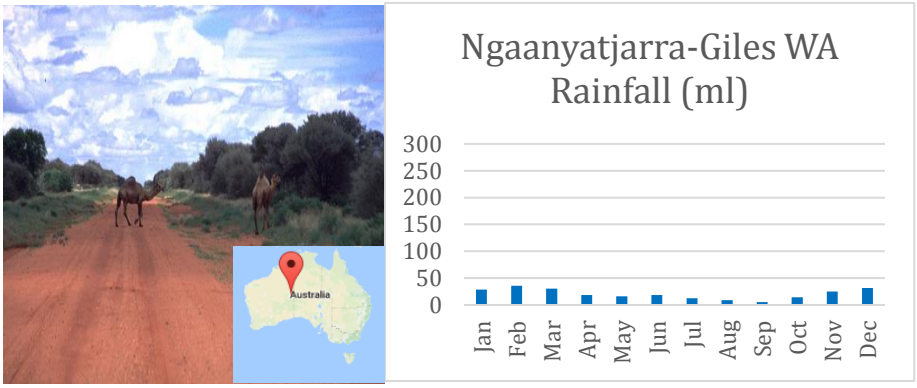

Figure 5-16: Ngaanyatjarra-Giles location and rainfall data

5.2.3.10 Lindsay VIC

In between Victoria and South Australia, the area includes several Forest Reserves and a town called Casterton. The town has a population of 1425, a mean minimum (average of the minimum temperature of each day during a year) and maximum temperature of 8.3ºC and 19.9ºC, and an annual rainfall of 640mm. Overall, it is a green pixel with different kinds of vegetation.

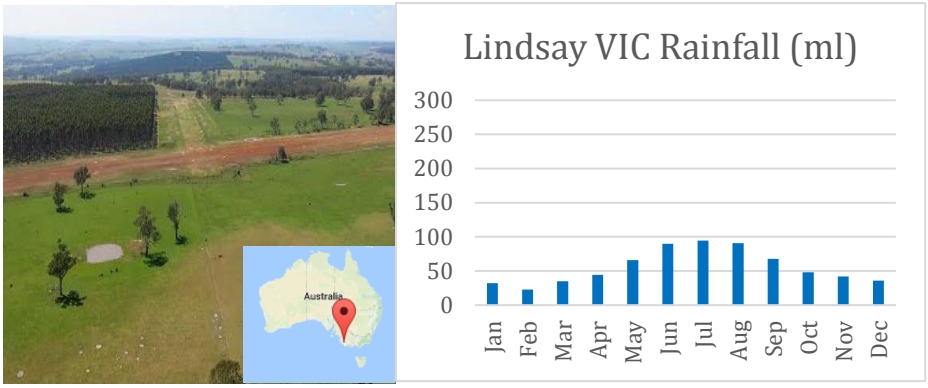

Figure 5-17: Lindsay VIC location and rainfall data

5.2.3.11 Georgetown QLD

It is located on the far north of Queensland. With a tropical climate, the target area includes mountains, rocks, lots of trees and a river called the Etheridge River. The economy of the region is based on cattle grazing and mining. The mean minimum temperature is 18ºC and the mean maximum temperature is 25ºC.

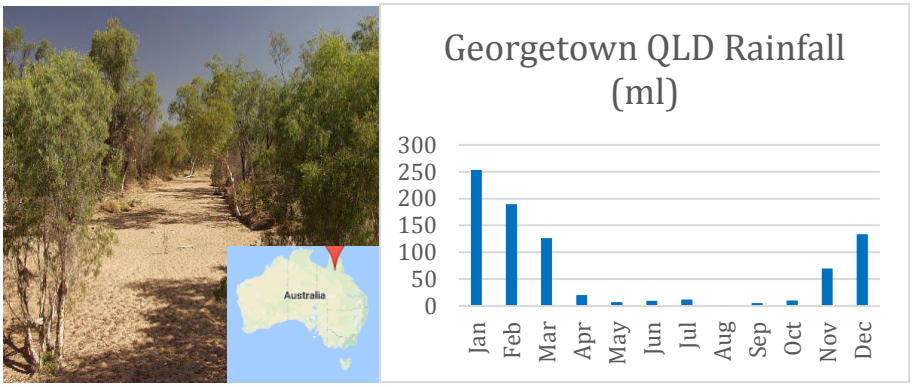

Figure 5-18: Georgetown QLD location and rainfall data

5.2.3.12 Myrtle Park NSW

Agricultural field zone with a portion of two national Parks called: Barmah National Park and Moira National Park. There are two towns, called Finley and Berrigan, in the area. Finley has 1921 inhabitants and Berrigan has a population of 922 Even though the center of the pixel is situated in NSW, the whole area contains as well Victoria State terrain. Temperatures go from 5ºC to 30ºC.

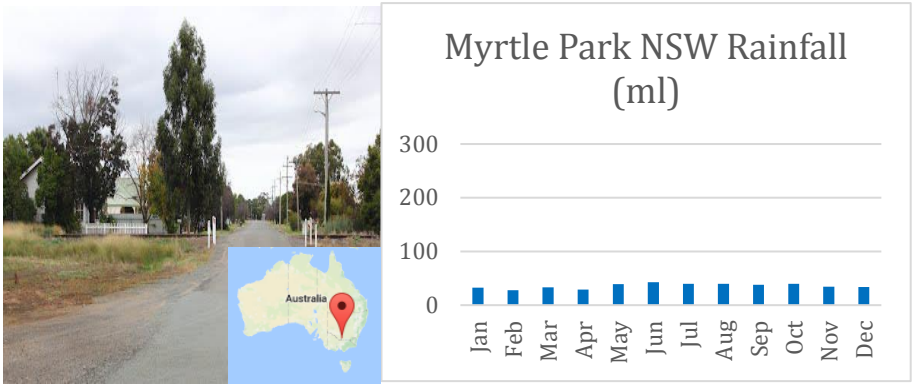

Figure 5-19: Myrtle Park location and rainfall data

5.2.3.13 Bullfinch WA

Half of the extent is mountain terrain and the other half agricultural field. There is a town in the area called Bullfinch that is known for gold mining. Another remarkable characteristic of the zone is that it includes Lake Deborah East.

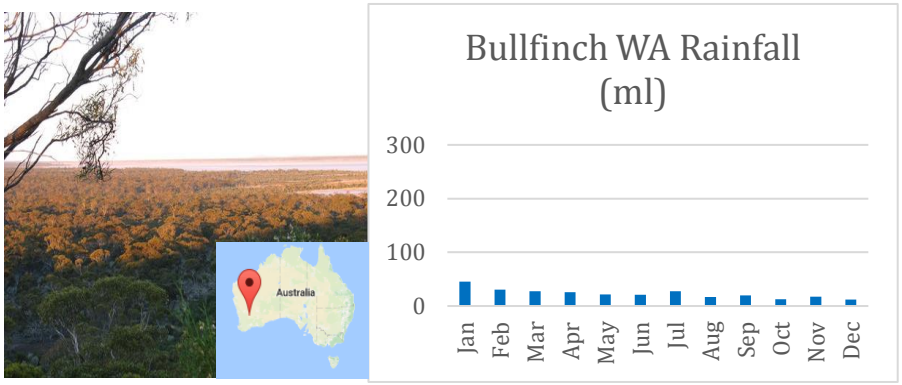

Figure 5-20: Bullfinch WA location and rainfall data

5.2.3.14 Elgin QLD

Constant vegetation in that region. Mostly not very dense although there is a small area full of trees. The rainy season in this subtropical climate area is between September and March.

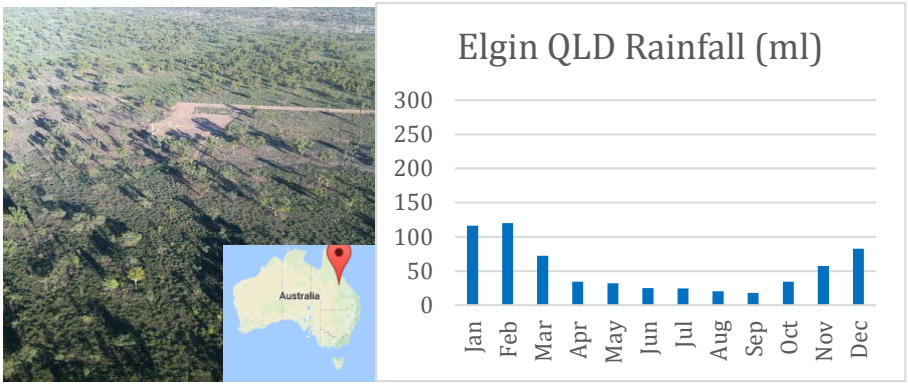

Figure 5-21: Elgin QLD location and rainfall data

5.2.3.15 Kalamurina SA

Almost half of the area consists on lakes and the rest is its national park. It is situated in the north of South Australia.

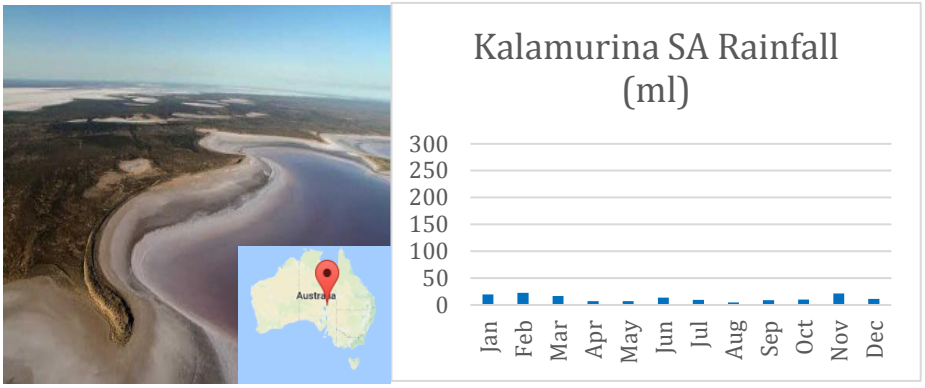

Figure 5-22: Kalamurina SA location and rainfall data

5.2.3.16 Bronte Park TAS

It is placed in Tasmania, surrounded by many different mountainous National Parks; such as: Walls of Jerusalem National Park and Cradle Mountain-Lake National Park. There are five main lakes in the region but they cover a small portion of the whole pixel.

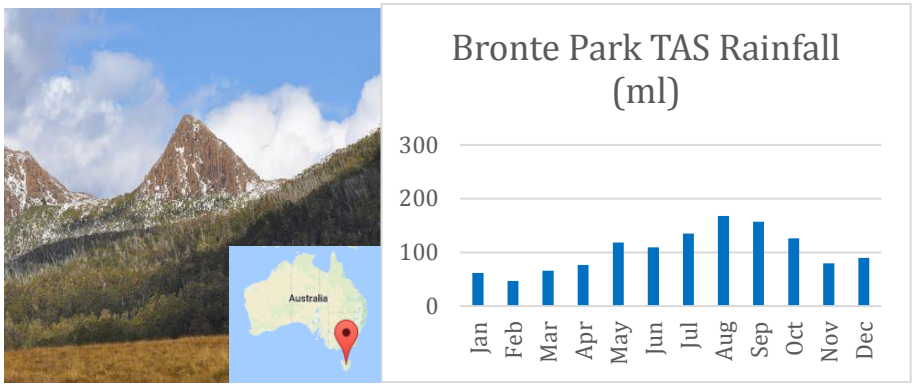

Figure 5-23: Bronte Park TAS location and rainfall data

6 RESULTS

6.1 Aquarius/SAC-D Passive observations

6.1.1 Emissivity (e_H, e_V)

The water in soils is the main factor dominating the Earth's emissivity at microwave frequencies. That is because of the difference of the dielectric constant of water (80) and that of dry soils (<5). That corresponds to emissivity values of 0.4 for water and 0.95 for a dry land [18].

Emissivity ranges from 0 to 1. the higher emissivity values in Australia are obtained for grasslands. More precisely, in the grassland territories characterized by being hot with a winter drought or warm with a presistently dry climate. Although the historic year average of rainfall in these areas is low-moderate, the deserted areas have lower rainfall but not higher emissivity than the rest of the country. There are some maximum values in the vertical polarization that exceed the maximum theoretical value of 1. This is probably due to inconsistencies with the modeled land surface temperatures used to calculate emissivity from brightness temperatures ($e_P = T_{B_P}/T_S^{\ E}$).

The lower emissivity is obtained for savannas, the hot grasslands and some specific areas within the desert. The annual rainfall average is high for the savanna and moderate or low for the rest. Nevertherless, the lower values correspond to areas that are constantly wet through the year. For instance, lakes as Lake Sylvester and Tarrabool Lake in Northern Territory State and Lake Torrens National Park, Lake Gairdner National Park, Lake Frome and Lake Eyre in South Australia have a significantly low emissivity.

Although the main dominating factor of the Earth's emissivity is the water in soils, its variation is also influenced by the vegetation cover, soil properties and surface roughness. The vegetation is the most significant of them because of its impact. In Australia, the extreme values of the emissivities are found in the grassland areas. Figure 6-5: e_H **average values of each pixel during the three years data** and Figure 6-6 show the temporal mean of emissivity for the three years of Aquarius observations, polarization H and V, their maximum values correlate

with the arid-regions and their minimum values are found in the temperate areas.

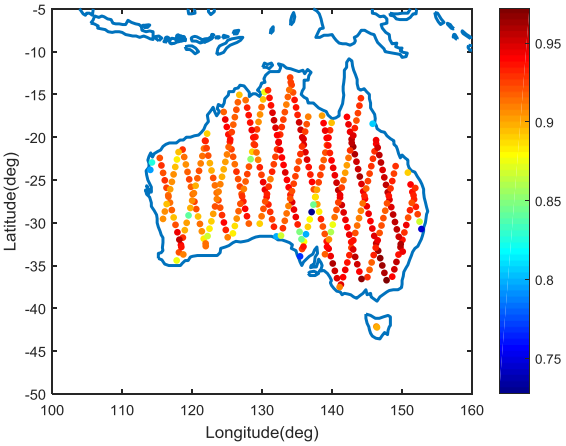

Figure 6-1: e_H maximum values of each pixel during the three years data

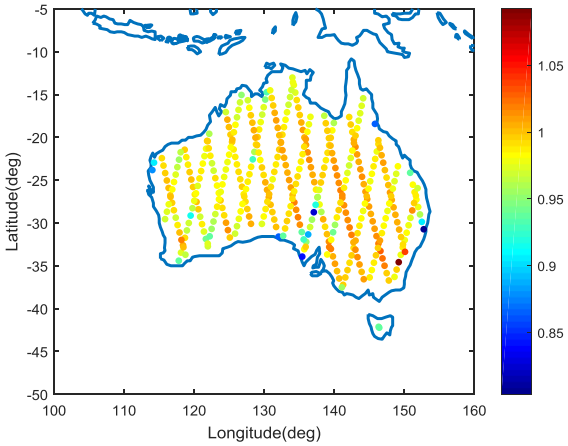

Figure 6-2: e_V maximum values of each pixel during the three years data

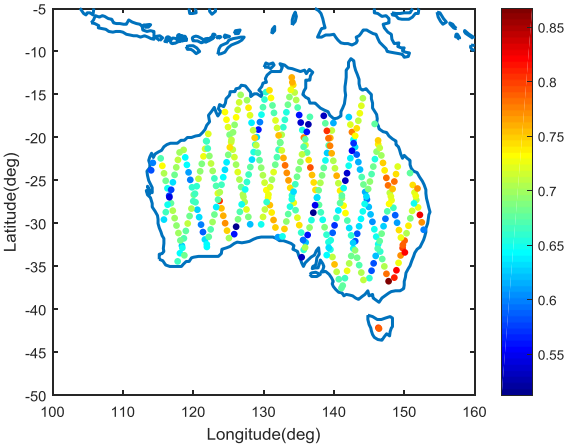

Figure 6-3: e_H minimum values of each pixel during the three years data

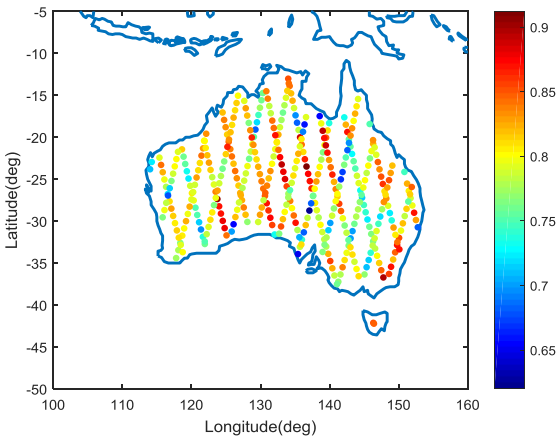

Figure 6-4: e_V minimum values of each pixel during the three years data

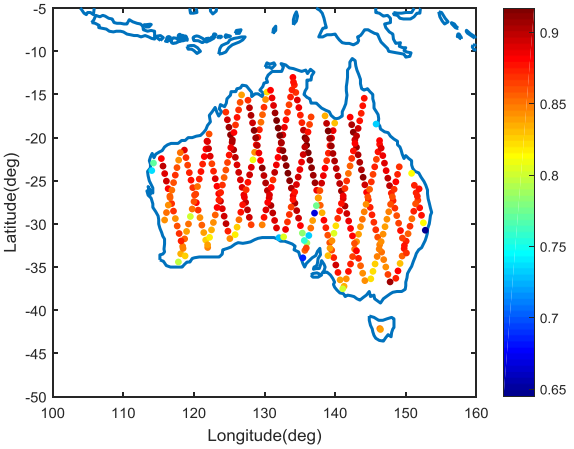

Figure 6-5: e_H average values of each pixel during the three years data

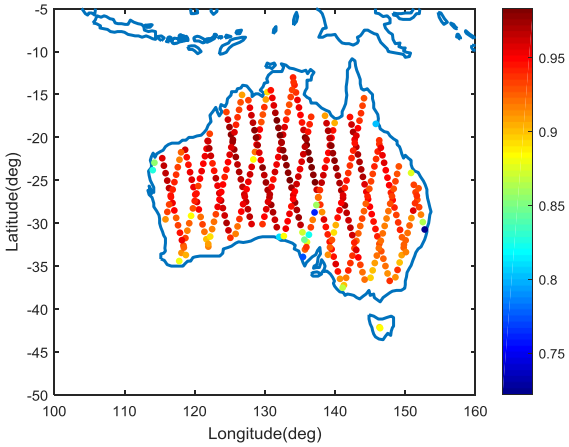

Figure 6-6: e_V average values of each pixel during the three years data

6.1.2 Soil Moisture (SM_{SCA})

As expected, SM_{SCA} correlates with the precipitation in the region of Australia (Figure 5-1). High values are found in the areas with subtropical and temperate climate, and low values relate to arid-regions. Nonetheless, subtropical regions, located in the north of the country, appear to have lower values than expected.

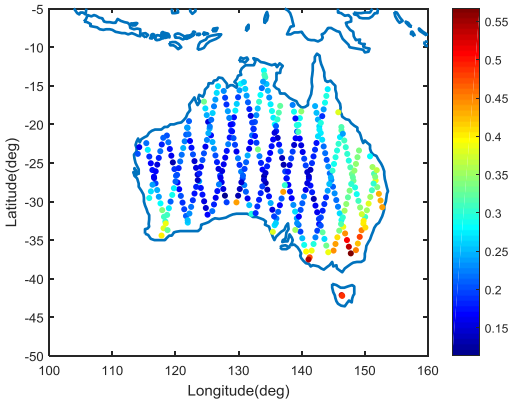

Figure 6-7: SM_{SCA} average during the 3 years of Aquarius/SAC-D data

6.2 Aquarius/SAC-D Passive observations

6.2.1 Radar backscatter (σ_{VV}, σ_{HH}, σ_{VH})

Co-polarized backscattering coefficients (σ_{VV} and σ_{HH}) are mainly associated with surface scattering while σ_{VH} backscattering is more related to the volume or multiple scattering [5]. The power of cross-polarized backscatters Figure 6-8 is lower than the other backscatter because the radar is sending a signal in one polarization and the antenna is receiving it in another. The depolarization is caused by the interaction of the signal with the vegetation (branches, leaves, stems…).

Figure 6-8, shows an Australian map of average observed HV cross-polarized backscatters, in logaritmic units. In the map it can be appreciated that the data is well correlated with Australian vegetation patterns. The only exceptions are the equatorial class, where there is no data, and some inland parts in the easters states (mostly in the New South Wales State), where the cross-polarized backscatter has a higher value than what would correctly represent the amount of vegetation. Other zones as the ones with tropical, subtropical and temperate classes are very well correlated with the identified vegetation density. For instance, the rainforests in the wet tropics and in Tasmania, have the highest values. Followed by the Eucalypt forests in the east coast, the Acacia forests and woodlands in Western Australia and the south of New South Wales. The casuarina forest in the south frontier between Western Australia and Northern Territory States, can be identified because of its value contrast with its surrounding desert areas. The different deserts are well characterized with low values.

Although, high co-polarized backscatter is mostly an effect of surface scattering, they can also be a result of volume scattering or double bounce interactions between vegetation and the surface. Consequently, high values indicate wet soil or well vegetated areas. A low value indicates that the zone is either dry or lightly vegetated [5]. In fig. 6-10 and 6-11, values are higher in the areas where soils are wet rather than dry, as in the equatorial, tropical and temperate climate areas. In dry regions as the desert and grassland, the values are lower. For all classes, the co-polarized backscatter is well correlated with the rainfall and soil moisture data. However, the arid areas have higher values than expected.

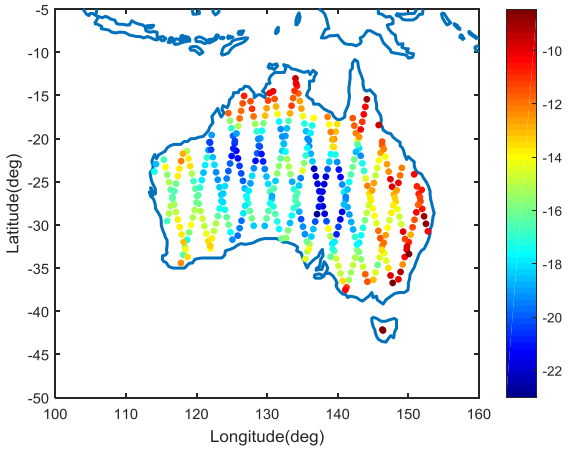

Figure 6-8: σ_{VH} average during the 3 years of

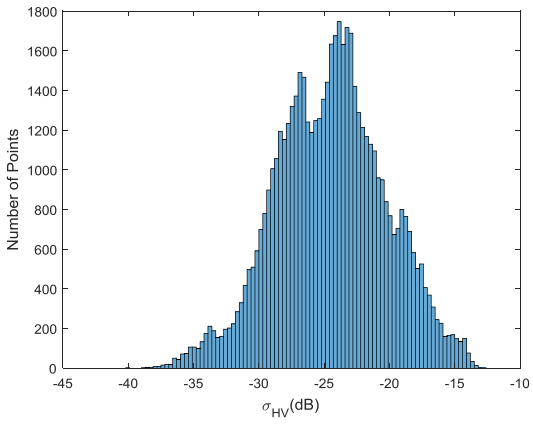

Figure 6-9: Histogram of 3 years Aquarius cross

Aquarius/SAC-D data

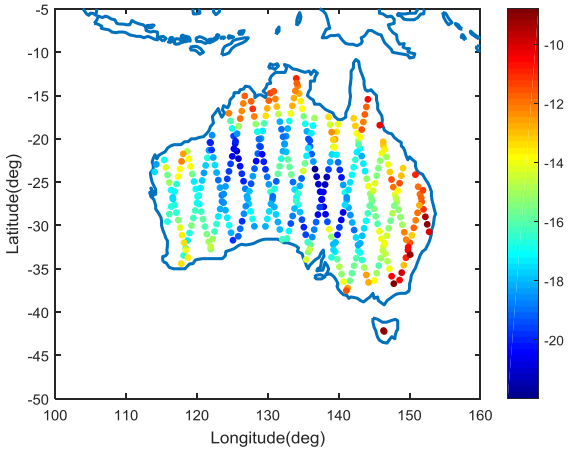

Figure 6-10: σ_{HH} average during the 3 years of Aquarius/SAC-D data

polarized radar backscatter, σ_{VH}, (in decibels)

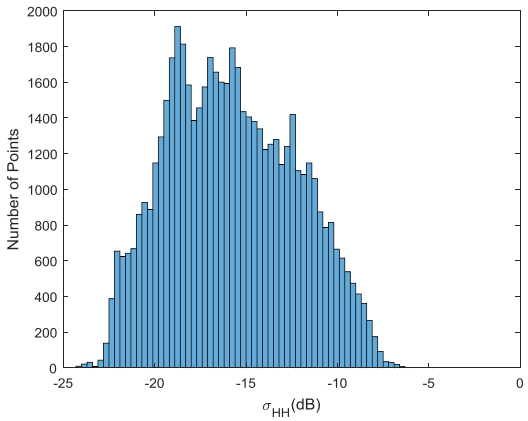

Figure 6-11: Histogram of 3 years of Aquarius co-polarized radar backscatter, σ_{HH}, (in decibels)

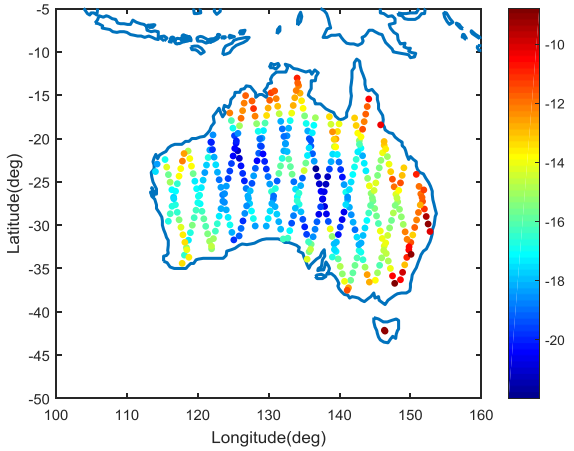

Figure 6-12: σ_{VV} average during the 3 years of Aquarius/SAC-D data

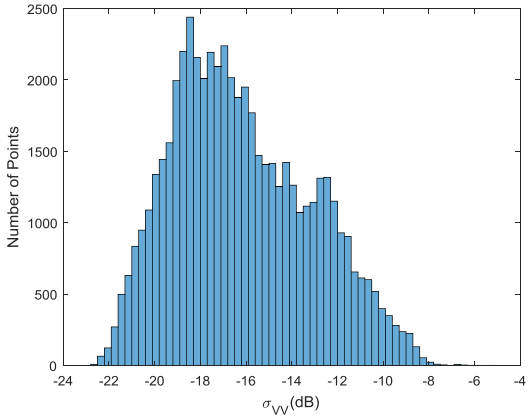

Figure 6-13: Histogram of 3 years of Aquarius co-polarized radar backscatter, σ_{VV}, (in decibels)

6.2.2 Radar Vegetation Index (RVI)

Although the overall view of the Radar Vegetation Index in the region of Australia generally matches with the known vegetation patterns from the National Vegetation Information System (NVIS) (p. 35), with some exceptions. This may be due to RVI being vulnerable to errors in the calibration offset term over lightly vegetation regions, leading to overestimation in dry regions [15].

When the RVI is analyzed for its different climate classes, it is found that in the equatorial climate class, there is no data. However, in temperate classes the RVI results are as expected. In some parts in the tropical, subtropical,

desert and grassland classes there are some unexpected beahavours. The best example is the Great Victoria Desert, which has an RVI close to 1. Although a small extent of the desert has acacia forests and woodlands, most of the region is covered by hummock grassland and a smaller percentage of acacia shrubands. Other zones with higher RVI than expected are in the Great Sandy Desert and the Little Sandy Desert. These zones have a medium to high RVI and its predominant vegetation is hummock grassland. On the other hand, in the tropical area, the maximum value in the region is approximately 0.65, which is underestimated and does not represent the high vegetation density.

Some areas that have expected RVI values are: the coast of Victoria and New South Wales, that is cataloged as an eucalypt oper forests region and, the south of New South Wales and the east-center of Western Australia, where the acacia open forests are. These areas have an RVI value close to 1 because of its dense vegetation. Moreover, the subtropical zone, situated in the northern part of Western Australia, Northern Territory and New South Wales has a high RVI that matches with the NVIS. The predominant vegetation in that class is the Eucalypt open woodlands and the Melaleuca forests and woodlands. The interior of the east coast in Victoria and New South Wales States includes many cities and it is cleared from vegetation except from the agricultural fields. The RVI measurements have higher values than expected, up to 0.65.

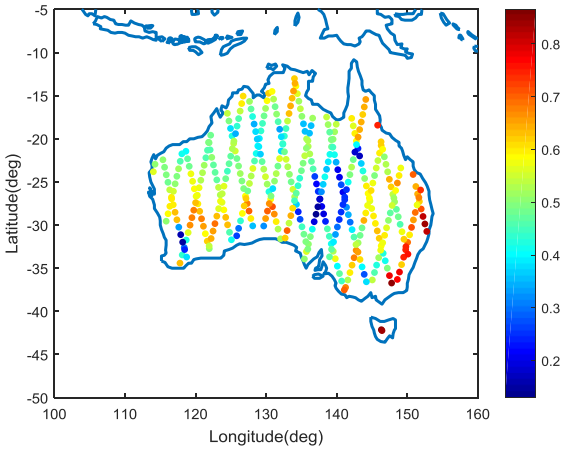

Figure 6-14: RVI average during the 3 years of Aquarius/SAC-D data

6.2.3 Radar Roughness Index (RRI)

Surface Roughness generally varies over long periods as seasons. Surface Roughness changes can be induced by disturbances, erosion and deposition events [16]. As stated in Section 3.2, when the surface is rough, the pulse can be scattered back in the same direction. Thus, the power of the received signal is higher. Figure 6-14, shows that the areas with higher roughness in Australia are those with tropical, subtropical and temperate climates.

In section 6.3.2, the analysis is based on the hypothesis that roughness in the region of Australia does not change significantly over a year period. Figure 6-16 shows the difference between the RRI average of two consecutive years.

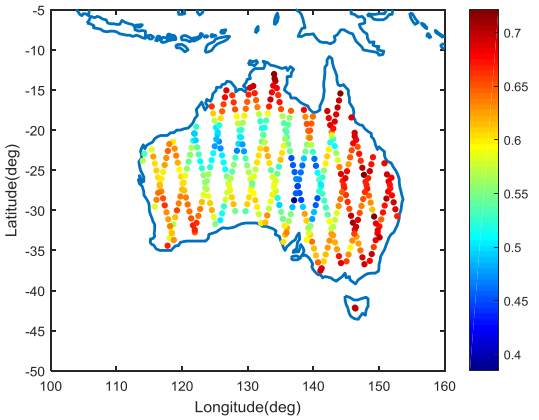

Figure 6-15: RRI average during the 3 years of Aquarius/SAC-D data

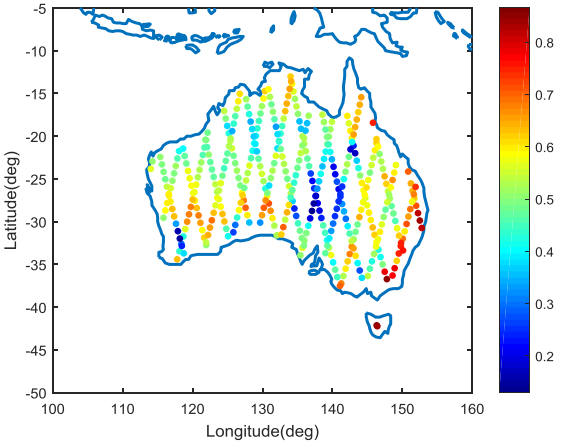

Figure 6-16: RRI difference between the averages of two years

6.2.4 Soil Moisture Index (SMI)

As expected, the lowest SMI values are found in the arid-areas of the country. On the other hand, the climate classes: tropical and grassland appear to have lower values than expected. It could be due to the fact that these zones experience high evaporation (p. 35). SMI is known to be sensitive to calibration errors over regions where the dynamic range of the backscatter coefficient is small, including deserts and forests [15]. For instance, the tropical climate area appears to have lower values than expected.

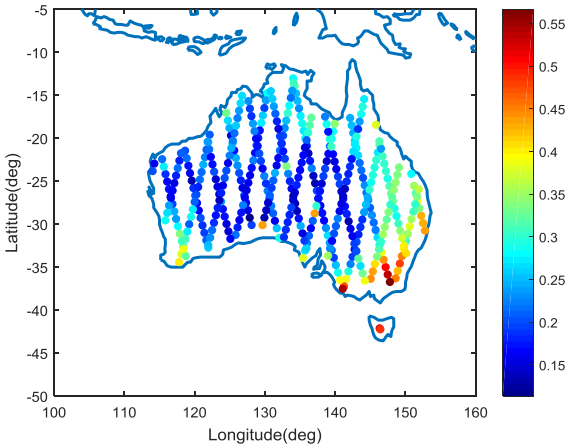

Figure 6-17: SMI average over the region of Australia

6.3 Active and Passive comparison

6.3.1 Joint distribution density

In order to combine active and passive microwave, radar observations ($\sigma_{VV}, \sigma_{HH}, \sigma_{VH}$ and RVI) are compared to both emisivities.

The theory states that for incidence angles lower than 50º, as it is the case of Aquarius, radar-radiometer covariations are mostly related to variations in the soil dielectric constant (SM changes) than to changes in vegetation or surface roughness conditions. The slope of the linear relation between the emissivity and the backscattes is positive for surfaces with a high dielectric constant (water) and negative for surfaces with a low dielectric constant (low soil moisture). This slope can change from negative to possitive if the soil moisture increases [5].

For the majority of the region of Australia, it is expected that when Soil Moisture (SM) increases, the emissivity decreases and the backscattering coefficients rise. However, in regions predominated by deserts, coastal areas and forests the opposite behaviour could be observed. In the Figure 6-18 it can be aprecciated that there is a negative slope between the active and the passive signal. However, in most of the graphics there are some points that describe an almost zero slope line. This slope is attributed to the arid regions.

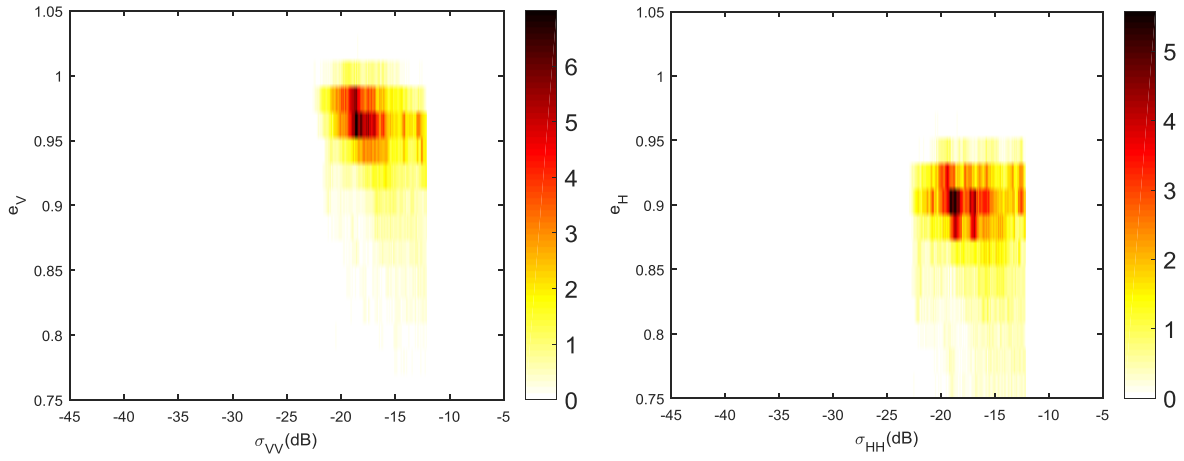

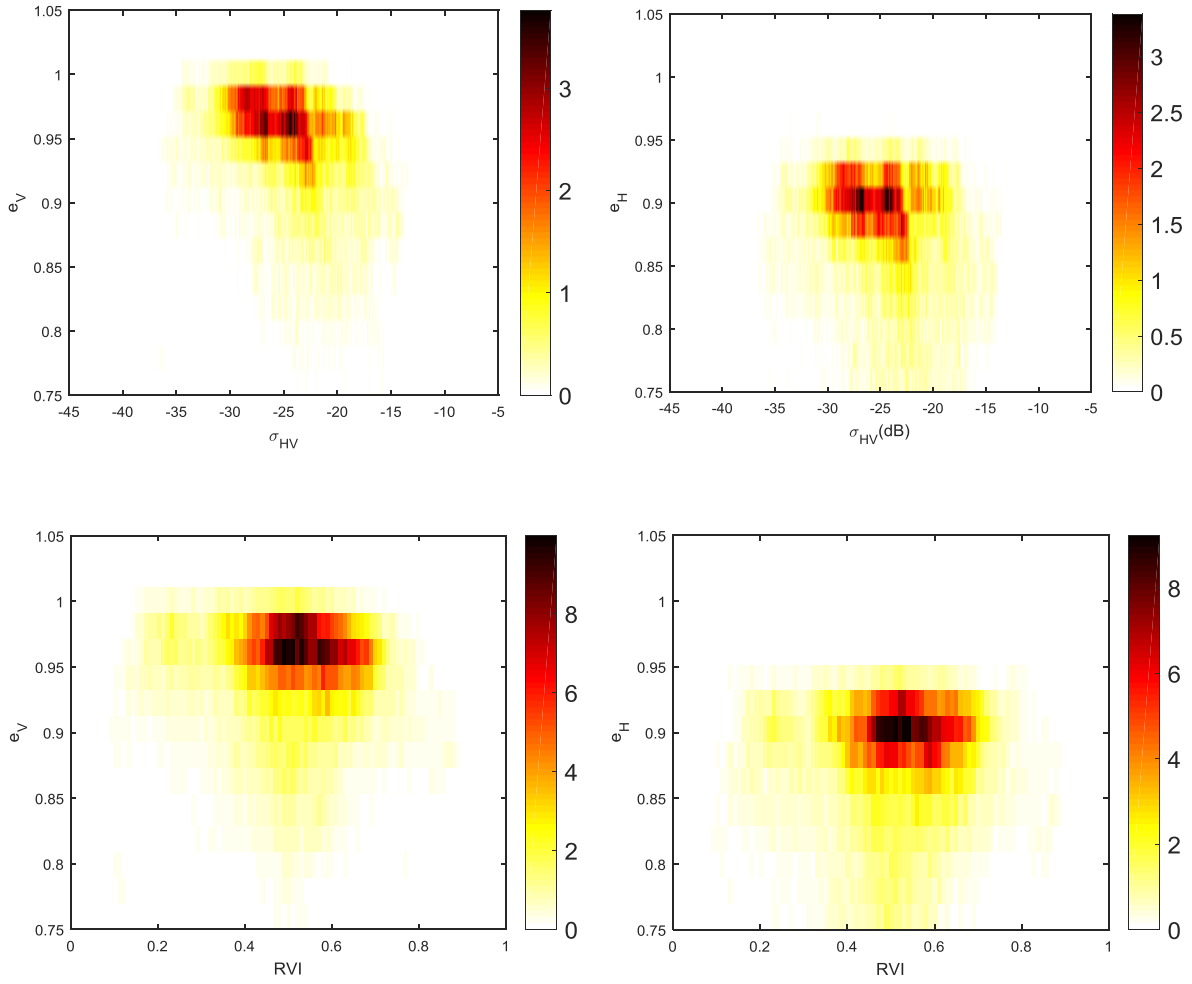

Figure 6-18: Relationship between the different emissivity and the backscatter or RVI in the region of Australia during the three years data

6.3.2 Max/Min

In this section, it is studied if the vegetation effects can be characterized in relation to the emissivity. To further remove the vegetation dynamics, it is necessary to quantify those using the available data. The RVI (p. 38) is the index used in this thesis for estimating the amount of vegetation in the region. More precisely, it is used to identify variations in the annual extreme values of the emissivity during high and low vegetation conditions, so that the vegetation effect on the emissivity can be understood. Commonly, it is expected to get lower emissivity in areas where the vegetation is dense and, higher emissivity for no vegetated regions. Basically, it is assumed that more vegetation has more water content above the soil.

The relationship between changes in emissivity and backscatter can help to conduct downscaling of passive microwave data through change detection algorithm. Thus, the vegetation effect could be removed from the emissivity, without the need for a radiative transfer model, or at least to constrain the model. Overall, inter-annual cycles within the vegetation could also be removed from the emissivity, to retrieve the soil component, and not a

compound influence from the vegetation and the soil.

Having demonstrated that surface roughness is relatively constant over time (p. 55), emissivity and backscatter variations are then mostly dominated by soil moisture and vegetation dynamics.

The studies realized in this section are included in Appendix 2. From the analysis performed, it was concluded that there was not a constant pattern behaviour between the extreme values of the emissivity and the RVI in the different land covers. The causes could be that the IGBP classes include pixels with different kinds of vegetation, that RVI is not a good index or that there is not a straight relation between the vegetation variations and the emissivity values.

6.3.3 Active and Passive temporal correlation

Australia is the sixth biggest country in the world and it has huge variations in its climate. Therefore, it is predictable that many anomalies alter the studies when the whole area is analysed. Furthermore, it is noticed that to better understand the behaviour of the variables, it will be necessary to conduct an individual study of the environment of the pixels (p. 38). 16 different areas are chosen for a more precise analysis.

Name of the study area	$\sigma_{HH} - e_H$	$\sigma_{VV} - e_V$	$\sigma_{HV} - e_H$	$\sigma_{HV} - e_V$
Bullfinch WA	0.921	0.867	0.827	0.806
Lindsay VIC	0.784	0.754	0.775	0.795
Lake Eyre SA	0.719	0.611	0.351	0.369
Kalamurina SA	0.0194	0.0136	0.564	0.532
Tanami WA	0.826	0.791	0.382	0.419
Elgin QLD	0.911	0.876	0.838	0.858
MyrtlePark NSW	0.644	0.777	0.597	0.62
Terraleah TAS	0.418	0.321	0.325	0.32
Kuender WA	0.449	0.573	0.61	0.613
Georgetown QLD	0.952	0.933	0.891	0.904
Ingomar SA	0.837	0.842	0.449	0.46
Bronte Park TAS	0.389	0.305	0.222	0.226

Tablelands NT	0.843	0.803	0.593	0.59
Nemarluk NT	0.963	0.957	0.905	0.912
Ngaanyatjarra-Giles WA	0.915	0.861	0.726	0.721
Talmalmo NSW	0.777	0.792	0.739	0.773
Average	0.7104625	0.6922875	0.612125	0.619875

Table 6-1: Correlation values between emissivity and backscatter

More densely-vegetated sites show a higher correlation between the emissivity and the backscatter (co-polar and cross-polar). The exceptions are the sites of Terreleah and Bronte Park, located in Tasmania. In fig. 6-19 it can be appreciated that in both graphics the data is very disperse for the antenna receives different emissivity values with the same power.

The areas with less vegetation, have a high correlation between the co-polarized backscatter and the emissivity. Nonetheless, their cross-polarized backscatter correlation with the emissivity is low. It could be due to the fact that the vegetation is detected with the HV polarization of the antenna.

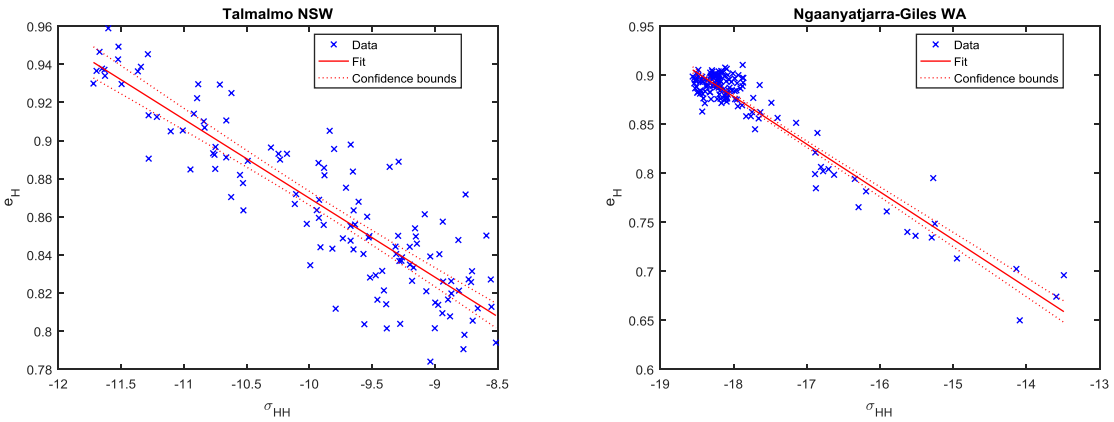

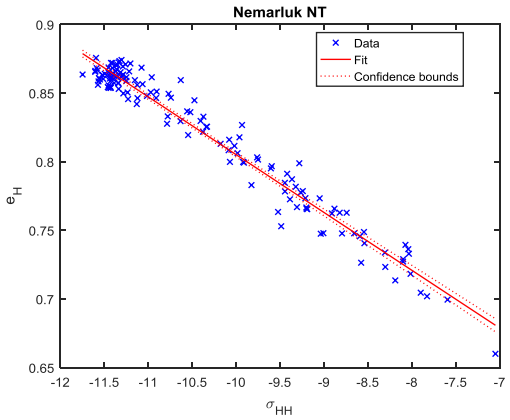
Nemarluk NT
Data
Fit
Confidence bounds
e_H
σ_{HH}

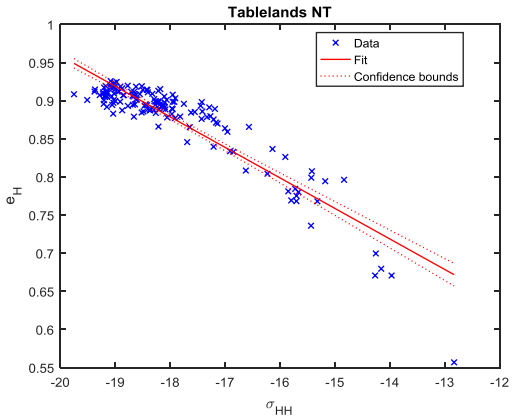
Tablelands NT
Data
Fit
Confidence bounds
e_H
σ_{HH}

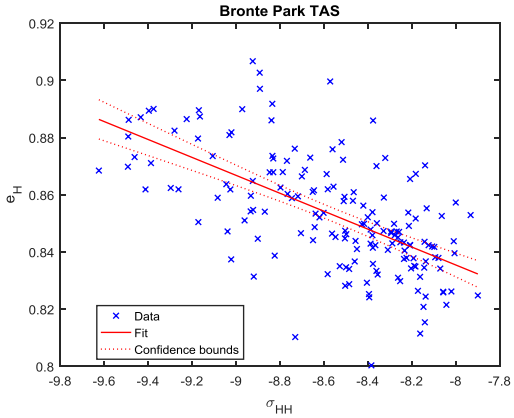
Bronte Park TAS
Data
Fit
Confidence bounds
e_H
σ_{HH}

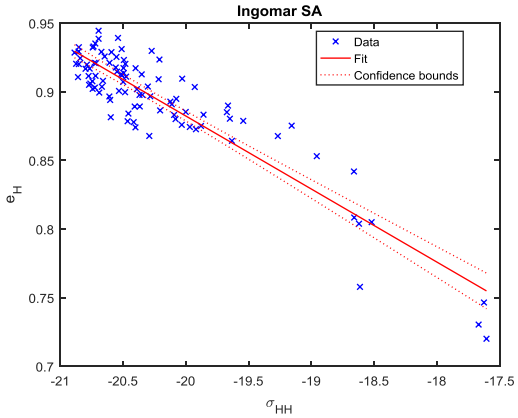
Ingomar SA
Data
Fit
Confidence bounds
e_H
σ_{HH}

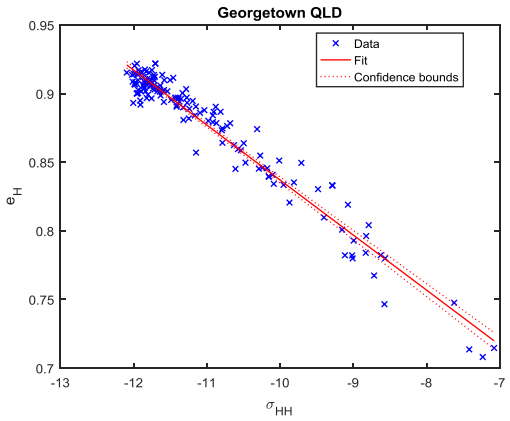
Georgetown QLD
Data
Fit
Confidence bounds
e_H
σ_{HH}

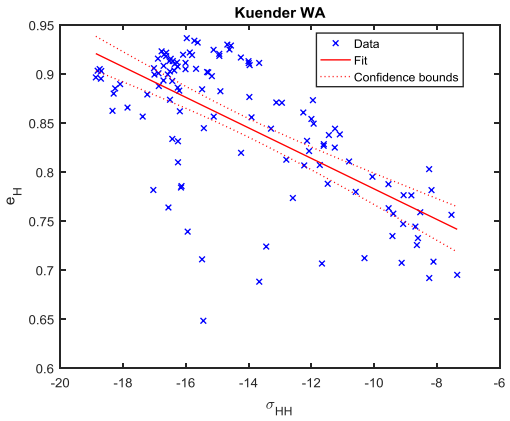
Kuender WA
Data
Fit
Confidence bounds
e_H
σ_{HH}

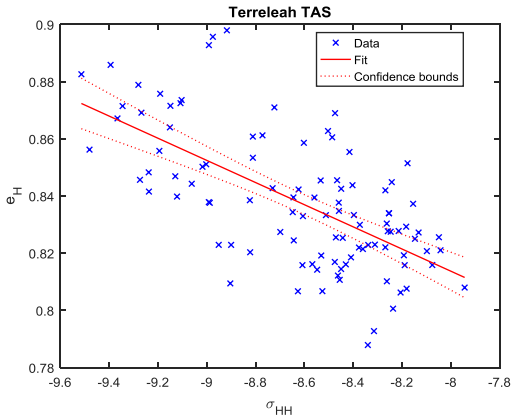
Terreleah TAS
Data
Fit
Confidence bounds
e_H
σ_{HH}

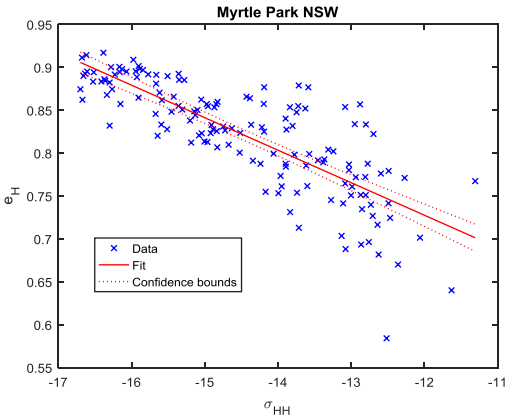
Myrtle Park NSW
Data
Fit
Confidence bounds
e_H
σ_{HH}

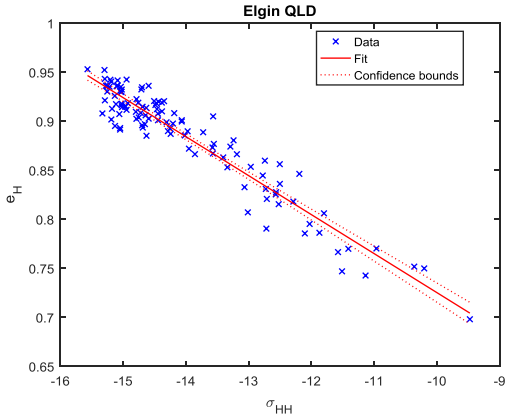
Elgin QLD
Data
Fit
Confidence bounds
e_H
σ_{HH}

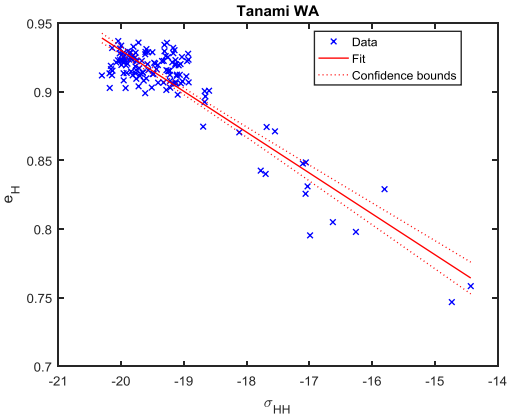
Tanami WA
Data
Fit
Confidence bounds
e_H
σ_{HH}

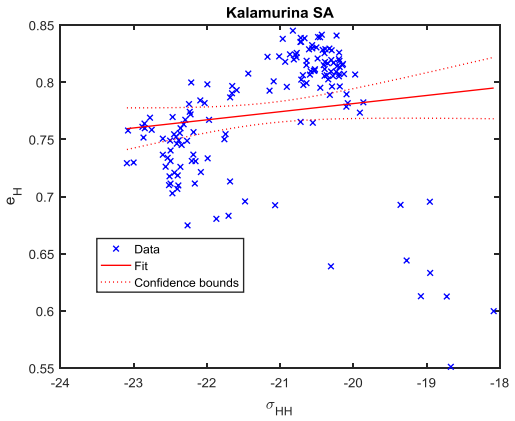
Kalamurina SA
Data
Fit
Confidence bounds
e_H
σ_{HH}

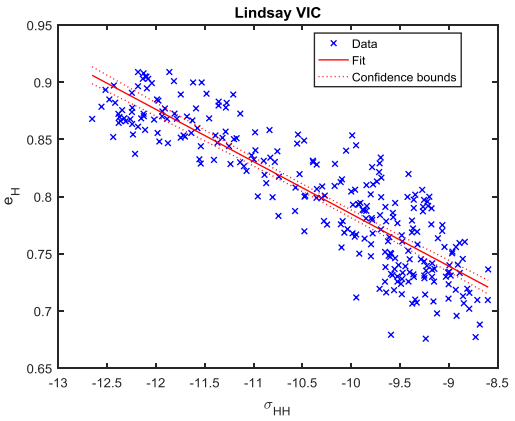
Lindsay VIC
Data
Fit
Confidence bounds
e_H
σ_{HH}

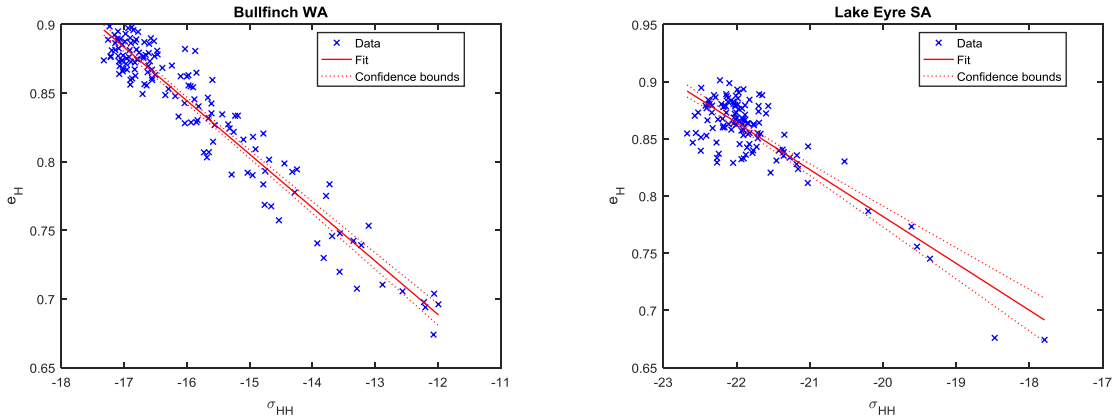

Figure 6-19: Relationship between the horizontal emissivity and the horizontal co-polarized backscatter coefficients.

6.3.4 Analysis of time series

The temporal behavior can be analyzed in the following subsections. For this part of the study, it is important to note that target areas refer to pixels with an area equal to approximately 100 km^2.These regions have substantial variabilities due to its size. For instance, one pixel can be part of two different climate classes. Each pixel center is related to a Weather Station that measures the rainfall data and, in some occasions, the stations may not be representative for the whole area. Observations of daily rainfall are nominally made at 9 am local clock time and record the total precipitation for the preceding 24 hours. If, for some reason, an observation is unable to be made, the next observation is recorded as an accumulation, since the rainfall has been accumulating in the rain gauge since the last reading [19]. That is the case of some of the peaks that appear in the graphics.

The SCA algorithm can fail when there is RFI, due to high topography or when, because of the quality parameters, the SCA uncertainty is higher than 4%. In the graphics represented below there are constant periods of SM_{SCA} that show this fail (because data is missing). There are 5 of the 16 sites that do not have SM_{SCA} data. As a substitude, the model SM_{NCEP} is used. The advantatges of using SM_{SCA} data is that it is more accurate since it is not a model.

The emissivity is taken every 7 days so the changes appear to be drastic.

6.3.3.1 Terreleah TAS

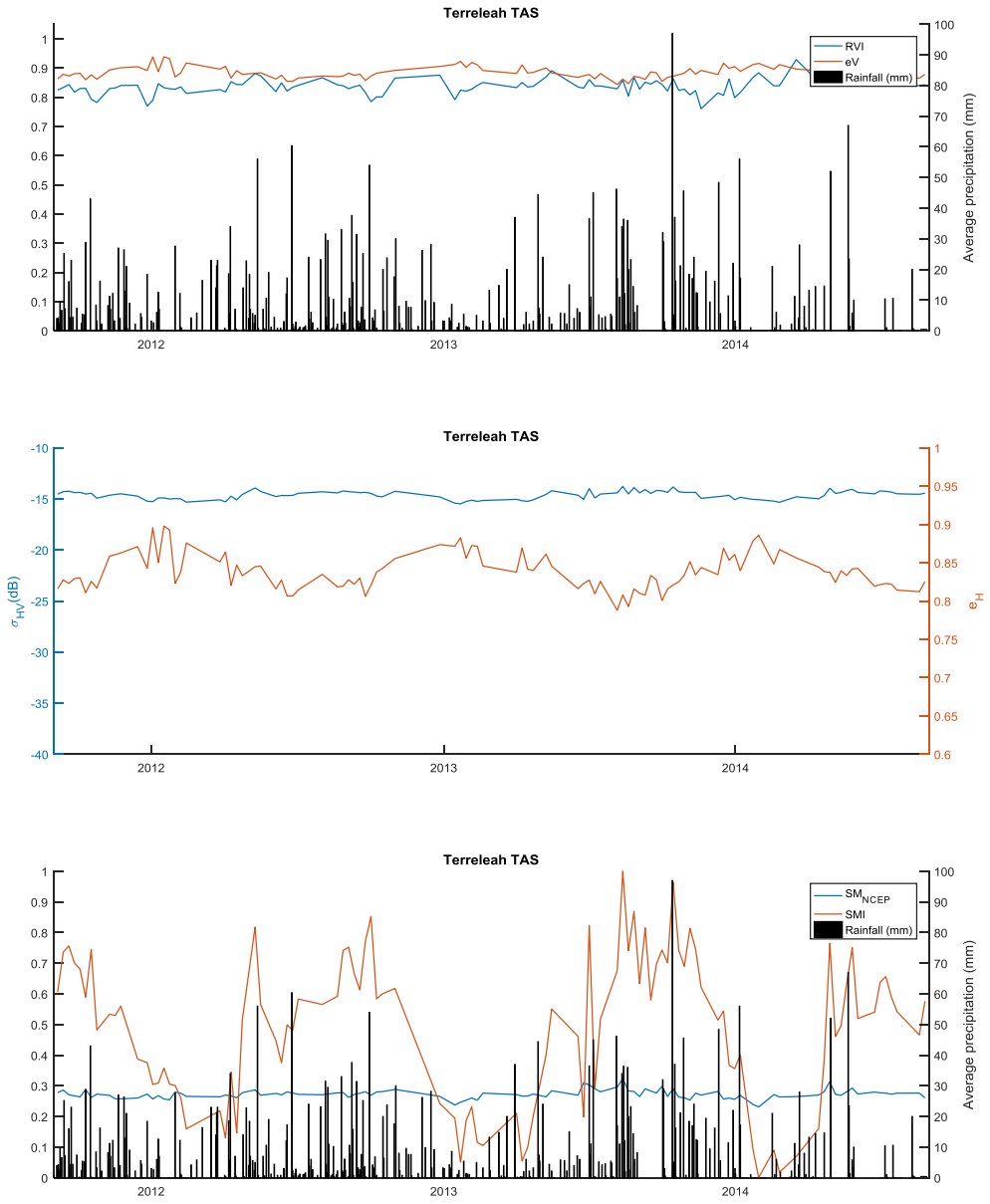

Figure 6-20: The first figure represents the RVI, vertical emissities and the rianfall data throughout the three years data. The second figure represents the $\boldsymbol{\sigma_{HV}}$ and the horizontal emissivity. The third one, characterizes the two SM indicators and the rainfall data

The rain amount of precipitation in the island of Tasmania, is one of the highest in Australia. From April until October it is when it rains the most. However, the soil is wet constantly. The emissivity maximums are from November until April.

The vegetation is very high and the pixel area is mostly covered by rainforest and Eucalypt tall open forest.

The expected values are lower because of the rain and the multiple-scattered pulses that Aquarius received.

Tasmania is well known by its wet climate. This can be easily seen in the SMI and SM_{NCEP} indicators. Apart from the differences between them, already explained in other graphics, it can be seen that both have almost the same average. Also, in this pixel it is important to take into account that the vegetation in Tasmania is predominated by trees and high vegetation that can affect the satellite's measures.

6.3.3.2 Talmalmo NSW

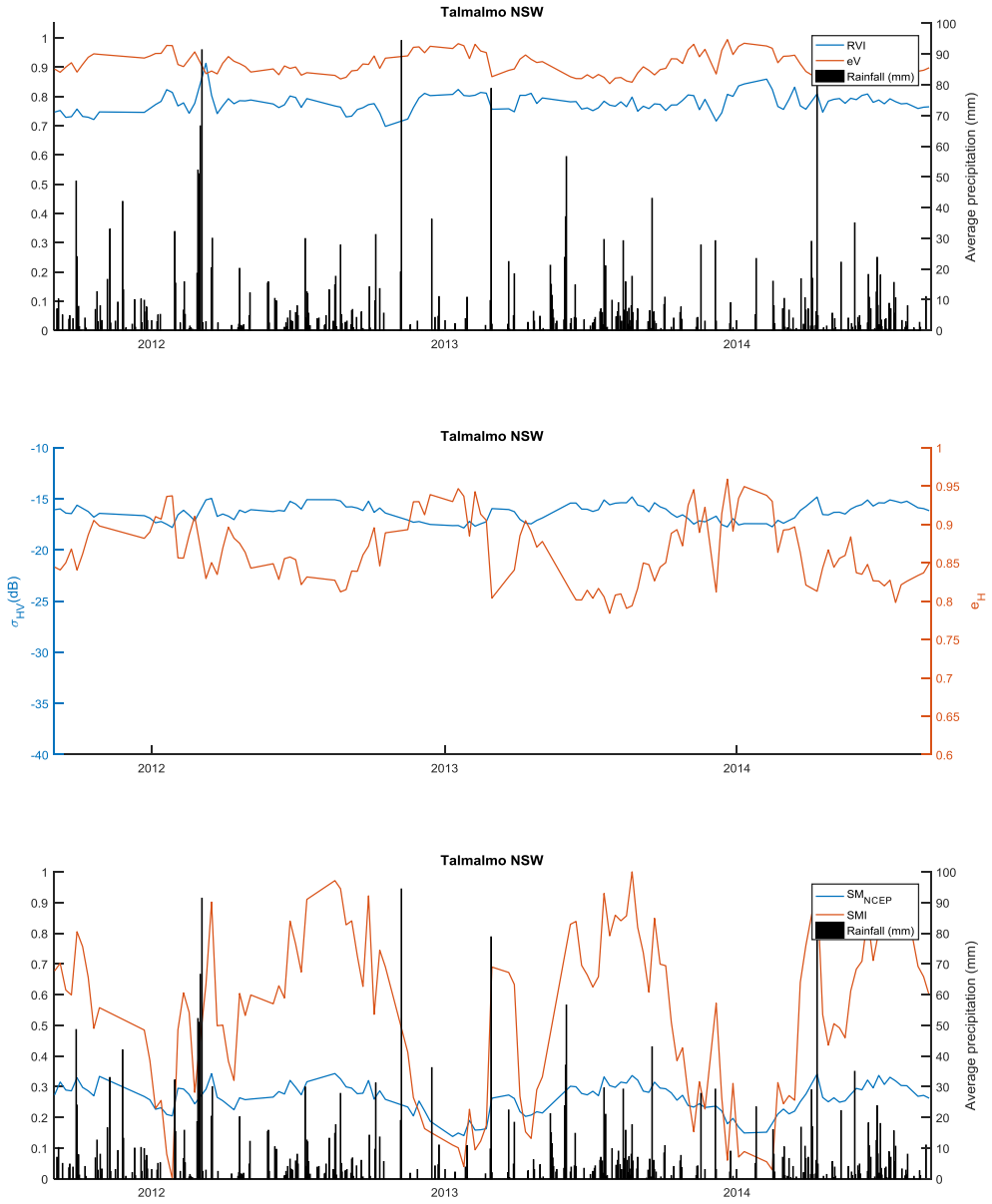

Figure 6-21: The first figure represents the RVI, vertical emissities and the rianfall data throughout the three years data. The second figure represents the $\boldsymbol{\sigma_{HV}}$ and the horizontal emissivity. The third one, characterizes the two SM indicators and the rainfall data

This pixel is located in an area where there are different altitude levels. For example the Weather Station is located

at sea level but surrounded by mountainous terrain of 300-600m high. Because of the size of the pixel and this altitude variabilities, the precipitation values are not representative of the whole region.

The rain peak of 2012 does not match the SM conditions because there was a gap of rain data. From the satellite measurements it is concluded that the peak is due to the accumulation of rain.

The rain conditions allow vegetation as Mallee woodlands and shrublands, in the region. There is no dry season in this area. That high level of vegetation can be appreciated in the RVI and cross-polar backscatter curves.

6.3.4.3 Tanami WA

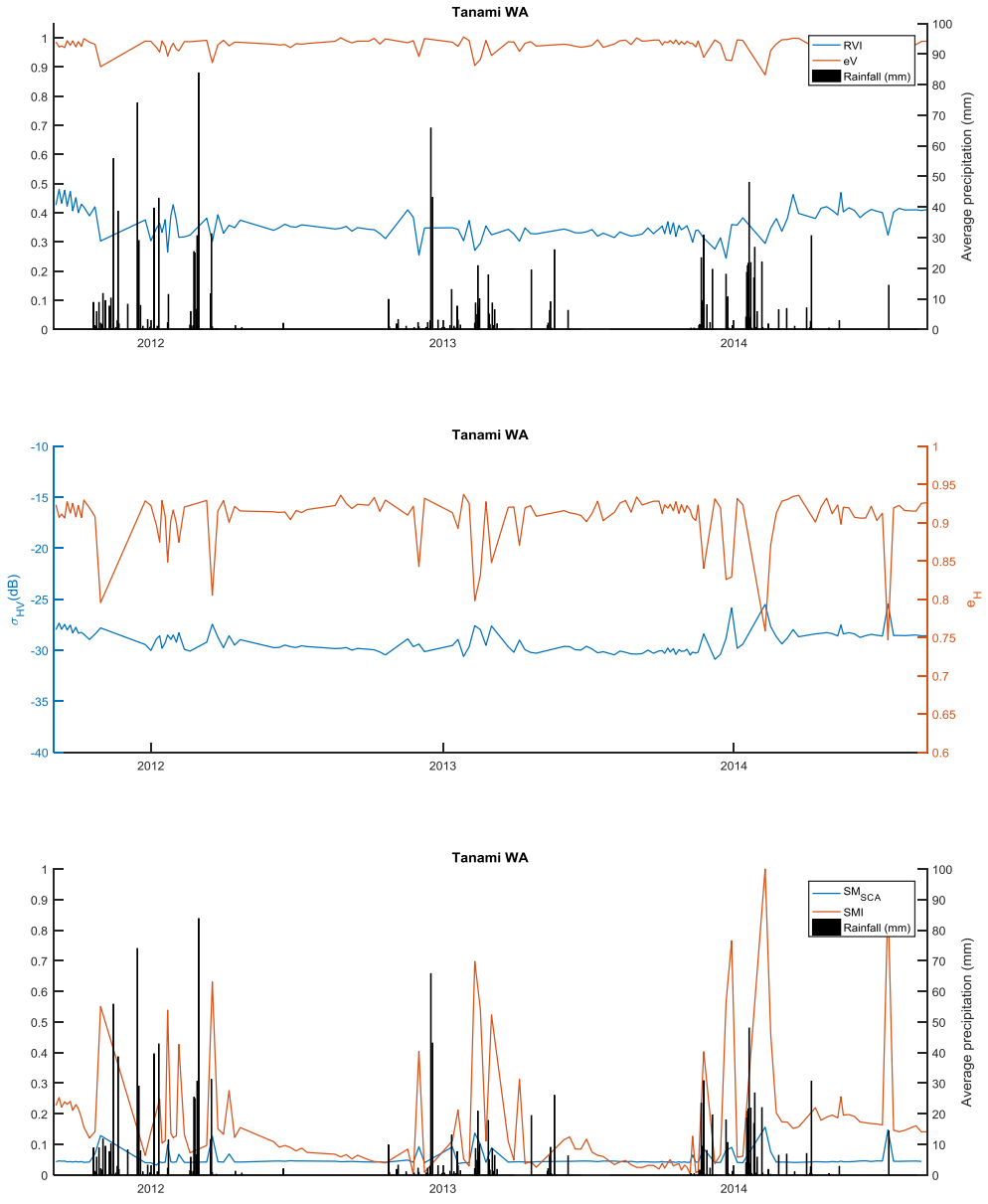

Figure 6-22: The first figure represents the RVI, vertical emissities and the rianfall data throughout the three years data. The second figure represents the $\boldsymbol{\sigma_{HV}}$ and the horizontal emissivity. The third one, characterizes the two SM indicators and the rainfall data.

The SMI and SM_{SCA} maximums, are during the wet season from October until March. The emissivity experience as well their minimums in that period. However, because the pixel is in between the grassland and desert climate classes, the emissivity have high values and the vegetation is higher than expected. The periods with constant SM_{SCA} are due to missing values. The SCA algorithm has missing values when the uncertainty is higher than 4%.

Despite the amount of precipitations during the wet season, Soil Moisture values do not present a big difference between dry and wet seasons. The mean of both Soil Moisture indicators is lower than in previous pixels but there have been more precipitations than in, for example, Kalamurina pixel. This behaviour could be produced by the position of the rainfall station. As explained before, this pixel has part grassland and par desert. Probably the station is located in the grassland part where the precipitations happen to occur more often. Also the satellites average the desert part of the pixel which is dry with the wetter grassland part. This leads into a low mean for both Soil Moisture indicators compared with the precipitation showed.

6.3.4.4 Ingomar SA

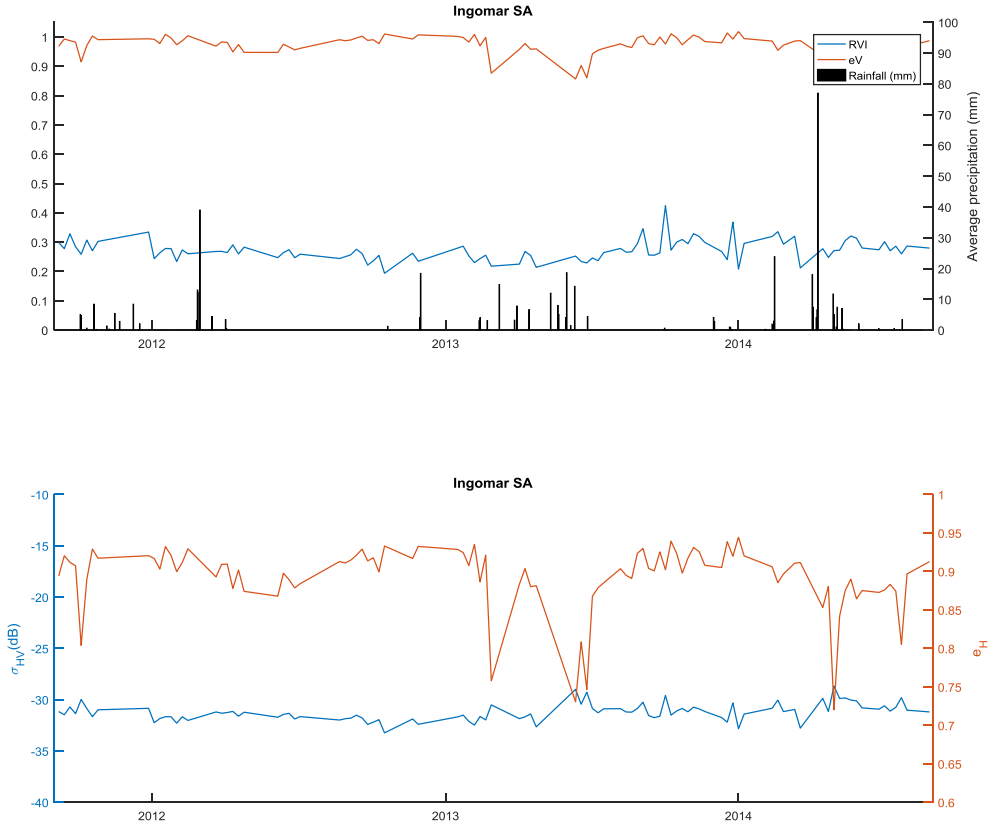

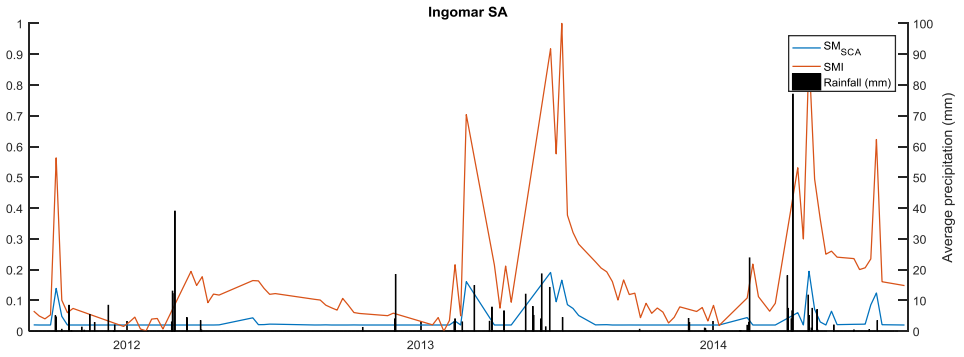

Figure 6-23: The first figure represents the RVI, vertical emissities and the rianfall data throughout the three years data. The second figure represents the $\boldsymbol{\sigma_{HV}}$ and the horizontal emissivity. The third one, characterizes the two SM indicators and the rainfall data

Ingomar SA is another pixel situated in the desert. The rain is scarce and does not match the SM and emissivity data.

Desert zones highlight by their super dry climate and soil. After a dry period the soil will be so dry that it will not be able to filtrate any precipitation that may happen and the water will flood the area. This flooding will affect the satellite which will see the water instead of the soil moisture, thus it will take measures of the water instead of the amount of water contained in the soil. These behaviors can be seen in the first rains of 2013, where a small amount of rainfall boosts the SMI indicator almost to 1.

SM_{SCA} has missing data from 2011 until 2013 (see explanation in 6.3.3.1 Analysis of time series).

6.3.4.5 Nemarluk NT

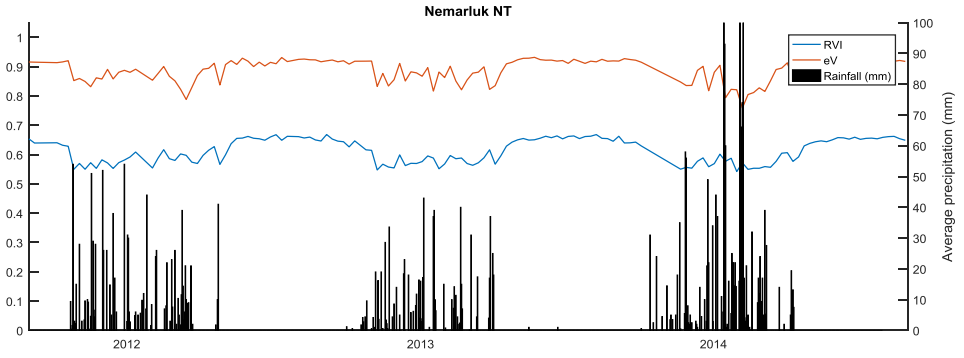

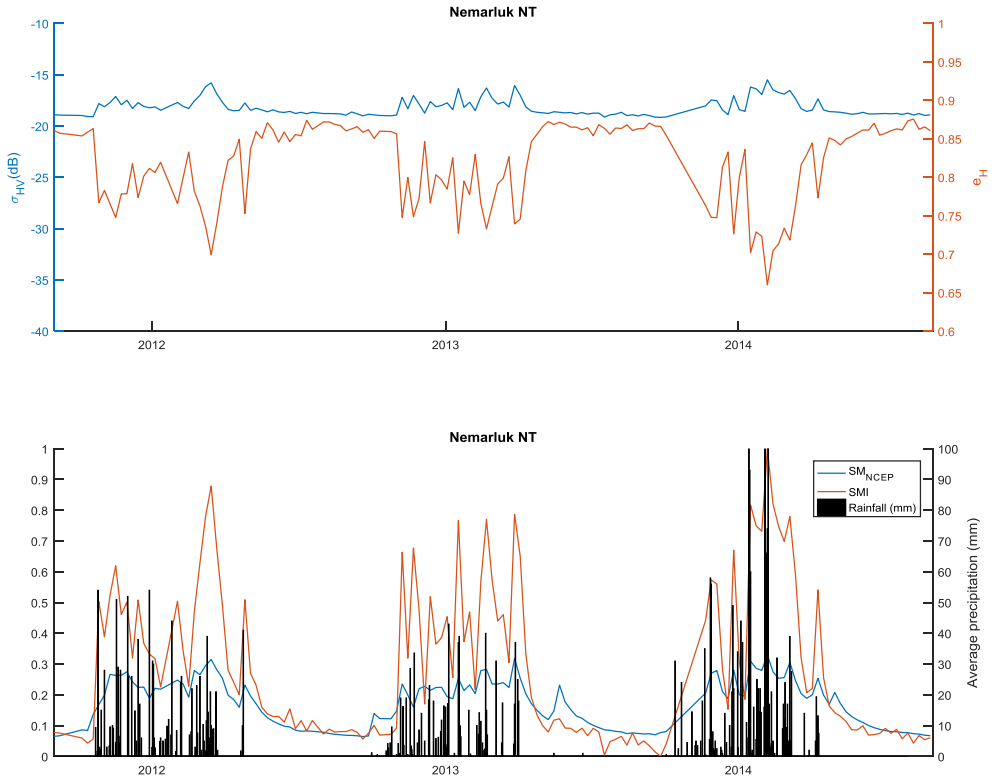

Figure 6-24: The first figure represents the RVI, vertical emissities and the rianfall data throughout the three years data. The second figure represents the $\boldsymbol{\sigma_{HV}}$ and the horizontal emissivity. The third one, characterizes the two SM indicators and the rainfall data

The most remarkable characteristic of these graphics is how the rainfall trains affect all the variables. The rainy season goes from October until April. The emissivity have lower values than other target areas. The cause could be the dense vegetation.

6.3.4.6 Tablelands NT

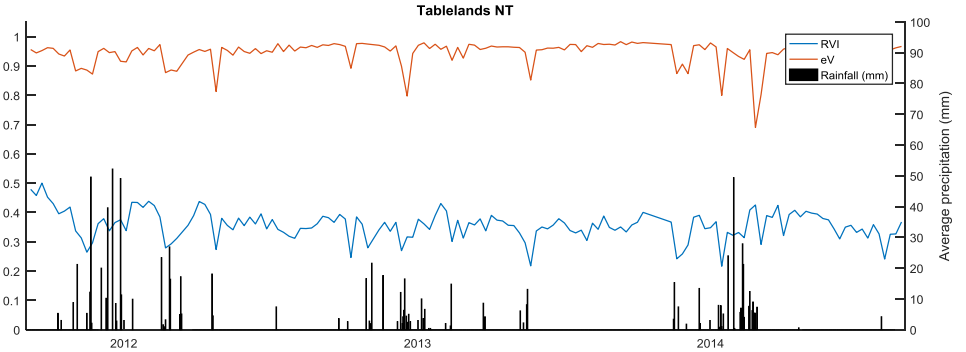

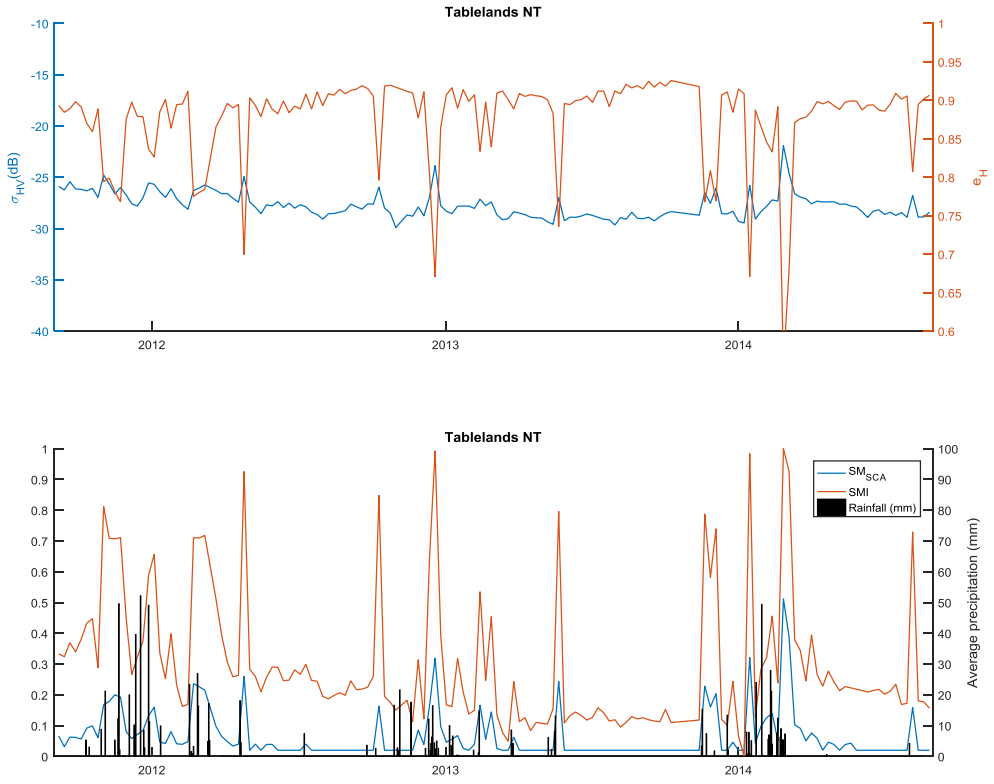

Figure 6-25: The first figure represents the RVI, vertical emissities and the rianfall data throughout the three years data. The second figure represents the $\boldsymbol{\sigma_{HV}}$ and the horizontal emissivity. The third one, characterizes the two SM indicators and the rainfall data

Tablelands NT pixel is in the desert, with a very hot period between the months of April and November. The SMI is not a very good index during these months. The region is drought during winter (see explanation in 6.3.4.4 Ingomar SA).

6.3.4.7 Kuender WA

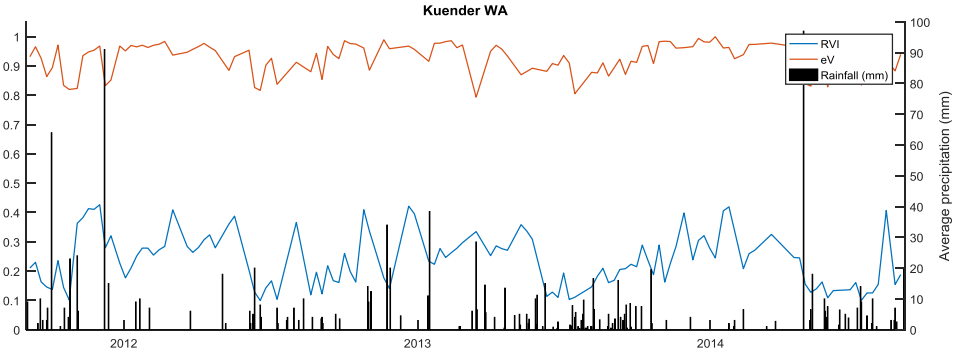

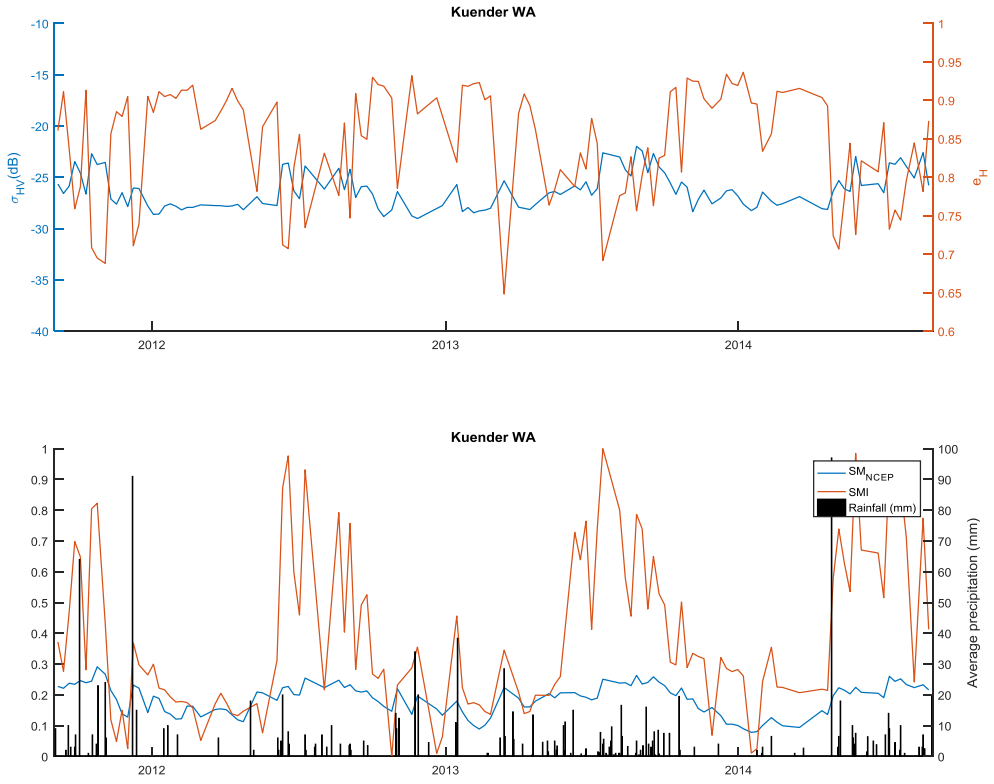

Figure 6-26: The first figure represents the RVI, vertical emissities and the rianfall data throughout the three years data. The second figure represents the $\boldsymbol{\sigma_{HV}}$ and the horizontal emissivity. The third one, characterizes the two SM indicators and the rainfall data

Agricultural fields are the principal vegetation in the pixel area. The area has interferences from several towns and lakes.

In the late 2011 and mid-2014, there are two erroneous rain peaks that are accumulation of rain. It can be observed that the SMI reaches its maximum periodically during the rainy season and not in those two peaks.

In the second graphic, it can be appreciated that the RVI changes rapidly and drastically. As this short periods of change do not correlate with the time needed for the vegetation to grow, it is noticed that RVI is not a good indicator for the area. Although σ_{VH} is a better indicator for Kuender WA, its peaks are caused by the rain and not by a vegetation increase.

6.3.4.8 Lake Eyre SA

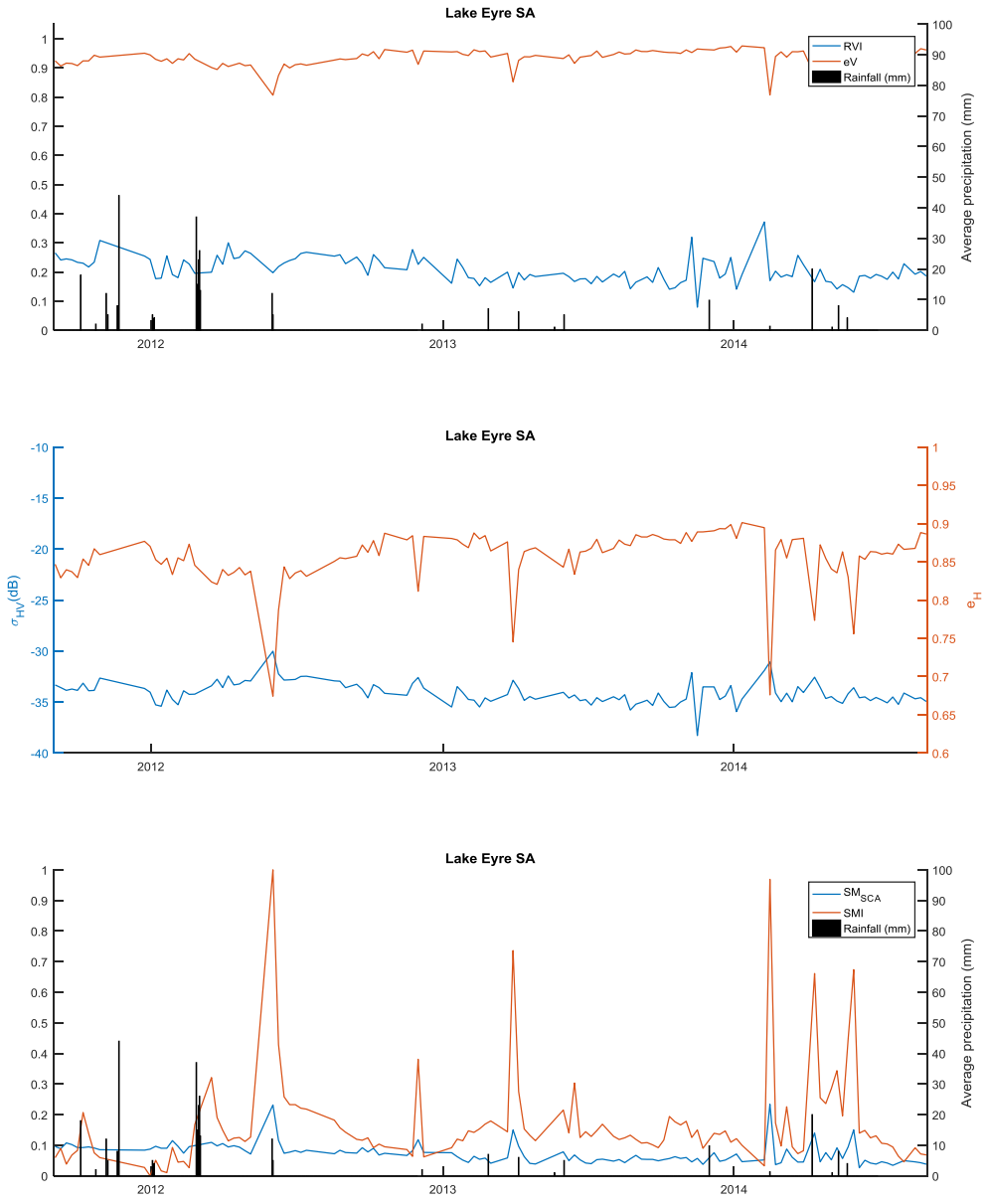

Figure 6-27: The first figure represents the RVI, vertical emissities and the rianfall data throughout the three years data. The second figure represents the $\boldsymbol{\sigma_{HV}}$ and the horizontal emissivity. The third one, characterizes the two SM indicators and the rainfall data

The rainfall data for the end of 2011 and the start of 2012 is not well correlated. However, the other peaks are well correlated.

It is a dry area situated in the desert. That is the cause of the low SM and the high emissivity. Although, they are some lakes in the area, they are mostly dry. The predominant vegetation for the area is hummock grassland.

6.3.4.9 Ngaanyatjarra-Giles WA

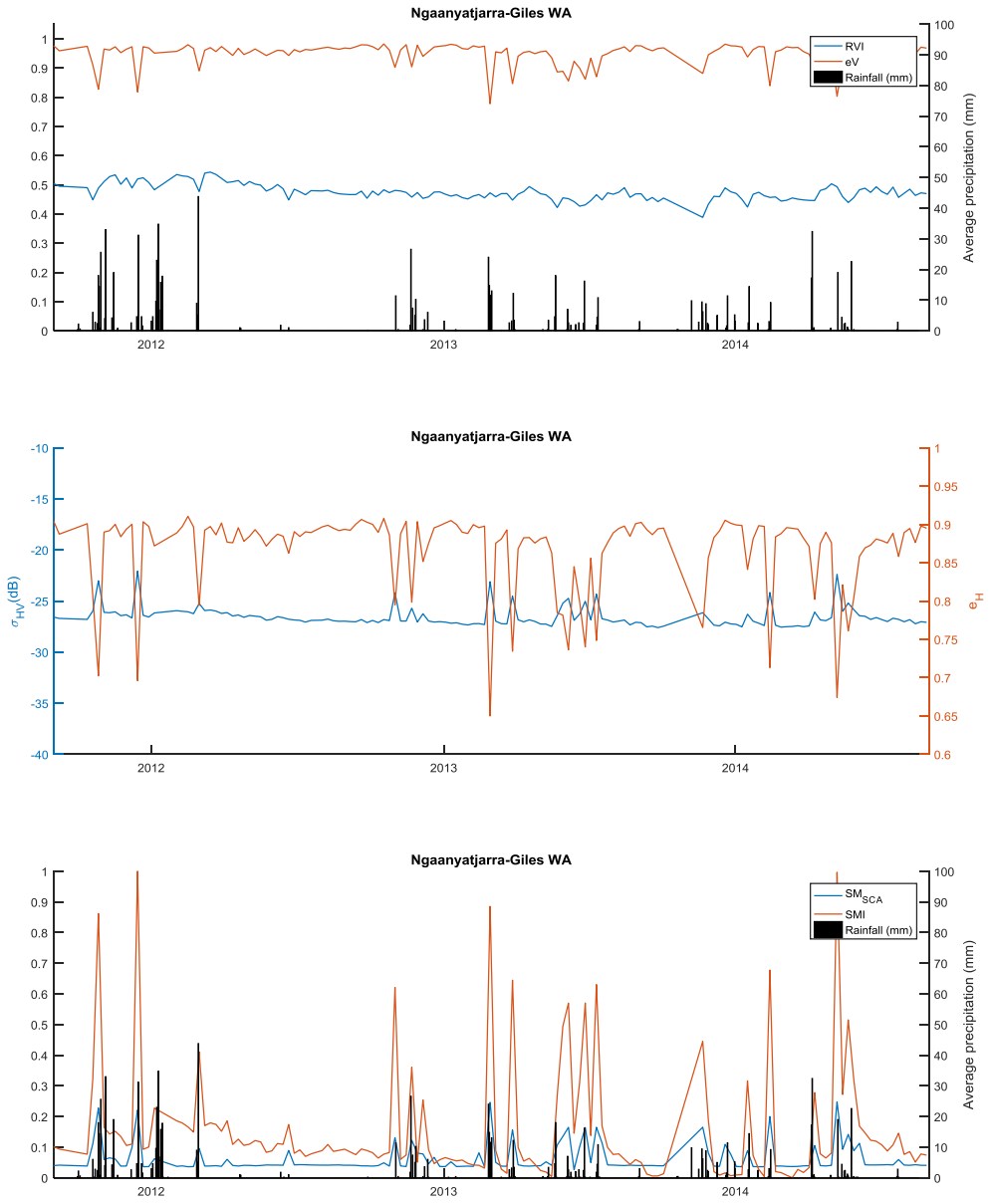

Figure 6-28: The first figure represents the RVI, vertical emissities and the rianfall data throughout the three years data. The second figure represents the $\boldsymbol{\sigma_{HV}}$ and the horizontal emissivity. The third one, characterizes the two SM indicators and the rainfall data

In this site, the rainfall is low. Accordingly, the SM is low but it has peaks in the rainy days due to possible floods. However, the evaporation occurs fast. Vertical emissivity and horizontal emissivity are affected by the rainy days with minimums.

As mentioned before, there are some regions in the desert with a higher RVI than expected. The Ngaanyatjarra-Giles WA pixel is a good example.

6.3.4.10 Lindsay VIC

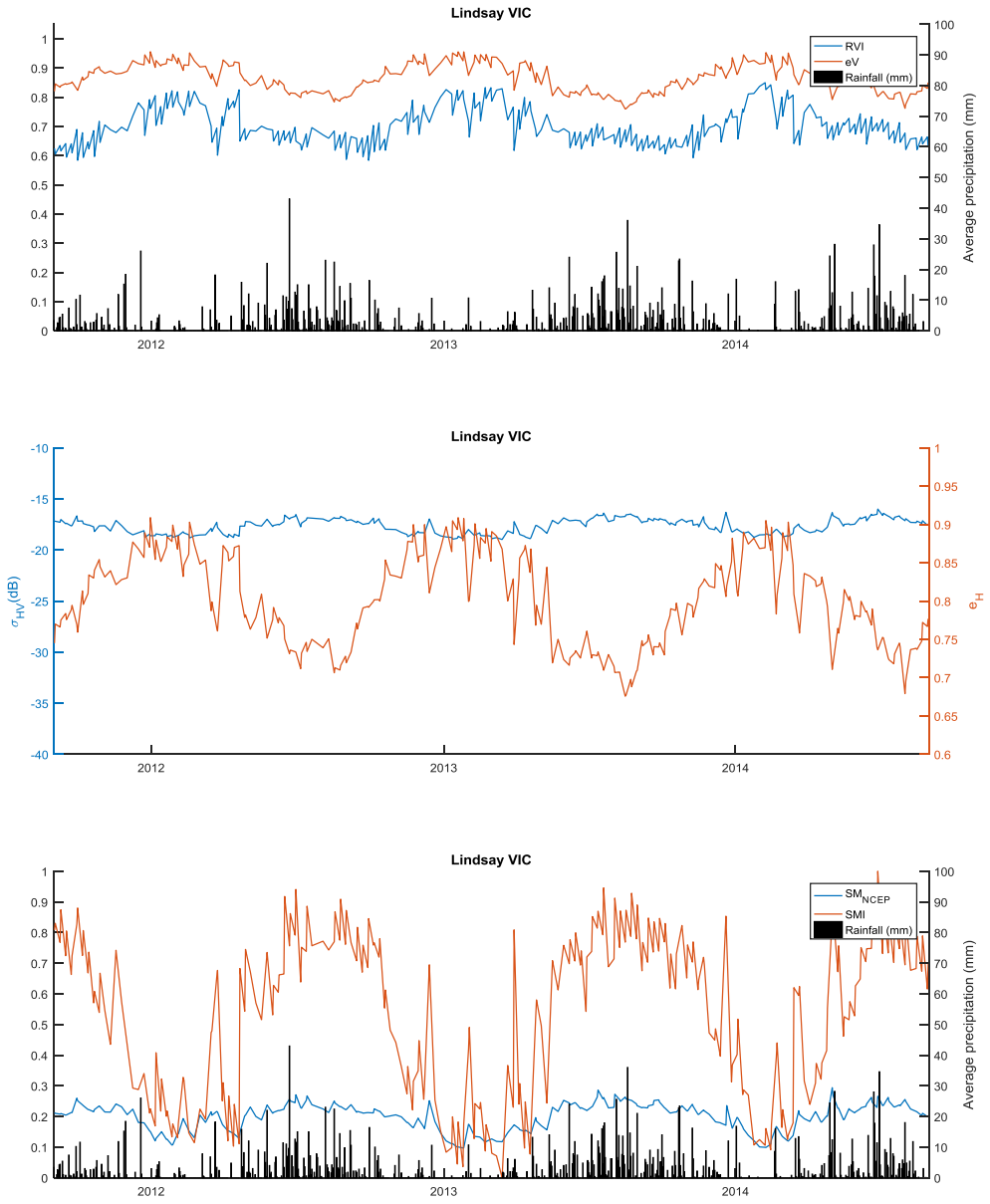

Figure 6-29: The first figure represents the RVI, vertical emissities and the rianfall data throughout the three years data. The second figure represents the $\boldsymbol{\sigma_{HV}}$ and the horizontal emissivity. The third one, characterizes the two SM indicators and the rainfall data

In the Lindsay pixel, emissivity and SM are well correlated with rainfall data. The rain period goes from May until September and it is when the SM is higher and the emissivity is lower. The emissivity increase when the soil is drier.

The RVI and σ_{VH} show that it is a well vegetated region. The high values of the variables can be due to the several forests in the area but, grassland and green agricultural fields are a possible cause of the RVI seasonal variations. These variations occur after the rain is consolidated in the terrain and it has a period to growth.

6.3.4.11 Georgetown QLD

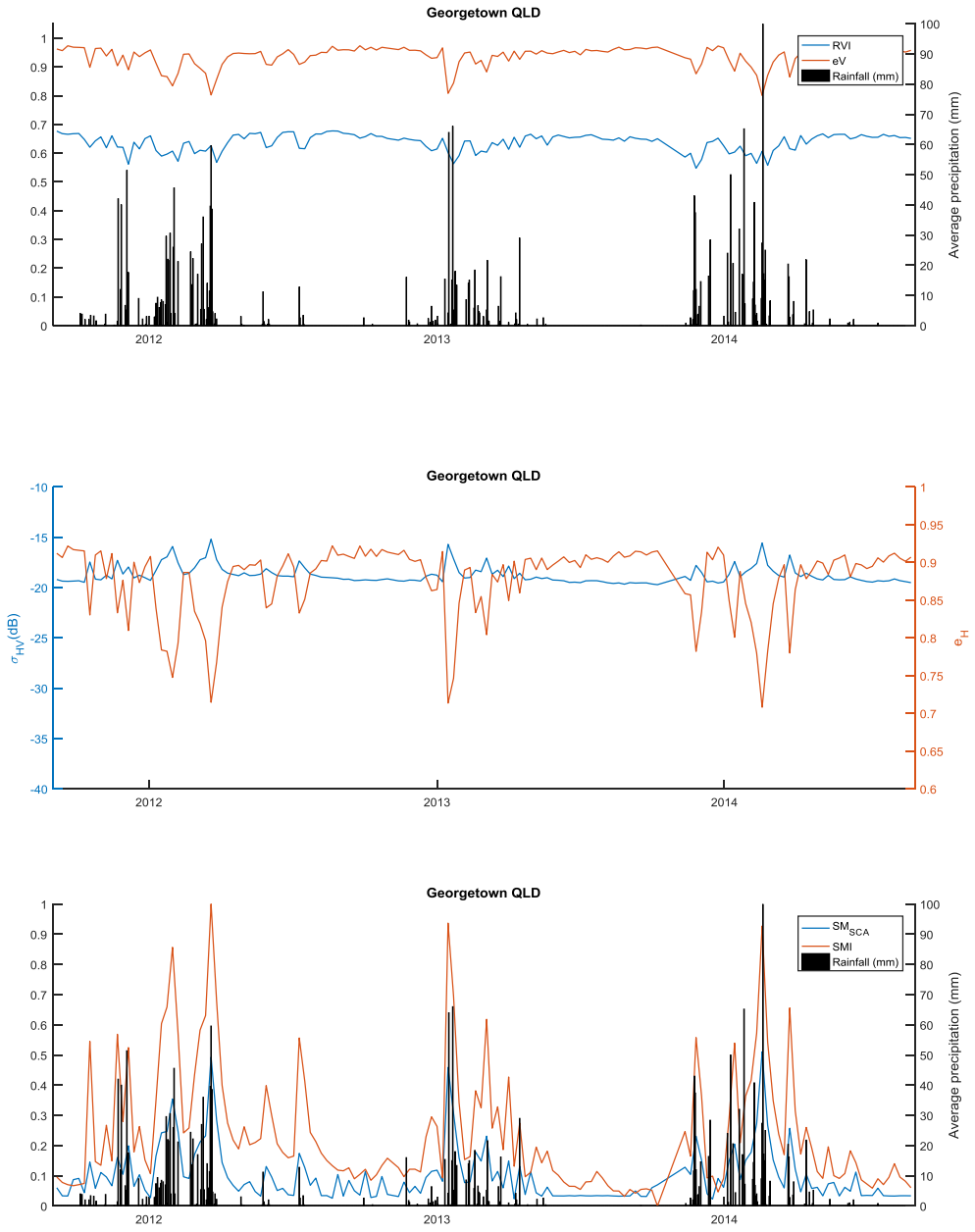

Figure 6-30: The first figure represents the RVI, vertical emissities and the rianfall data throughout the three years data. The second figure represents the $\boldsymbol{\sigma_{HV}}$ and the horizontal emissivity. The third one, characterizes the two SM indicators and the rainfall data

In the pixel of Georgetown QLD, the rain is very well correlated with the SM data, the emissivity and the vegetation. During dry periods the emissivity have higher values. The vegetation is tall, constant and dense. The climate is tropical and the terrain is rough.

The horizontal emissivity is higher than in other areas. This effect could be because of the predominant trees.

Looking into the Soil Moisture data values this pixel has a particularity, both indicators have very similar values. It can be observed from SM variable that there is an absence of precipitation data. As well, some SM_{SCA} values are missing during 2013 (see explanation in 6.3.3.1 Analysis of time series).

6.3.4.12 Myrtle Park NSW

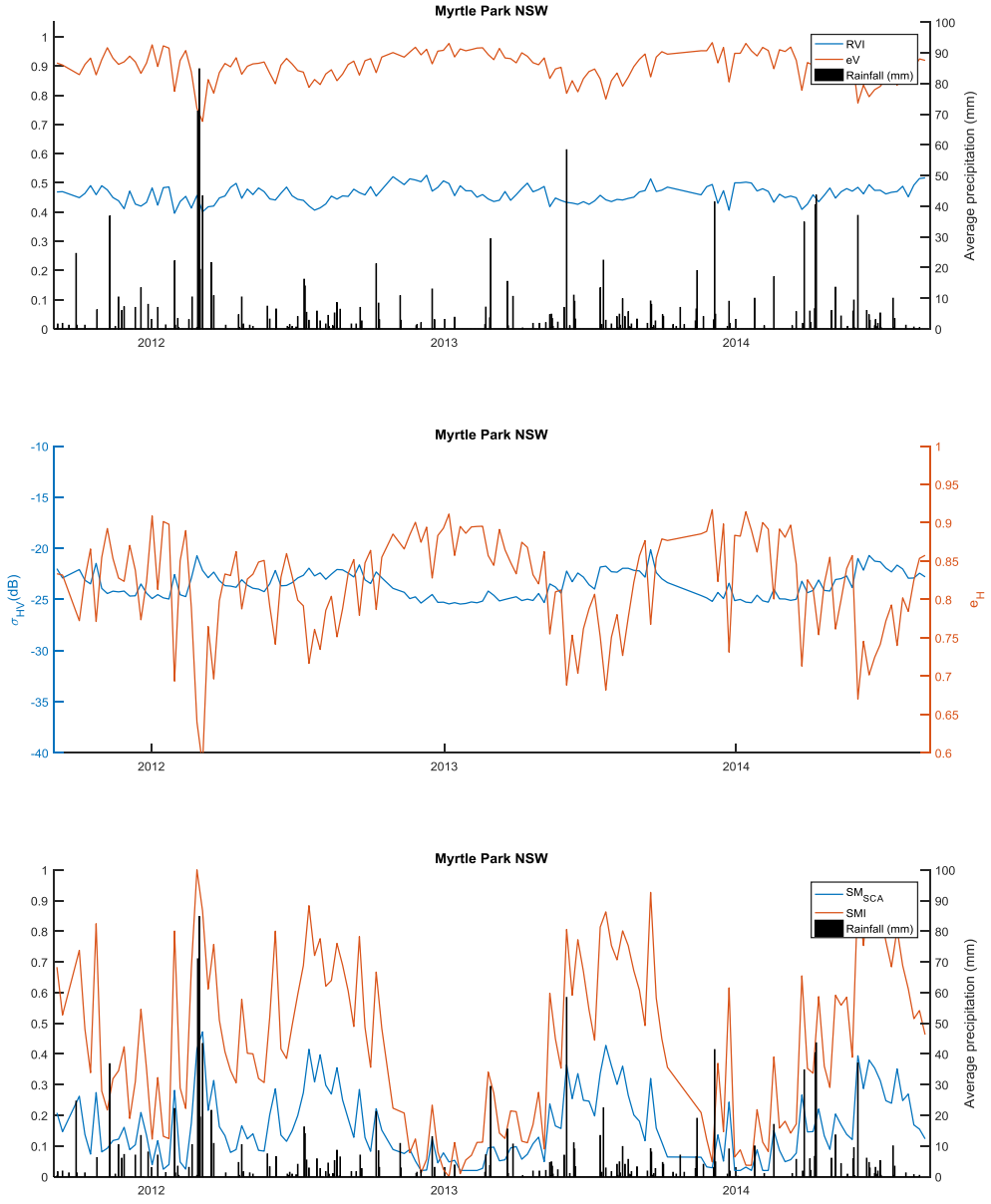

Figure 6-31: The first figure represents the RVI, vertical emissities and the rianfall data throughout the three years data. The second figure represents the $\boldsymbol{\sigma_{HV}}$ and the horizontal emissivity. The third one, characterizes the two SM indicators and the rainfall data

The vegetation is constant throughout the year. The area includes two national parks, two towns and many

agricultural fields.

The emissivity oscillate with the rain trains. When there is a drier period, the emissivity increase. During the rainy peak days, the emissivity decrease in the nadir rainfall.

Myrtle Park pixel, situated in NSW, is affected by constant rainfalls throughout the year. Therefore, soil moisture values of both indicators are high. As in the other pixels, SM is highly affected by the rainfall following it with a peak every time it precipitates on the zone.

6.3.4.13 Bullfinch WA

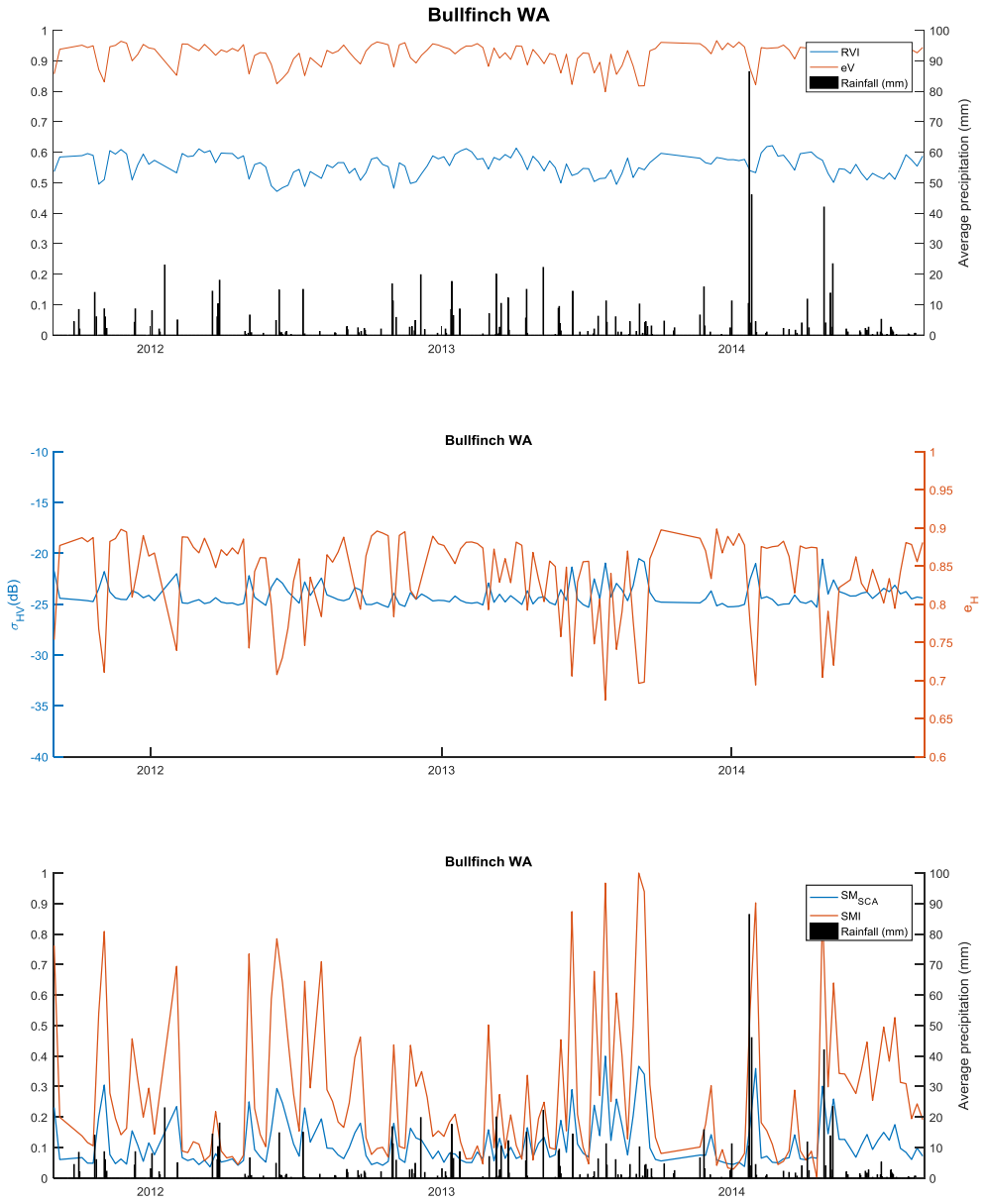

Figure 6-32: The first figure represents the RVI, vertical emissities and the rianfall data throughout the three years data. The second figure represents the $\boldsymbol{\sigma_{HV}}$ and the horizontal emissivity. The third one, characterizes the two SM

indicators and the rainfall data

In Bullfinch WA pixel, the horizontal emissivity have higher values than the vertical emissivity. More precisely, the horizontal emissitives are more affected by the rain.

The rainfall is low but it rains the same amount every month, which can be related to constant vegetation. Although the RVI and σ_{VH} variables show that the area is vegetated, they are both affected by the radar noise of the rain.

The SMI and SM_{NCEP} peaks correlate to the rainfall data.

6.3.4.14 Elgin QLD

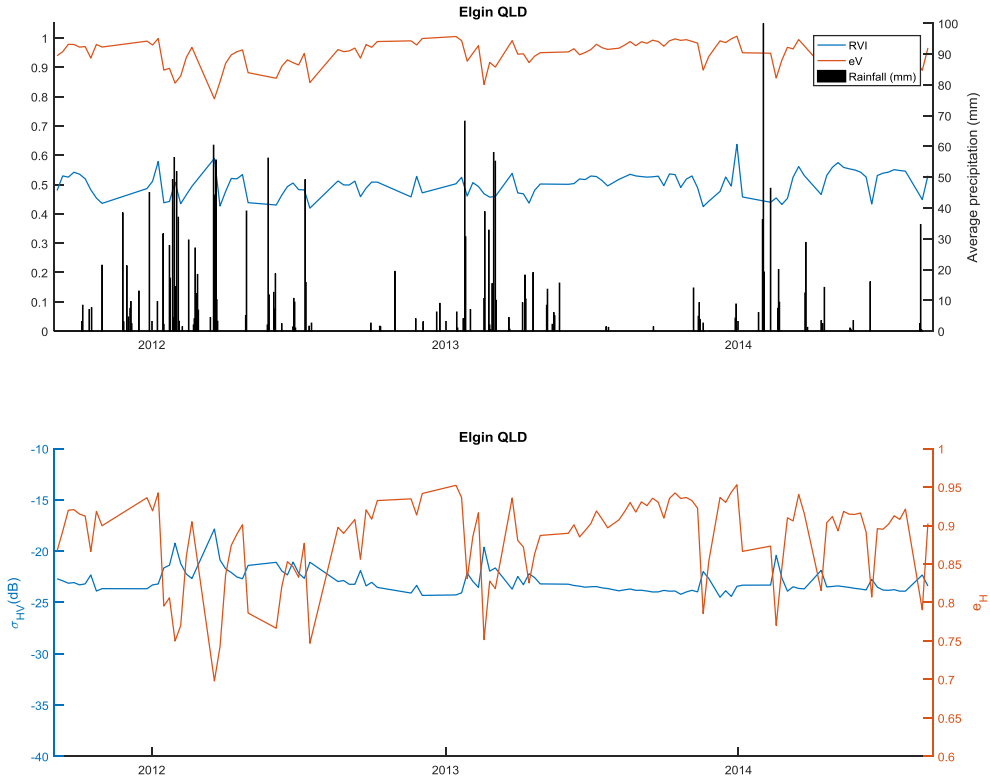

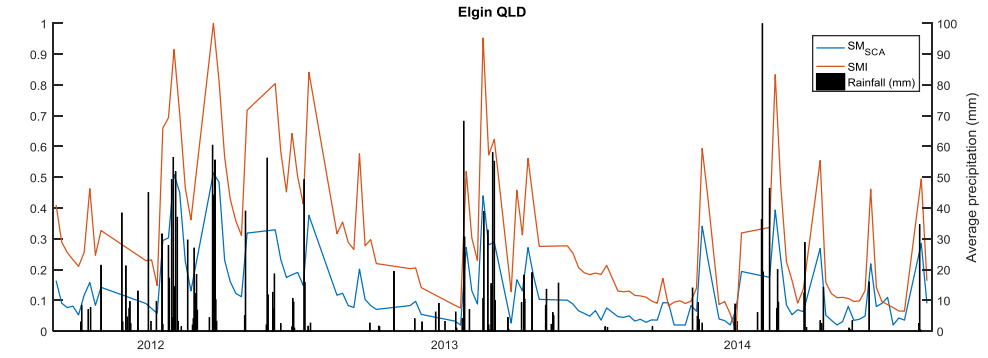

Figure 6-33: The first figure represents the RVI, vertical emissities and the rianfall data throughout the three years data. The second figure represents the σ_{HV} and the horizontal emissivity. The third one, characterizes the two SM indicators and the rainfall data

The Elgin QLD pixel is in the subtropical climate class. It has constant vegetation with a portion of forests and woodlands. Both emissivity have their maximums during the dry season which is from April until September. The terrain is wet throughout the year.

In 2012, the area experimented lower emissivity and higher SM due to the increase of rain.

6.3.4.15 Kalamurina SA

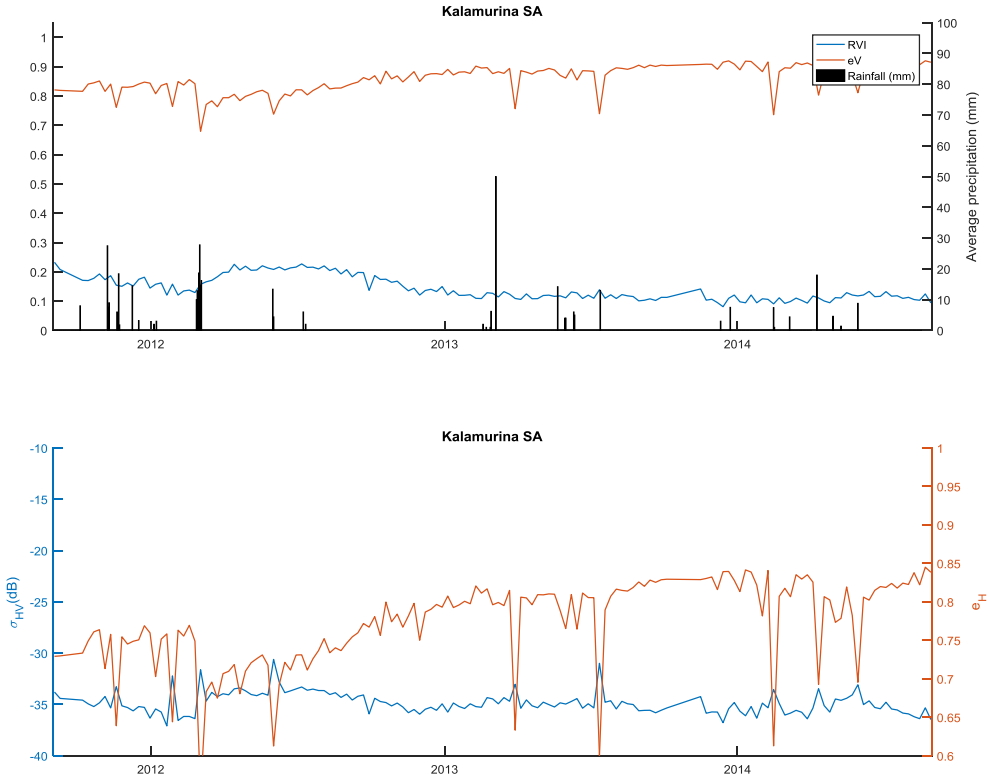

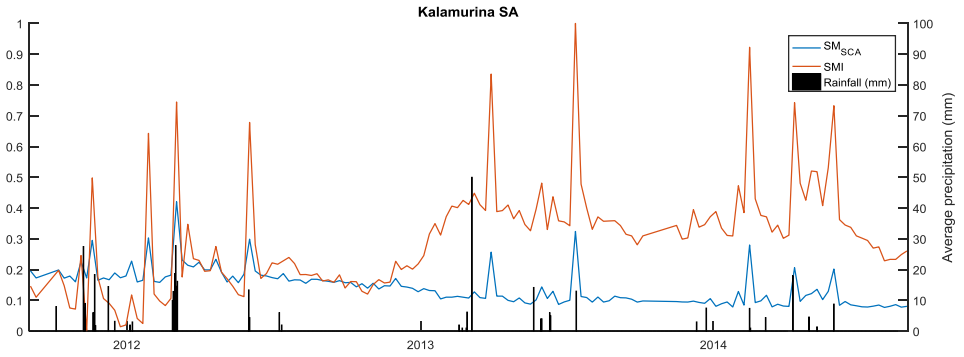

Figure 6-34: The first figure represents the RVI, vertical emissities and the rianfall data throughout the three years data. The second figure represents the $\boldsymbol{\sigma_{HV}}$ and the horizontal emissivity. The third one, characterizes the two SM indicators and the rainfall data

Kalamurina SA is another pixel located in the desert. The predominant vegetation in the area is chenopod shrublands, samphire shrubs and forblands. Therefore, the vegetation in the area is sparse. The emissivity is not as high as expected because it includes some lakes.

The rainfall is low throughout the year so the soil is dry. The SM drastic change of values are due to the rain (see explanation in 6.3.4.11 Ingomar SA).

It can be appreciated, that the horizontal emissivity increase from mid-2012 on. That is because in the end of 2011 and start of 2012 the precipitation were higher than other years. As well, there are some SM peaks during that period that indicate that rain data is missing.

In the early 2013, the SM_{SCA} remains constant while the SMI increases, the reason could be the normalization of SMI ($SMI\boldsymbol{\sigma VV}=\frac{10log_{10}(\sigma_{VV})-\sigma^{min}{}_{VV}}{\sigma^{max}{}_{VV}-\sigma^{min}{}_{VV}}$ **(30)**

6.3.4.16 Bronte Park TAS

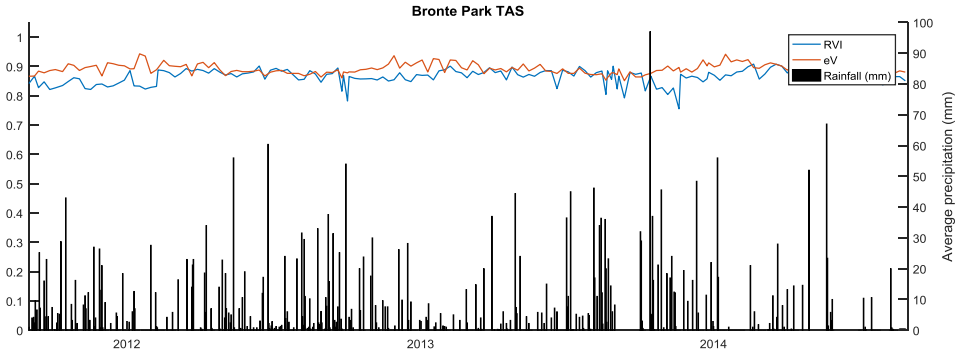

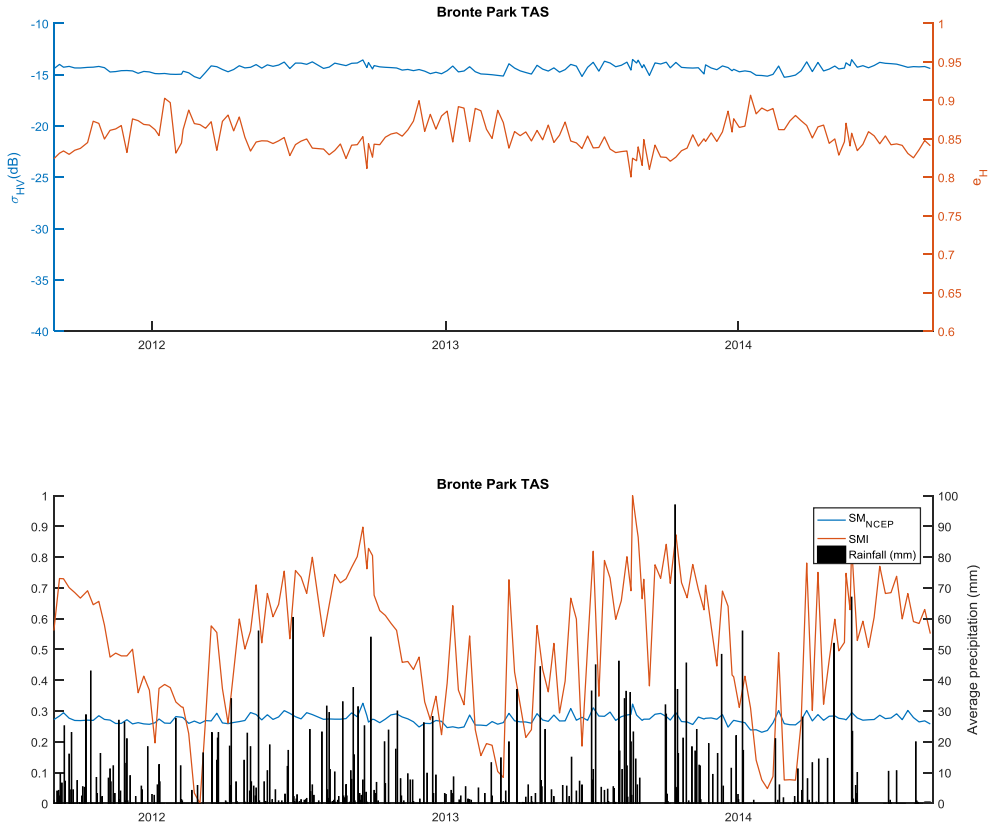

Figure 6-35: The first figure represents the RVI, vertical emissities and the rianfall data throughout the three years data. The second figure represents the $\boldsymbol{\sigma_{HV}}$ and the horizontal emissivity. The third one, characterizes the two SM indicators and the rainfall data

The vegetation is very high and the pixel area is mostly covered by rainforest and Eucalypt tall open forest. The horizontal emissivity have a higher value than other areas, as stated in 6.3.4.10 Georgetown QLD, the reason could be the predominant trees.

The rain amount of precipitation is very high, especially during the months of April to October. Therefore, the Soil Moisture is constantly high too.

The expected values are lower because of the rain and the multiple-scattered pulses that Aquarius received.

7 CONCLUSIONS

This Thesis provides an assessment of the relationship between Aquarius collocated passive and active L-band measurements using three years of obsevations (2011-2014) over Australia. The main conclusions of this work are listed below.

- When looking at the 3 years average of the Aquarius vertical and horizontal emissivity, higher and lower values match with the desert and tropical or temperate climate areas.
- The RVI shows higher values than expected in the arid regions. It also appears to be highly influenced by rain. Still, its temporal average agrees well with the volume of biomass that is found in the temperate and tropical climate areas.
- The relationship between the emissivities and the RVI for the different IGBP areas, suggests that the land cover data cannot provide useful information about the variability in vegetation scattering that is likely to influence the relation between the emissivities changes. This indicates that an optically-based land cover classification (such as IGBP) is not representative of microwave vegetation properties and effects.
- The study between the emissivities and the co-polarized backscatter coefficients shows that there is a high correlation between the two variables. However, there are a few exceptions, particularly the sites in Tasmania and in Kuender WA, which could be affected by radio frequency intereferences. This high correlation could be further explored to develop synergistic retrieval techniques to combine the relative advantages of active and passive measurements (e.g. the SMAP concept)
- From the analysis of time-series, it is deduced that the SMI is a good indicator for the soil moisture changes. On the other hand, SM_{SCA} is consistent with its values.

8 REFERENCES

[1] NASA. [Online]. Available: http://aquarius.umaine.edu/docs/Aquarius_Mission_Brochure_508_Compliant.pdf.

[2] NASA. [Online]. Available: www.smap.jpl.nasa.gov.

[3] W. Wagner, et al «Evaluation of the agreement between the first global remotely sensed soil moisture data with model and precipitation data,» vol. 108, nº JOURNAL OF GEOPHYSICAL RESEARCH, pp. 1-17, 2003.

[4] ESA. [Online]. Available: http://www.esa.int/Our_Activities/Observing_the_Earth/SMOS/Facts_and_figures.

[5] M. Piles, et al «Sensitivity of Aquarius Active and Passive Measurements Temporal Covariability to Land Surface Characteristics,» vol. 53, nº IEEE TANSACTIONS ON GEOSCIENCE AND REMOTE SENSING, pp. 4700-4711, 2015.

[6] NASA. [Online]. Available: http://www2.hawaii.edu/~jmaurer/scatterometry/what_is_scatterometry.html.

[7] R. T. Keating, et al «Tropical Rainfall Measuring Mission (TRMM):US/Japan Science Operations,» nº AIAA-92-0594.

[8] K. Nakagawa, et al «Global Change Observation Mission (GCOM),» nº Proceedings of ISPRS Technical Commission VIII Symposium, 2001.

[9] Fawwaz T. Ulaby, Microwave Remote Sensing: Active and Passive, Volume I: Fundamentals and Radiometry, Artech House Publishers, 1986.

[10] M. Piles, et al «Multiscale soil moisture retrivals from microwave remote sensing observations,» Remote Sensing Laboratory, UPC, Barcelona, 2010.

[11] F. Sabins, et al «Remote Sensing. Principles and Interpretation,» *Geological Magazine,* vol. 135, nº 1, pp. 143-158, 1997.

[12] F. Ulaby, et al Microwave Remote Sensing Volumes 1,2 and 3, 1982.

[13] B. Choudhury, et al «Effect of Surface Roughness on Microwave Emission from Soils,» *Journal of Geophysical Research,* nº 84, pp. 5699-5706, 1979.

[14] J. Wang, et al «Remote Sensing of Soil Moisture Content over Bare Fields at 1.4 GHz fREQUENCY,» *Journal of Geophysical Research,* pp. 5277-5282, 1981.

[15] «NASA Web site,» [Online]. Available: www.nasa.gov.

[16] «SMAP mission,» [Online]. Available: www.remss.com/missions/smap.

[17] R. Bindlish, et al «Global Soil Moisture From the Aquarius/SAC-D Satellite: Description and Initial Assessment,» *IEEE GEOSCIENCE AND REMOTE SENSING LETTERS,* vol. 12, nº 5, pp. 923-927, 2015.

[18] «Australian Government Boreau of Metereology,» [Online]. Available: http://www.bom.gov.au.

[19] P. S. Narvekar, et al «Soil Moisture Retreival Using L-Band Radar Observations,» vol. 53, nº IEEE TRANSACTIONS ON GEOSCIENCE AND REMOTE SENSING, 2015.

[20] Y. Kim, et al «Radar Vegetation Index for Estimating the Vegetation Water Content of Rice and Soybean,» vol. 9, nº IEEE GEOSCIENCE AND REMOTE SENSING LETTERS, pp. 564-568, 2012.

[21] W. Wagner, et al «A study of vegetation cover effects on ERS scatterometer data,» vol. 37, nº IEEE Trans. Geosci. Remote Sens., pp. 938-948, 1999.

[22] M. Piles, et al «Uncertainty Analysis of Soil Moisture and Vegetation Indices Using Aquarius Scatterometer Observations,» *IEEE Transactions on Geoscience and Remote Sensing,* vol. 52, pp. 4259-4271, 2014.

[23] B. Choudhury, et al «A parameterization of effective soil temperature for microwave emission,» *J. Geophys. Res.,* vol. 87, nº C2, pp. 1301-1304, 1982.

[24] J.-P. Wigneron, et al «A simple Parameterization of the L-Band Microwave Emission from Rough Agricultural Soils,» *IEEE TRANSACTIONS OF GEOSCIENCE AND REMOTE SENSING,* vol. 39, nº 8, pp. 1697-1706, 2001.

[25] T. J. Schmugge, et al «Remote sensing in hidrology,» *Advances in Water Resources,* vol. 25, pp. 1367-1385, 2002.

9 APPENDICES

APPENDIX 1

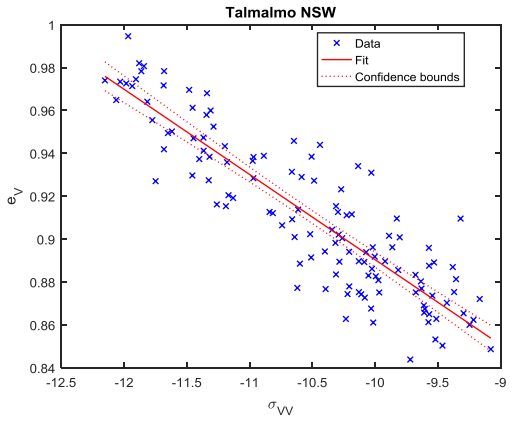
Talmalmo NSW
Data
Fit
Confidence bounds
e_V
σ_{VV}

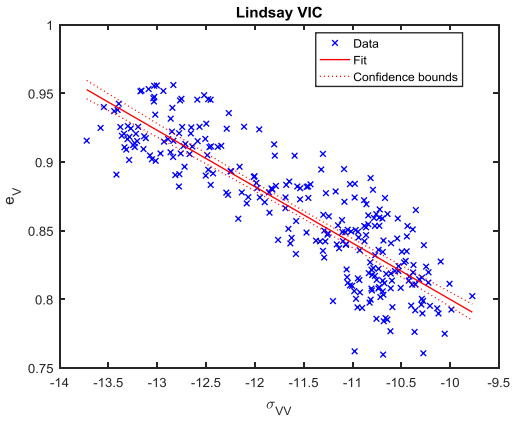
Lindsay VIC
Data
Fit
Confidence bounds
e_V
σ_{VV}

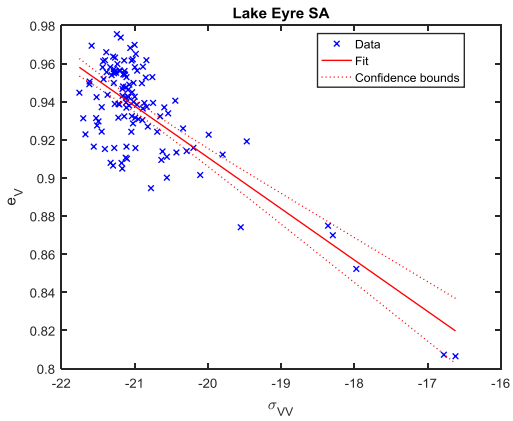
Lake Eyre SA
Data
Fit
Confidence bounds
e_V
σ_{VV}

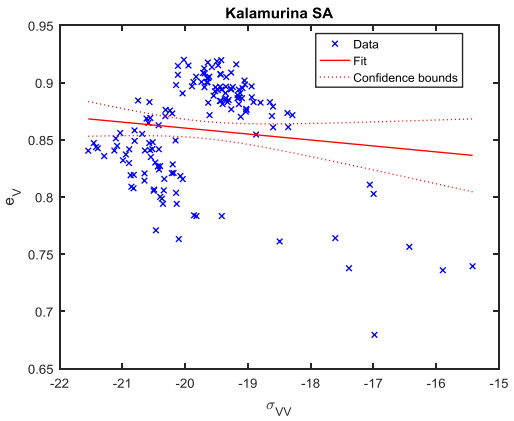
Kalamurina SA
Data
Fit
Confidence bounds
e_V
σ_{VV}

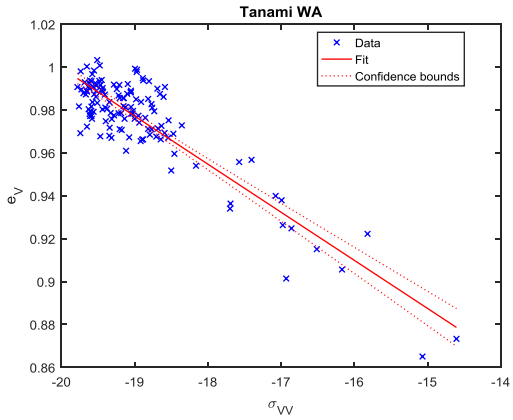
Tanami WA
Data
Fit
Confidence bounds
e_V
σ_{VV}

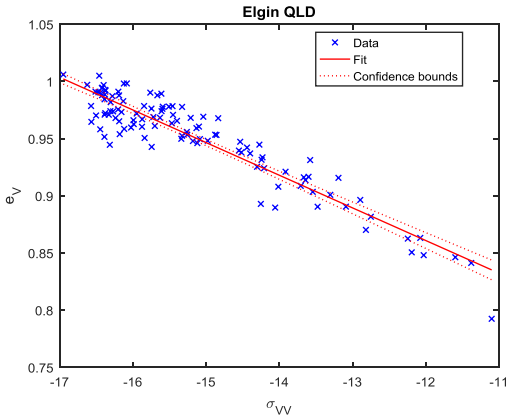
Elgin QLD
Data
Fit
Confidence bounds
e_V
σ_{VV}

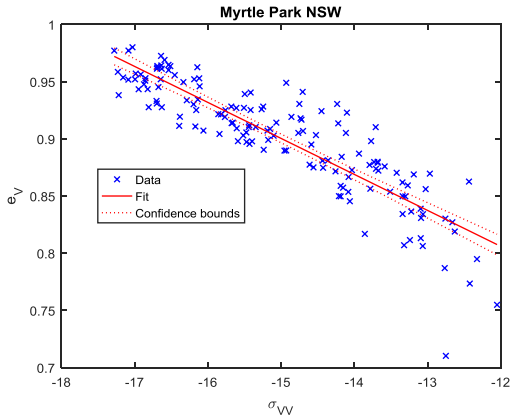
Myrtle Park NSW
Data
Fit
Confidence bounds
e_V
σ_{VV}

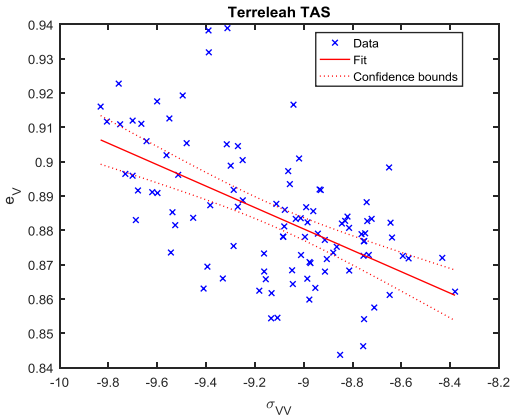
Terreleah TAS
Data
Fit
Confidence bounds
e_V
σ_{VV}

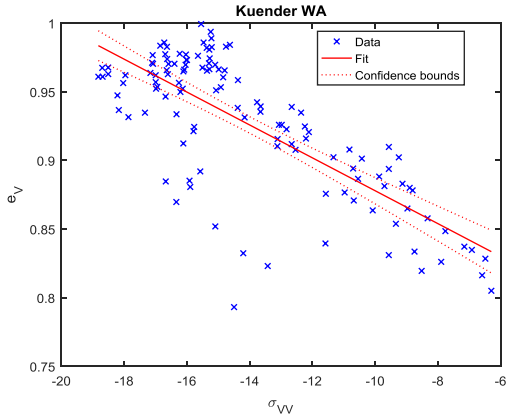
Kuender WA
Data
Fit
Confidence bounds
e_V
σ_{VV}

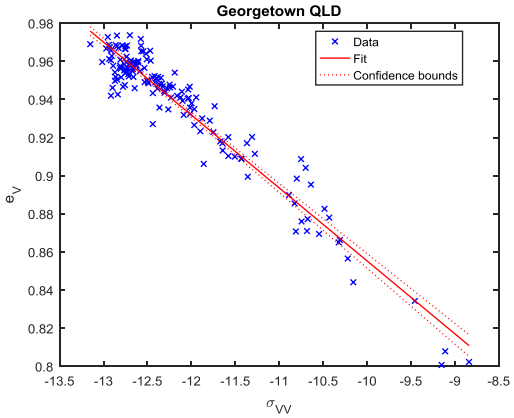
Georgetown QLD
Data
Fit
Confidence bounds
e_V
σ_{VV}

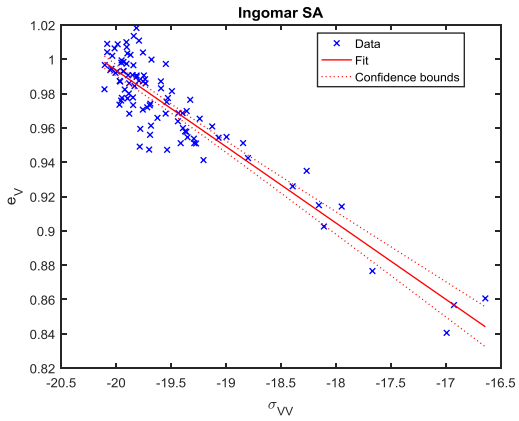
Ingomar SA
Data
Fit
Confidence bounds
e_V
σ_{VV}

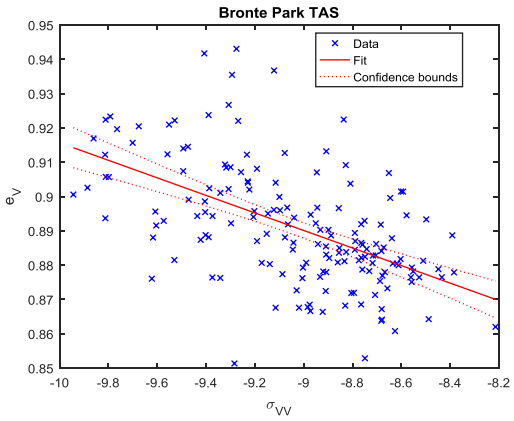
Bronte Park TAS
Data
Fit
Confidence bounds
e_V
σ_{VV}

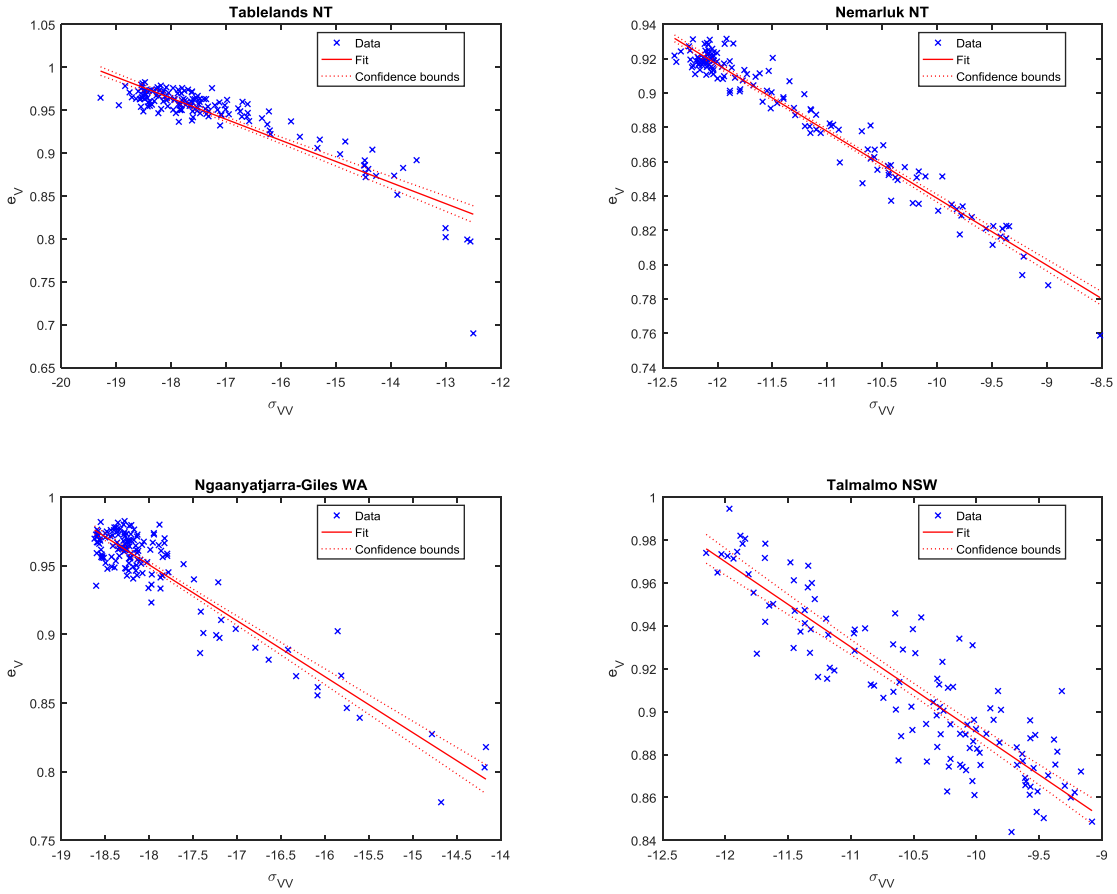

Figure 9-1: Linear regression between the vertical emissivity and the co-polarized ($\boldsymbol{\sigma_{VV}}$) backscatter

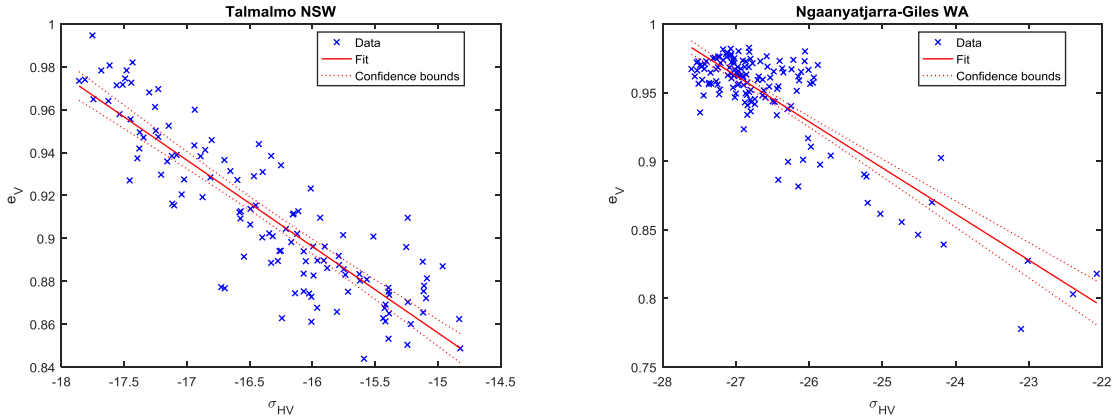

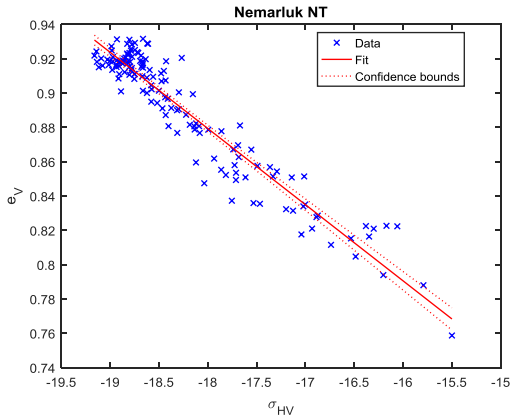
Nemarluk NT
Data
Fit
Confidence bounds
e_V
σ_{HV}

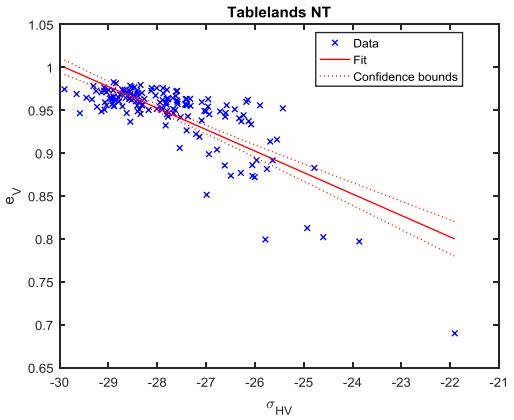
Tablelands NT
Data
Fit
Confidence bounds
e_V
σ_{HV}

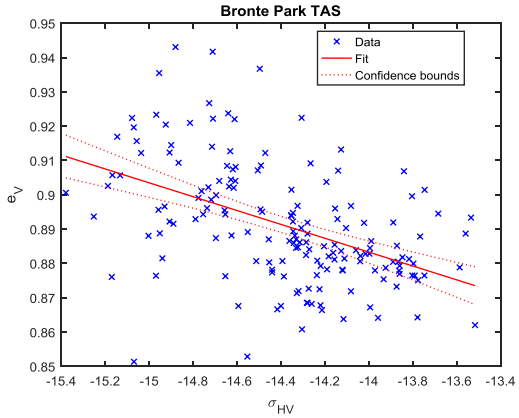
Bronte Park TAS
Data
Fit
Confidence bounds
e_V
σ_{HV}

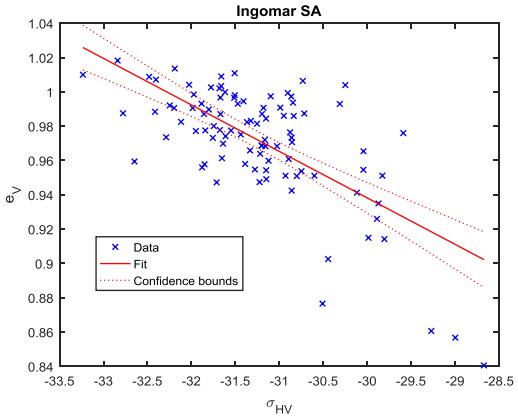
Ingomar SA
Data
Fit
Confidence bounds
e_V
σ_{HV}

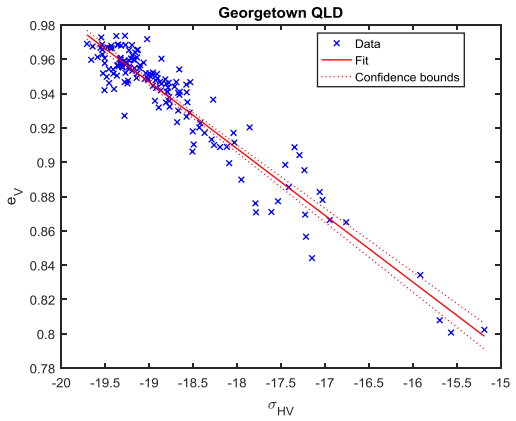
Georgetown QLD
Data
Fit
Confidence bounds
e_V
σ_{HV}

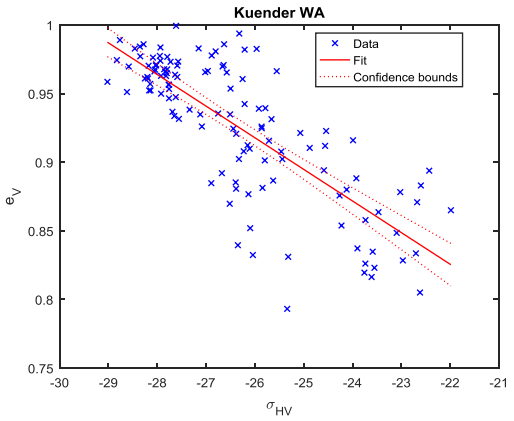
Kuender WA
Data
Fit
Confidence bounds
e_V
σ_{HV}

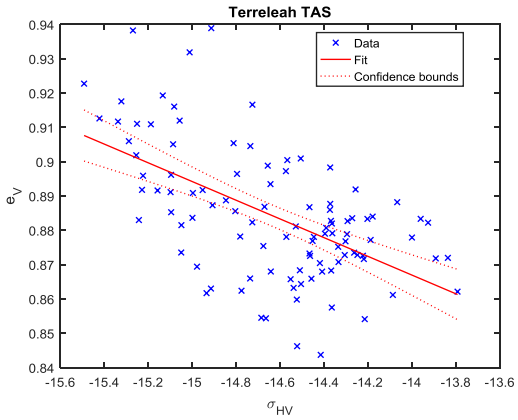
Terreleah TAS
Data
Fit
Confidence bounds
e_V
σ_{HV}

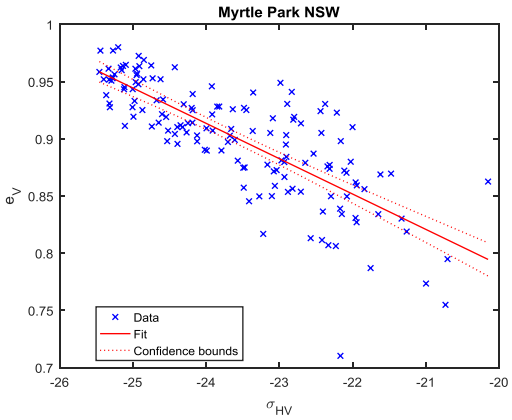
Myrtle Park NSW
Data
Fit
Confidence bounds
e_V
σ_{HV}

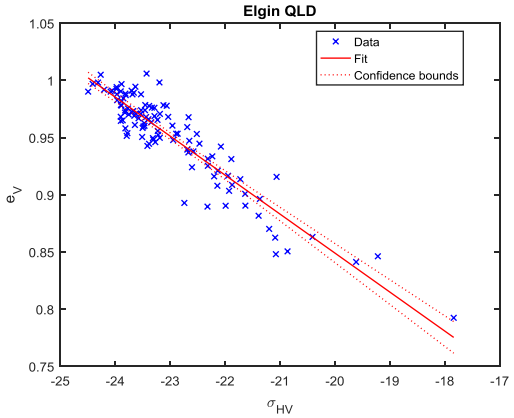
Elgin QLD
Data
Fit
Confidence bounds
e_V
σ_{HV}

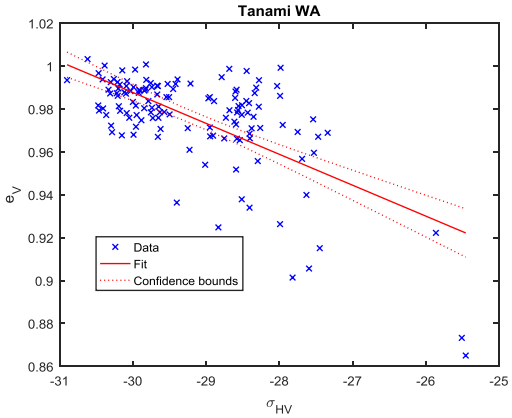
Tanami WA
Data
Fit
Confidence bounds
e_V
σ_{HV}

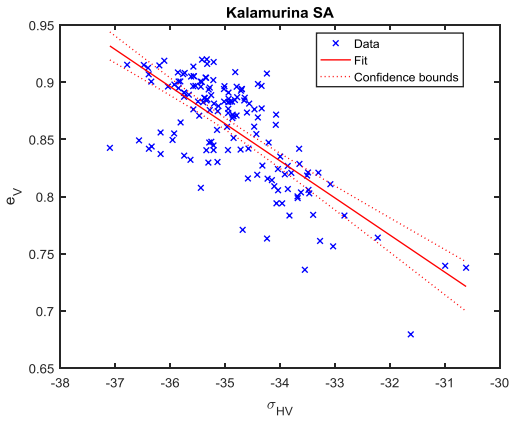
Kalamurina SA
Data
Fit
Confidence bounds
e_V
σ_{HV}

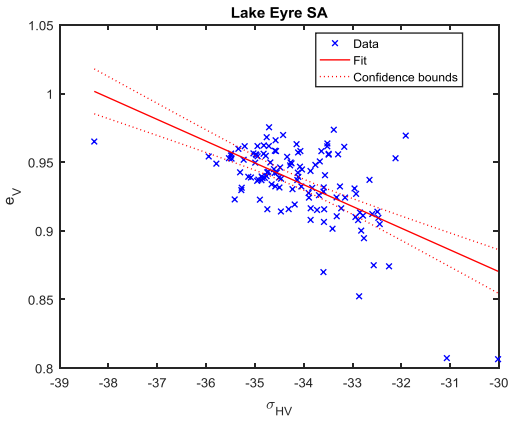
Lake Eyre SA
Data
Fit
Confidence bounds
e_V
σ_{HV}

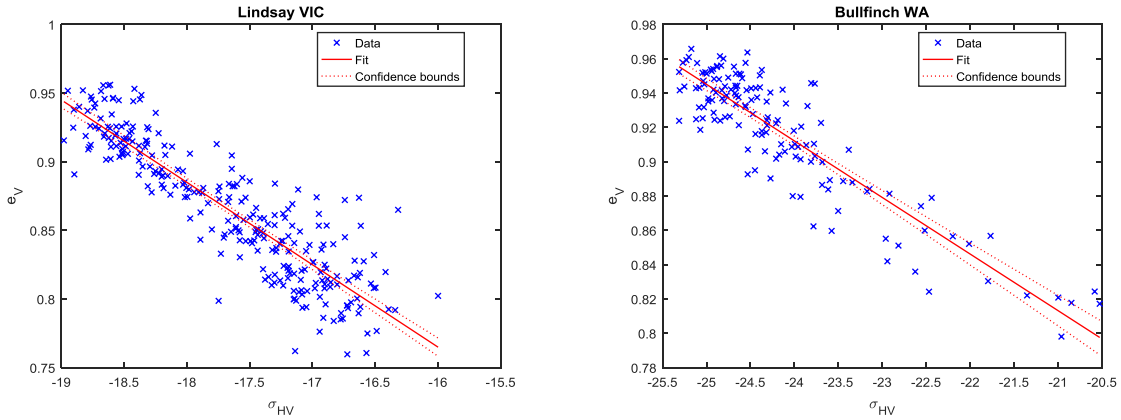

Figure 9-2: Relationship between the vertical emissivity and the cross-polarized ($\boldsymbol{\sigma_{HV}}$) backscatter

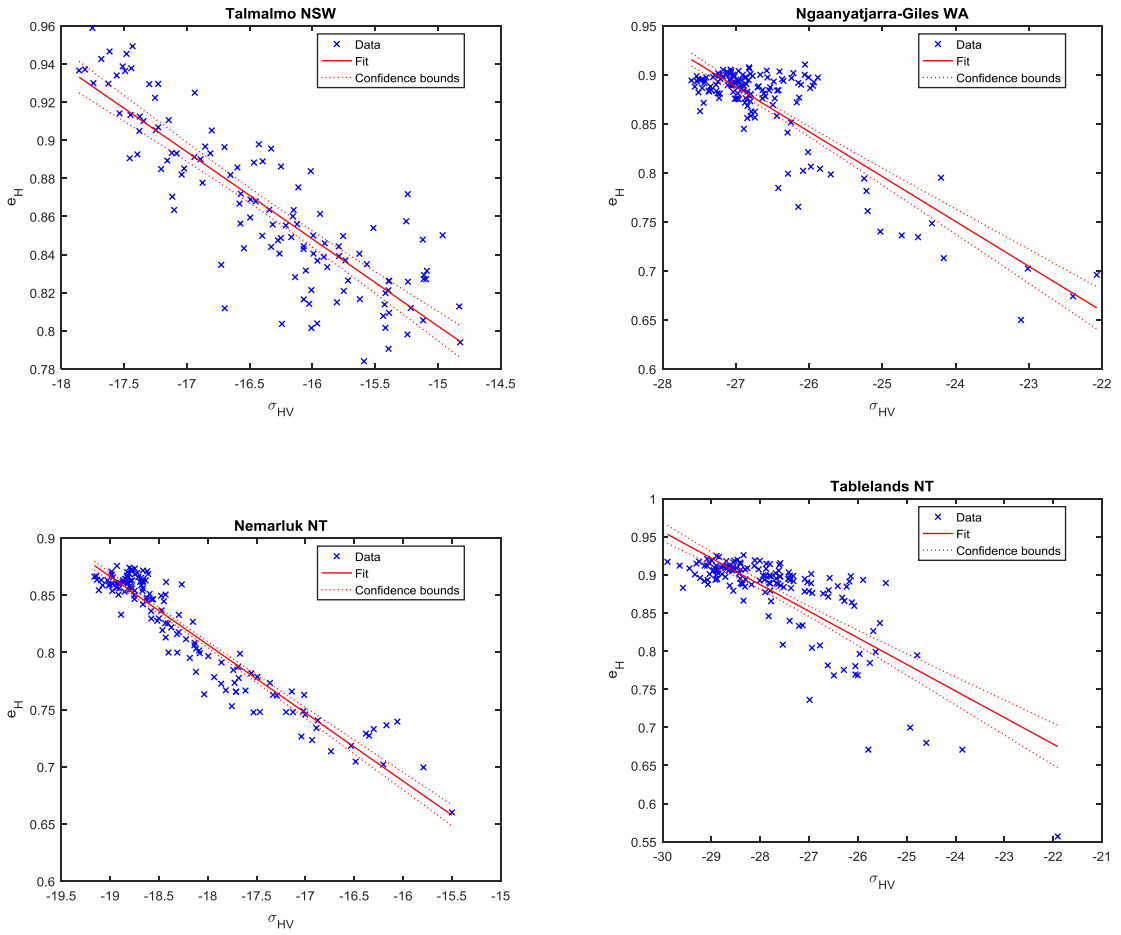

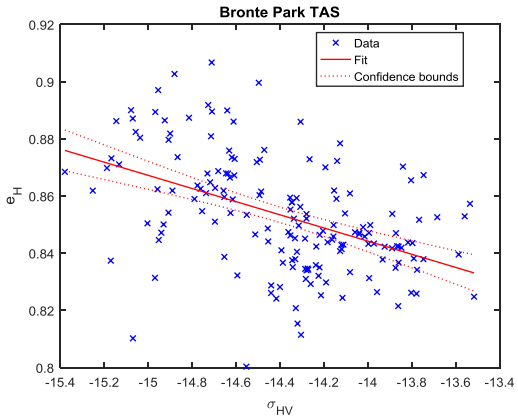
Bronte Park TAS
Data
Fit
Confidence bounds
e_H
σ_{HV}

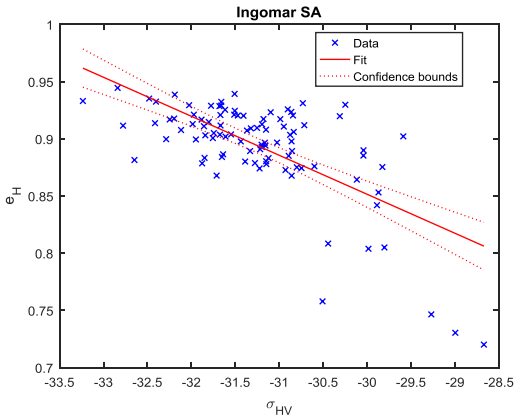
Ingomar SA
Data
Fit
Confidence bounds
e_H
σ_{HV}

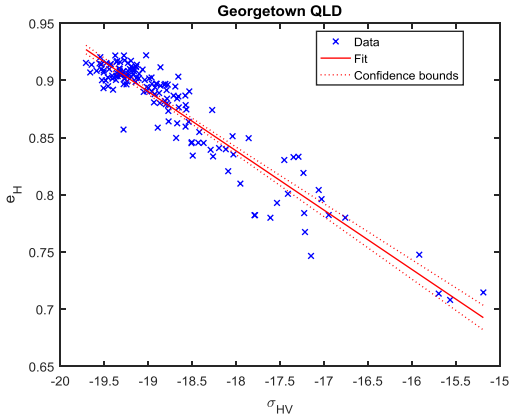
Georgetown QLD
Data
Fit
Confidence bounds
e_H
σ_{HV}

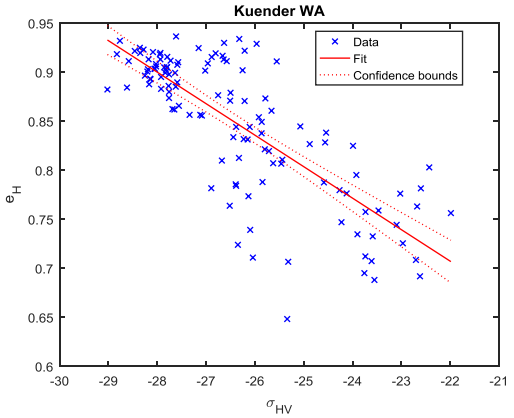
Kuender WA
Data
Fit
Confidence bounds
e_H
σ_{HV}

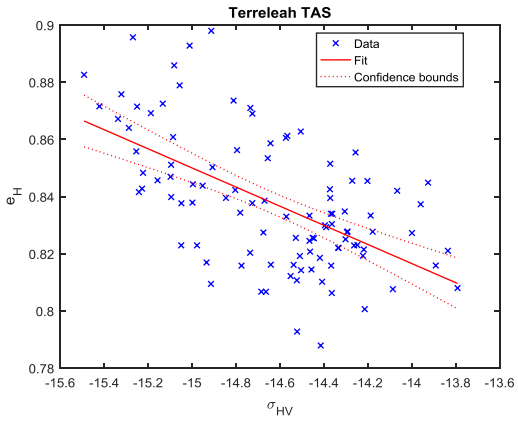
Terreleah TAS
Data
Fit
Confidence bounds
e_H
σ_{HV}

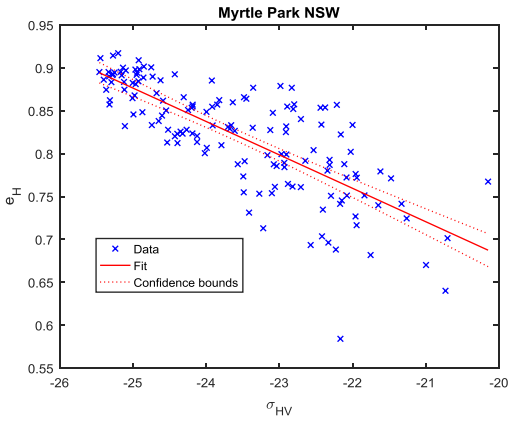
Myrtle Park NSW
Data
Fit
Confidence bounds
e_H
σ_{HV}

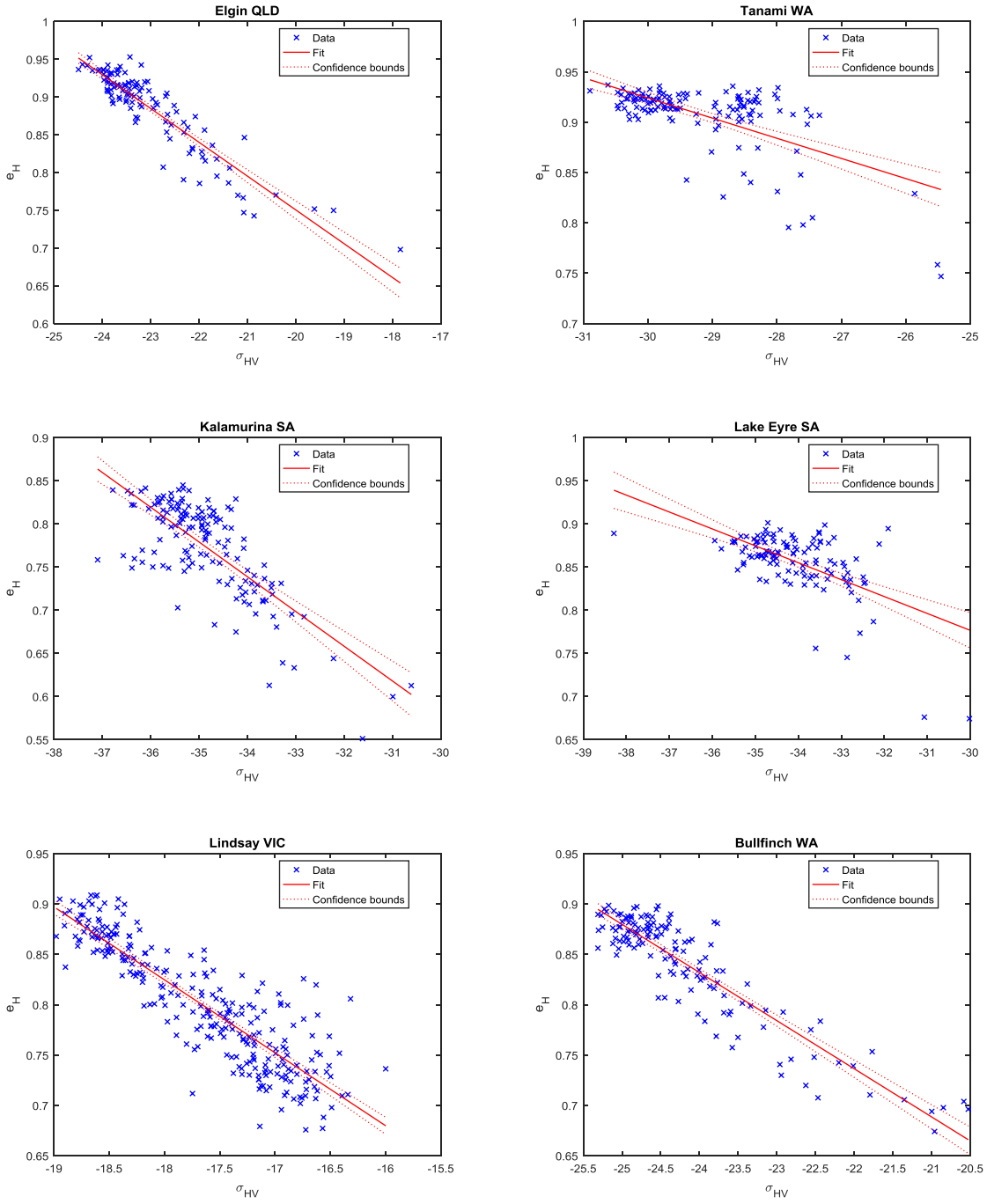

Figure 9-3: Relationship between the horizontal emissivity and the cross-polarized ($\boldsymbol{\sigma_{HV}}$) backscatter

APPENDIX 2

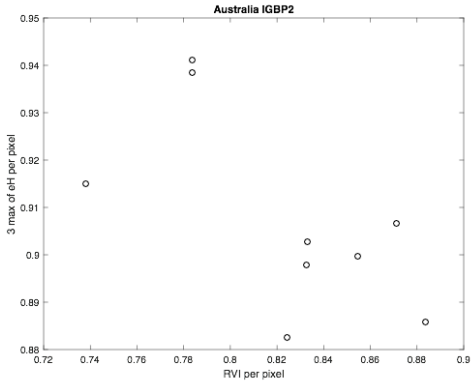
Australia IGBP2
3 max of eH per pixel
RVI per pixel

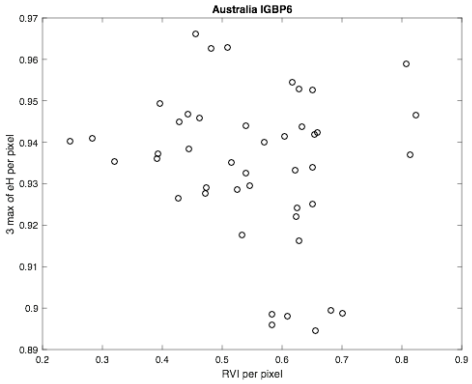
Australia IGBP6
3 max of eH per pixel
RVI per pixel

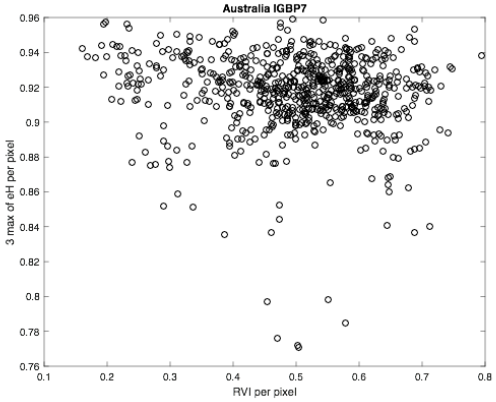
Australia IGBP7
3 max of eH per pixel
RVI per pixel

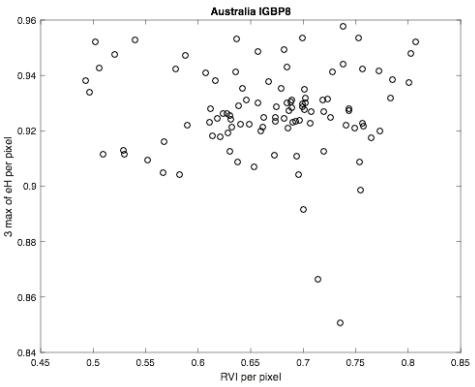
Australia IGBP8
3 max of eH per pixel
RVI per pixel

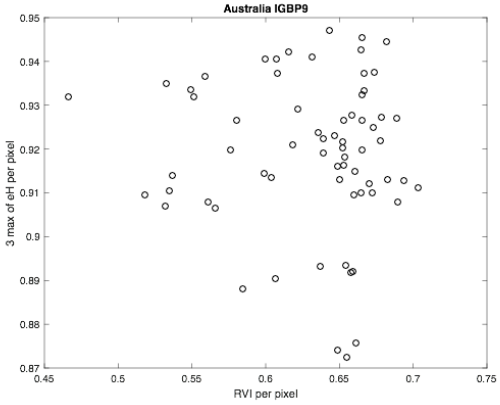
Australia IGBP9
3 max of eH per pixel
RVI per pixel

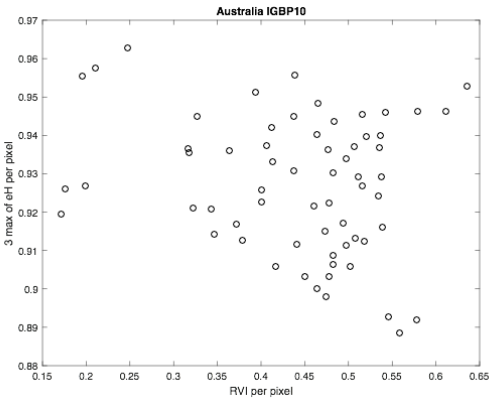
Australia IGBP10
3 max of eH per pixel
RVI per pixel

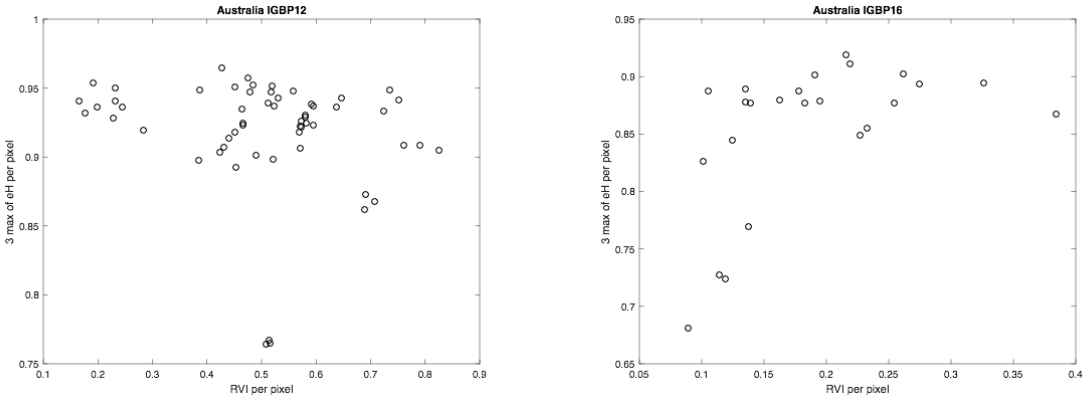

Figure 9-4: comparison between the extreme values of emissivity and the RVI values. Each graphic represents a different IGBP class